Copyright is owned by the Author of the thesis. Permission is given for a copy to be downloaded by an individual for the purpose of research and private study only. The thesis may not be reproduced elsewhere without the permission of the Author.

Spin-dependent electronic and transport properties of unconventional conductors

A thesis presented in partial
fulfilment of the requirements
for the degree of
Doctor of Philosophy
in Physics

at Massey University,
Palmerston North, New Zealand.

Philip Christopher Ingenhoven
2010

Abstract

In this thesis we present three different aspects of spin and spin-dependent transport properties in novel materials. Spurred by the prospect of *spintronic* devices, which use the spin degree of freedom of electrons instead of, or combined with, the charge degree of freedom, we analyse the spin properties of quantum wires, organic conducting polymers and sheets of graphene.

First, we examine a quantum wire that is embedded in a two dimensional electron gas. We consider the *Rashba* spin-orbit coupling, and include the effect of interaction between the conduction electrons. We construct an analytically solvable low-energy theory for the wire, and explore the interaction between two magnetic impurities in the wire. We find that both the spin-orbit coupling and the electron-electron interaction have an effect on the magnetic interaction, and find the magnetic interaction to be tunable by an electric field.

Next, we study an organic conducting polymer, which is contacted to magnetised ferromagnetic leads. In semiconducting organic polymers the current is transported by spinful polarons and spinless bipolarons. We simulate the transport through the system, including both types of charge carriers, and find the current to be insensitive to the presence of bipolarons. In addition, we find the bipolaron density to depend on the relative magnetisation of the ferromagnetic contacts. This constitutes an optical way of measuring the spin accumulation in conducting polymers.

Finally, we investigate the optical conductivity of graphene. Symmetry arguments indicate the existence of two kinds of spin-orbit coupling in the two dimensional lattice, but there is no consensus about the actual strength of these couplings. We calculated the microwave optical conductivity of graphene including both possible spin-orbit interactions. We find the low frequency dependence of the optical conductivity to have a unique imprint of the spin-orbit couplings. This opens a possibility to experimentally determine both couplings separately.

Acknowledgements

I sincerely want to thank everybody who contributed to this work and who supported me during the time of this thesis.

First of all, I thank my supervisors Ulrich Zülicke and Reinhold Egger, for making it possible for me to write my thesis at two ends of the world, at Massey University in Palmerston North and at the Heinrich Heine Universität Düsseldorf. They were both always open for questions and discussion, and I learned much of them about physics and how to approach a physical problem. I further want to thank my co-workers Markku Jääskeläinen, Zsolt Bernád and Dan Csontos for fruitful discussion and revitalising breaks. I also want to thank Alessandro De Martino for answering numerous questions via email, and François Bissey for keeping my Linux computer running. A special thanks to Jess Hughes for proofreading my thesis. I am grateful to have been provided with a Massey University Doctoral Scholarship and stipend of the MacDiarmid-Institute. And finally, thanks to all my family and friends for their support over the years.

Contents

Abstract **iii**

Acknowledgements **v**

Contents **vii**

List of Figures **ix**

List of Tables **xv**

1 Introduction and motivation **1**

2 Interplay of spin splitting and interaction in semiconductor quantum wires **9**

2.1 Introduction . . . 9

2.2 One particle picture of a quantum wire with spin-orbit coupling . . . 15

2.3 Interaction effects and RG analysis . . . 18

2.4 Luttinger liquid description . . . 25

2.4.1 Luttinger liquid for a one-dimensional interaction electron gas . . . 25

2.4.2 Luttinger liquid description for our system . . . 28

2.5 RKKY interaction . . . 31

2.5.1 One-dimensional free electron gas . . . 32

2.5.2 RKKY Interaction in our system . . . 33

2.6 Discussion . . . 38

3 Spin-dependent transport in conducting polymers **41**

3.1 Introduction . . . 41

3.2 Theoretical description of conducting polymers . . . 43

3.2.1 The Hamiltonian . . . 44

3.2.2 Ground state and exotic single particle excitations . . . 46

3.3 Modelling the transport . . . 50

3.4 Solutions for our model 54
    3.4.1 Collinear case: a readily solvable limit 54
    3.4.2 Noncollinear magnetisation 56
3.5 Discussion 58

4 Optical conductivity in Graphene: Effects of spin-orbit coupling 61
4.1 Introduction 61
4.2 Theoretical description of graphene 63
    4.2.1 Clean flat Graphene 63
    4.2.2 Including spin-orbit coupling 64
4.3 Optical conductivity 66
    4.3.1 Graphene without spin-orbit coupling 67
    4.3.2 Graphene with spin-orbit coupling 68
4.4 Results 73
4.5 Discussion 77

5 Summary and Conclusions 81

A Second order RG equations 85

B Bosonisation and Luttinger liquids 90

Bibliography 95

List of Figures

1.1 Schematic view of a giant magneto resistance device. In a) both contacts are magnetised in the same direction. The polarised electrons can pass through the sample easily. The device has a low resistance. In b) the magnetisation of the two contacts is antiparallel. Polarised electrons originating from the left contact can not enter the right contact, which causes a higher resistance in the device. 2

1.2 Schematic view of a Datta Das device. Both contacts are magnetised in the same direction. An electric field perpendicular to the two-dimensional electron gas cause spin-orbit coupling. a) The spin-orbit coupling is tuned in a way that the spin precesses 360^o over the length of the system. The fully rotated spin now can enter the right contact. b) Here the spin-orbit coupling is tuned in a way that the spins only precess 180^o over the length of the system, thus the electrons can not enter the right contact. 3

1.3 Schematic view of a semiconductor heterojunction. AlGaAs has a higher Fermi energy and electrons spill into the GaAs, leaving positively charge donors behind. These cause a band bending. This results in a high electron density near the interface, the two-dimensional electron gas. 5

1.4 Chemical structure of polyacetylene. The polymer consists of a chain of CH groups that are connected via alternating single and double bonds. . . 6

1.5 Graphene is a two-dimensional hexagonal lattice of carbon atoms. 7

2.1 Schematic setup of a 2DEG in the $x - z$ plane with additional confinement in z-direction and the E field in y-direction causing the spin-orbit coupling. Figure used with the kind permission of A. Schulz. 10

2.2 One-dimensional subbands due to the confining potential $V(z) = m\omega^2 z^2/2$ 11

2.3 Dispersion relation of free one-dimensional electrons: a) Zeeman split bands: A magnetic field causes the dispersion relation to shift up or down in energy depending on whether the spins are aligned parallel or antiparallel to the field b) Rashba split bands: A perpendicular electric field also causes spin-orbit coupling, the shift in the dispersion relation depends on momentum and spin state 12

2.4 Schematic band structure (2.15) of a typical one-dimensional Rashba quantum wire. The red/blue curves show the $s = \pm$ bands, and the dotted curves indicate the next subband (the Fermi energy ϵ_F is assumed below that band). For the low-energy description, we linearise the dispersion. It is notationally convenient to introduce bands A (solid lines) and B (dashed lines). Green and black arrows indicate the respective spin amplitudes (exaggerated). The resulting Fermi momenta are $\pm k_F^{(A,B)}$, with Fermi velocities $v_{A,B}$. 16

2.5 Schematic view and Feynman diagram of the interaction processes (solid lines indicate right movers and dashed lines left movers). a) $g_{4\|A}$, which couples only fermions on the same branch (analogous for B), describing forward scattering and b) $g_{4\perp}$, in which the coupled fermions are still on the same side of the Fermi surface but couple different branches A and B. The momentum transfer in both cases is close to zero, thus the coupling constant for these processes is $W_0 = \tilde{V}(q = 0)$. 21

2.6 Schematic view and Feynman diagram of the interaction processes (solid lines indicate right movers and dashed lines left movers). the $g_{2\perp}$ consists of two contributions that have the same operator structure after commuting the fermions a) $W_0 = \tilde{V}(q = 0)$. b) $W_1 = \cos^2(\theta_A - \theta_B)\tilde{V}(q = k_F^{(A)} + k_F^{(B)})$. Commutation of the fermions gives the minus sign in equation (2.37). . . . 22

2.7 Schematic view and Feynman diagram of the interaction processes (solid lines indicate right movers and dashed lines left movers). a) $g_{2\|\nu}$ the transferred momentum is close to zero, hence the coupling is $W_0 = \tilde{V}(q = 0)$. b) g_f corresponds to intra band scattering with band flip. For the coupling on finds $W_1 = \cos^2(\theta_A - \theta_B)\tilde{V}(q = k_F^{(A)} + k_F^{(B)})$. 23

2.8 Example for a term that would be possible from a momentum conservation point of view and contribute to g_f, the momentum transfer would equal the difference between the two Fermi points $k_F^{(A)} - k_F^{(B)}$. The thin wire approximation, though, kills this term since equation (2.34) contains exchange integral between the harmonic oscillator functions $H_0(z)$ and $H_1(z)$, which are orthogonal and thus the integral is zero. (Solid lines indicate right movers and dashed lines left movers.) 23

2.9 a) In higher dimensions quasi free excitations are possible. One can define quasi particles that essentially behave like free electrons, but b) in one dimension every excitation in an interacting system has to be collective. . . 26

2.10 Schematic view of the spectral function of one-dimensional electrons. a) Free noninteracting electrons. The spectral function is a simple delta peak at $\omega = v_F q$ indicating the true single particle excitation. b) Interacting electrons described by the Luttinger liquid theory. Instead of a delta function one finds two divergencies corresponding to the charge density waves $(v_c q = \omega)$ and spin density waves $(v_\sigma q = \omega)$ with different power laws. So no single particle excitation can exist in a Luttinger liquid. 28

3.1 The structural diagram for *trans*-polyacetylene displays the typical dimerisation pattern. In *trans*-polyacetylene an additional symmetry is found, since the double and the single bonds can be interchanged without changing the energy of the system. 43

3.2 Structural diagram for *cis*-polyacetylene. Here the additional symmetry of *trans*-polyacetylene is broken. 43

3.3 Schematic extended band structure for a one dimensional lattice with half filling without phonon effects. 45

3.4 Degenerate ground states for $\Delta(x) = \pm\Delta_0$. Top: phase **A**, Bottom: phase **B**. 47

3.5 Left: Schematic figure of a soliton excitation. On the left side of the polymer the system is in phase **A** and the right in phase **B**. The single electron state can now be filled with one, two, or zero electrons. Top left: one electron causing a charge neutral but spinful excitation. Middle left: the electronic state is empty, thus one has a localised positive, but spinless charge. Bottom left: two electrons lead to a spinless negative excitation. Right: The corresponding dispersion relation with the localised midgap states is shown. 48

3.6 a) Dimerisation potential for a polaron excitation. b) Band structure and single particle states, here the occupation of the states leads to an electron polaron, with spin 1/2. 49

3.7 Schematic view of the two terminal device. A conducting polymer will be contacted with arbitrarily magnetised ferromagnetic contacts. $G^{\uparrow(\downarrow)}$ describe the spin dependent tunnelling into the polymer and $G^{\uparrow\downarrow}$ has to be included for noncollinear magnetisation, to account for boundary exchange effects. 50

3.8 Bipolaron density $n_{BP}(x,\theta)$ in equation (3.47) for collinear magnetisations, i.e., $\theta = 0$ (solid curve) and $\theta = \pi$ (dashed curve). We use a representative parameter set for hole transport. In units where $G_P = D_P/L = 1$, the parameters are $D_{BP} = 2L/3, G^{\uparrow} = 10^4, G^{\downarrow} = 10^{-2}, k = D_P/10, b = D_{BP}/10$, $2\Delta_0 = 3.5$, $\bar{\mu} = -2$, $T = 0$, and $eV = 1$, see text. The inset shows $\Delta n_{BP} = [n^{(+)}_{BP}(x) - n^{(-)}_{BP}(x)]/n^{(-)}_{BP}(L/2)$ for the same curves. 55

3.9 The scattering rate for bipolaron creation is proportional to $n_{\uparrow}n_{\downarrow}(x,\theta)$. This rate is shown for $\theta = 0$ (dashed curve) and $\theta = \pi$ (dot dashed curve). The solid curve shows the change in bipolaron density for the respective magnetisations $\Delta n_{BP} = [n^{(+)}_{BP}(x) - n^{(-)}_{BP}(x)]/n^{(-)}_{BP}(L/2)$ (scaled with factor 5 for clarity). It is clearly seen that in the parallel case there is a bigger scattering rate at first, and hence more bipolarons. The two rates cross at $x/L = 0.57$ which is exactly the point of inflection in the bipolaron density difference, see vertical line. We used the same parameter set as in figure 3.8 57

3.10 Spin accumulation sensitivity $R(\theta)$, see equation (3.43), of the bipolaron density as a function of the magnetisation tilt angle. Parameters are as in figure 3.8, additionally we set $\mathrm{Re}G^{\uparrow\downarrow} = \mathrm{Im}G^{\uparrow\downarrow} = 5.1 \times 10^3$. 58

4.1 a) Carbon atoms form a hexagonal lattice. $\vec{\delta}_i$ define the distance between next neighbours and $\vec{a}_j$ define the unit cell. There are two inequivalent lattice sites per unit cell, denoted **A** and **B**. b) Reciprocal lattice with the reciprocal lattice vectors $\vec{b}_{1,2}$ and the symmetry points Γ, M, K, and K'. The Fermi point are K and K'. 62

4.2 a) Tight-binding approximation of the bandstructure of graphene. One can clearly see the linear cones at the K and K' points, where the hole states (dark blue) and electron states (lighter blue) spectra touch each other. b) Top view of the bandstructure with symmetry points. 65

4.3 Optical conductivity for a flat sheet of graphene without spin-orbit coupling, where $\sigma_0 = 2e^2/h$. For $\omega \to \infty$ the optical conductivity reaches the universal value $e^2/(4\hbar)$. 69

4.4 Regions in the Δ_R-Δ_I-plane where the different $\tilde{F}_n$ contribute, cf. Table 4.1. There is no contribution to $\sigma(\omega)$ from region 4. 73

4.5 Optical conductivity at $T = 1$ K for graphene at the charge-neutrality point ($\mu = -\Delta_I$) with $\Delta_R = 0$ but finite $\Delta_I = 100\,\mu$eV. The spectral gap $2\Delta_I$ implies $\sigma(\omega) = 0$ for $\omega < 2\Delta_I$ when considering only bulk states. Inset: Low-energy part of the bandstructure. 74

4.6 Same quantity plotted and parameters used as in figure 4.5, except that $\Delta_I = 0$ and $\Delta_R = 100\,\mu$eV and $\mu = 0$. Kinks arise when new transitions between different bands become possible at certain critical values of ω (see inset). 75

4.7 Same quantity plotted and parameters used as in figure 4.5, except that $\Delta_R = 100\,\mu$eV and $\Delta_I = 0.2\Delta_R$, thus realizing the case $2\Delta_I < \Delta_R$. We set $\mu = 0$ to maintain charge neutrality. More kinks appear as the bands are less symmetric than for the cases shown in figures 4.5 and 4.6. 76

4.8 Same as figure 4.5 but for the special case $2\Delta_I = \Delta_R$ with $\Delta_R = 100\,\mu$eV, setting $\mu = 0$ to ensure charge neutrality. Inset: The bandstructure shows that three bands cross at $k = 0$, and hence some of the kinks in $\sigma(\omega)$ disappear. 77

4.9 Same as figure 4.5, except that $\Delta_I = 0.8\Delta_R$ with $\Delta_R = 100\,\mu$eV, thus realizing the case $2\Delta_I > \Delta_R$. Charge neutrality is maintained by setting $\mu = (\Delta_R - 2\Delta_I)/2$. 79

4.10 Same as figure 4.7, focusing on the region $0.4 < \hbar\omega/\Delta_R < 1.6$. The solid curve is for $T = 1$ K, the dashed curve for $T = 10$ K, and the dot-dashed one for $T = 100$ K. The distinct kinks are thermally smeared and suppressed at elevated temperatures, but remain visible up to $T \approx 10$ K. 79

List of Tables

4.1 List of $\tilde{F}_n$ functions and the regions in which they contribute, as illustrated in figure 4.4. 73

Chapter 1

Introduction and motivation

Recent years have witnessed tremendous advances in nanotechnological applications and fundamental understanding of the materials involved [1–3]. The aim in nanotechnology is to understand and use the quantum properties that the nano-sized devices are governed by, to fabricate smaller, faster, and more energy efficient devices. At length scales of a few to a hundred nano meters, the quantum nature of the system plays an important role. Thus, it is essential to understand the underlying physics of the material. A full quantum mechanical approach for the thousands of particles is an impossible task. Therefore, one needs to find ways to describe the important quantum features without overloading the model with detail, as we will see in the effective models used in the course of this thesis. The materials used range from low dimensional quantum structures within semiconductor heterostructures such as two-dimensional electron gases, quasi one-dimensional quantum wires, or zero-dimensional quantum dots [4]. Also new materials such as conducting polymers and molecules are being investigated [5]. Another promising candidate for nano electronics are carbon based structures such as sheets of graphene [6, 7], carbon nanotubes [8], and fullerenes [9]. A large effort is also made to investigate the properties of compound materials which consist of layers of magnetic and nonmagnetic materials.

A key role is played by the quantum mechanical spin degree of freedom, opening the field of *spintronics*, or spin dependent electronics. For a detailed review of this new exciting field see [10]. The spin is a relativistic property of the electron, giving it an intrinsic angular momentum and magnetic moment. Electrons are fermions because they have a spin quantum number of $s = \frac{1}{2}$, they carry a magnetic moment of $m = -g\mu_B s$, where g is the electron g factor and μ_B the Bohr magneton. The idea now is to influence this degree of freedom magnetically or electrically, to change the transport properties of a sample.

There are two main routes to implement *spintronic* devices. These are exemplified by devices working on the bases of the giant magneto resistance effect (GMR) [11] and the spin field effect transistor (spin-FET) proposed by Datta and Das [12].

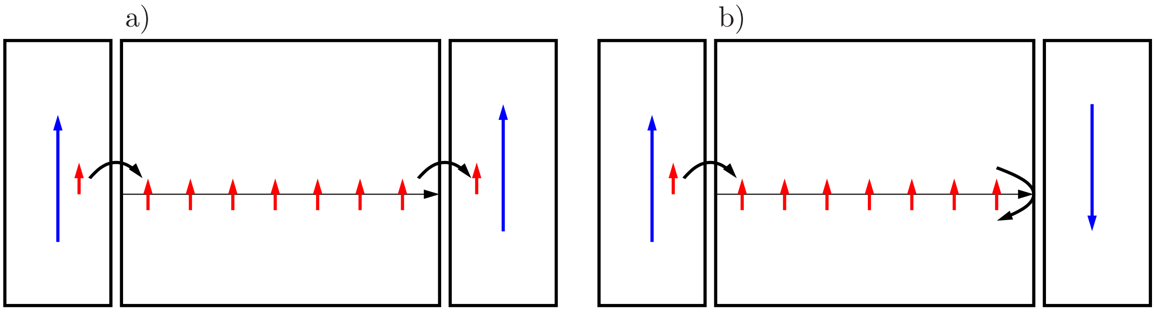

Figure 1.1: Schematic view of a giant magneto resistance device. In a) both contacts are magnetised in the same direction. The polarised electrons can pass through the sample easily. The device has a low resistance. In b) the magnetisation of the two contacts is antiparallel. Polarised electrons originating from the left contact can not enter the right contact, which causes a higher resistance in the device.

The simpler of the two devices mentioned above is based on the GMR effect. In a sandwich structure, made of two ferromagnetic materials separated by a nonmagnetic layer, the current is sensitive to the relative magnetisation of the two ferromagnets. From the magnetic left contact, spin polarised electrons enter the nonmagnetic middle layer. If the right contact is polarised in the same way as the left, the electrons can easily exit the system, see figure 1.1 a). If the right contact is magnetised in the opposite way, the electrons with spin aligned to the left contact's magnetisation have a high probability to be scattered back, see figure 1.1 b). Measuring the current through the system, one finds the resistance to be significantly different in the two cases. This could in principle lead to magnetic random access memory (MRAM) devices, which would deliver a non-volatile random access memory [13]. Other devices based on the GMR effect have already reached the computer market in read-out heads for compact hard disks [14, 15] and the Nobel price in Physics was awarded for this in 2007. However, there is room for improvement concerning the used materials and the geometry of such devices. The most important feature here is the spin scattering length, which is defined by the coupling of the spin degree of freedom and the orbital motion of the electron in the sample, and other spin dependent scattering mechanisms like magnetic impurity scattering. A similar principle is used in the TMR (tunnel magneto resistance) devices where the nonmagnetic layer is replaced by a tunnelling junction [16].

The second promising approach is based on an idea of Datta and Das [12], where instead of changing the magnetisation of the contacts, the polarisation of the charge carriers in the sample is influenced to change the current through the system, see figure 1.2. The working principle of this spintronic field effect transistor, is similar to that of an electro optic modulator. The device is a two-dimensional electron gas which is now similar to the

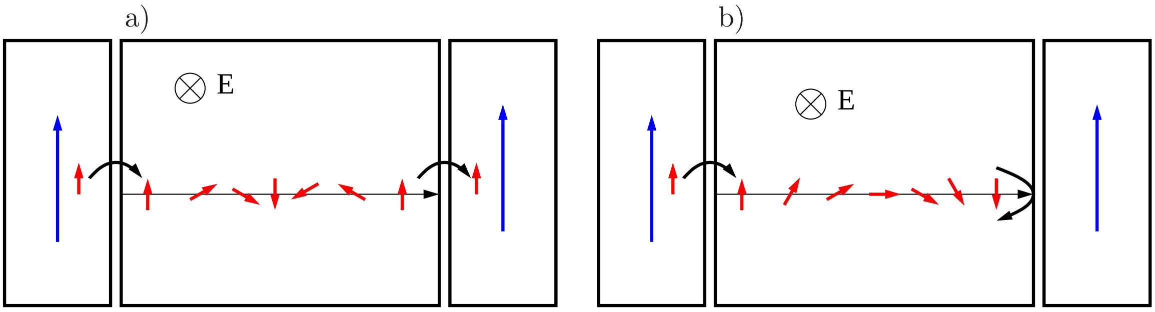

Figure 1.2: Schematic view of a Datta Das device. Both contacts are magnetised in the same direction. An electric field perpendicular to the two-dimensional electron gas cause spin-orbit coupling. a) The spin-orbit coupling is tuned in a way that the spin precesses 360^o over the length of the system. The fully rotated spin now can enter the right contact. b) Here the spin-orbit coupling is tuned in a way that the spins only precess 180^o over the length of the system, thus the electrons can not enter the right contact.

GMR type devices contacted to ferromagnetic leads. The difference is that the relative magnetisation of the contacts is not changed, but the polarisation direction is the same on both sides. As in the GMR-like devices, polarised electrons enter at the left contact. In a two-dimensional electron gas an electric field which is perpendicular to the plane of the gas is always present. It arises due to an asymmetry in the confining potential. This electric field gives rise to coupling between the spin degree of freedom of the electron, and its orbital motion. The spin-orbit coupling in turn causes the electron spin to precess with a precession length determined by the strength of the spin-orbit coupling. Via applying an additional electric field the spin-orbit coupling becomes tunable. Thus, the precession length can be changed in way that the electron spin either rotates by 180^o or 360^o, see figure 1.2. An electron with its spin rotated by 180^o degrees has a lower chance of entering the right contact than an electron with a spin that carried out a full 360^o rotation. Thus, through varying the external electric field the spin dependent current through the system can be influenced. This idea has spurred a lot of interest and fundamental research of spin-orbit coupling. Twenty years after the first proposal, Koo *et al.* [17] have demonstrated the possibility to electrically control the spin precession in a spin-injected field effect transistor, which in some aspects behaves as predicted by theory, but other aspects deserve further investigation [18, 19]. One problem is that interference of different angular modes washes out the effect to some extent. To naively overcome this problem it has been proposed to further confine the electrons to one dimension via back-gates, but this leads to mixing of the subbands and a peculiar spin distribution [20], which we will further investigate in the next chapter.

To understand spin-dependent transport, it is vital to fundamentally understand the nature of spin-orbit coupling and other spin-dependent scattering mechanisms in the materials used. This thesis is dedicated to investigating the spin and spin transport properties in three different systems.

In chapter 2 we focus on a quantum wire that is confined within a two-dimensional electron gas. A two-dimensional electron gas occurs at the interface of differently doped semiconductors, see figure 1.3. To understand why this layer is formed we consider an AlGaAs - GaAs heterojunction. The Fermi energy E_F in the widegap AlGaAs layer is higher than its counterpart in the narrowgap GaAs layer. Thus electrons will spill over into GaAs layer leaving behind positively charged donors. These create an electrostatic potential which in turn will cause a band bending as shown in figure 1.3. In an equilibrium situation the Fermi energy is constant throughout the system. At the interface, the electron density is peaked and the Fermi energy crosses the conduction band in this two-dimensional area, thus forming a thin conducting layer near the interface. As mentioned above, the potential confining the electrons to two dimensions is asymmetric, causing an effective electric field perpendicular to the interface which, in turn, couples the spin degree of freedom to the orbital motion of the electron. The strength of this coupling can be tuned by an additional perpendicular electric field. To confine the electrons further, back-gates are used. An applied voltage on these gates will push the electron into a small quasi one-dimensional channel; a quantum wire. In the first part of our work we will describe such a wire and include the effects of electron-electron interaction. Electron-electron interactions have a fundamental effect on the physics of the system. It is not possible to apply the quasiparticle approach used in higher dimensions, instead we use a Luttinger liquid-like description for the quantum wire. In one dimension, interactions will not allow single-particle excitations and only collective excitations are allowed. In this model we are then able to calculate the interaction strength between two localised magnetic moments. We published this work in [21].

In chapter 3 we look at a GMR-like situation and investigate a system in which we chose a conducting polymer as the non magnetic middle layer. Usually, plastics which are made from polymers are insulators, but conjugated polymers, a special class of polymers, have been found to conduct the electrical current, similarly well as semiconductors or metals. They show a fundamentally different transport behaviour to that of conventional conducting materials [22]. These polymers are semiconductors but via doping the conductivity can be enhanced almost to the level of metallic conductors. Conducting polymers or plastics are a class of polymers in which one finds an alternating single bond - double bond structure. The simplest of these polymers is polyacetylene (CH_x), see figure 1.4. These materials are insulators or semiconductors, with a gapped bandstructure. Although, for the highly conducting polymers, the conduction has a clear metallic nature: the conductivity remains non-zero in the zero temperature limit, indicating the absence of an energy gap and the presence of delocalized electronic wavefunctions. Here, we focus

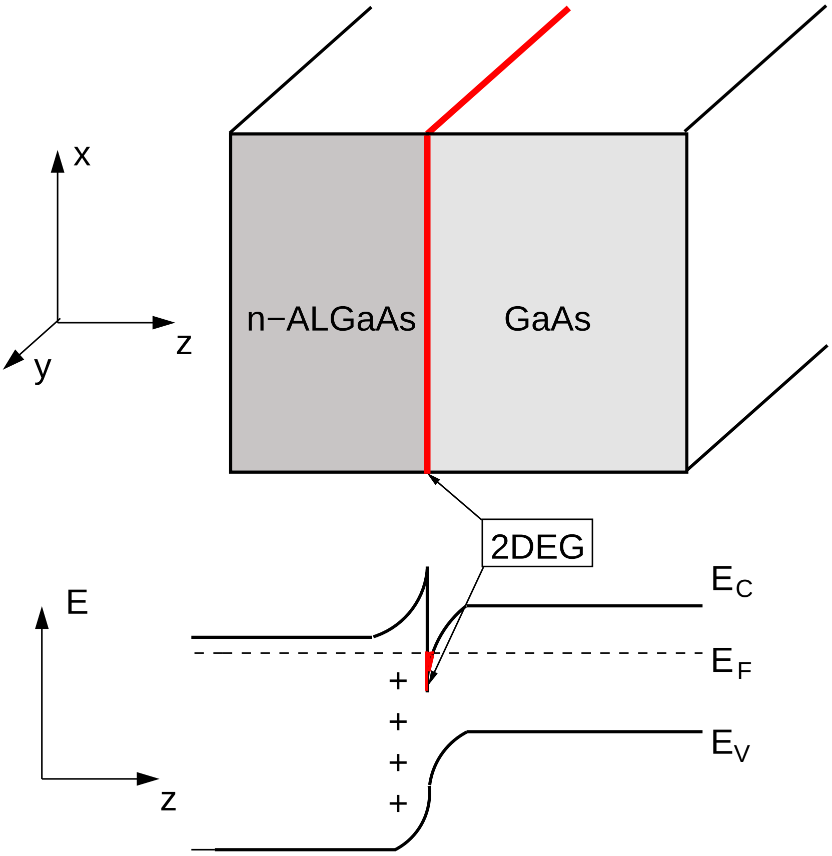

Figure 1.3: Schematic view of a semiconductor heterojunction. AlGaAs has a higher Fermi energy and electrons spill into the GaAs, leaving positively charge donors behind. These cause a band bending. This results in a high electron density near the interface, the two-dimensional electron gas.

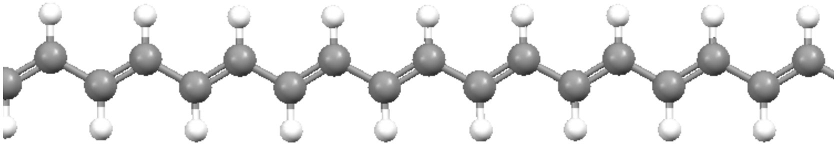

Figure 1.4: Chemical structure of polyacetylene. The polymer consists of a chain of CH groups that are connected via alternating single and double bonds.

on semiconducting, slightly doped polymers. Due to the strong electron-phonon coupling, exotic excitations within the gap are possible. The most important of these excitations are polarons, bipolarons and to a lesser extent solitons, see [23]. A single electron, or hole, will deform the surrounding lattice and cause the excitation to be local and inside the gap. These excitations are called polarons. Polarons are singly charged and have a spin of 1/2 just like conventional electrons and holes. Bipolarons are bound states between two polarons, and are doubly charged, but have zero spin. Solitons are excitations in *trans*-polyacetylene or similar polymers that form locally in a region where the double bond - single bond pattern changes. Solitons occur as a negative or positively charged quasiparticle with zero spin, or as a neutral state which carries spin 1/2. In the conducting polymers we look at, the charge is only transported by polarons and bipolarons. We investigate the spin dependent transport through a polymer, taking into account that two polarons can combine into one bipolaron and vice versa. We compute the current through a polymer that is contacted with arbitrarily magnetised contacts, and also calculate the bipolaron density for different magnetisation configurations. The results of this project were published in [24].

In chapter 4 we concentrate on graphene. Graphene is a monolayer of carbon atoms packed into a hexagonal honeycomb lattice, see figure 1.5. It is the basic building block for carbon-based materials such as nanotubes, fullerenes and graphite. Free standing two-dimensional graphene was not believed to exist due to theoretical arguments stating that two-dimensional lattices are unstable [25]. Only recently this view was proved wrong by the

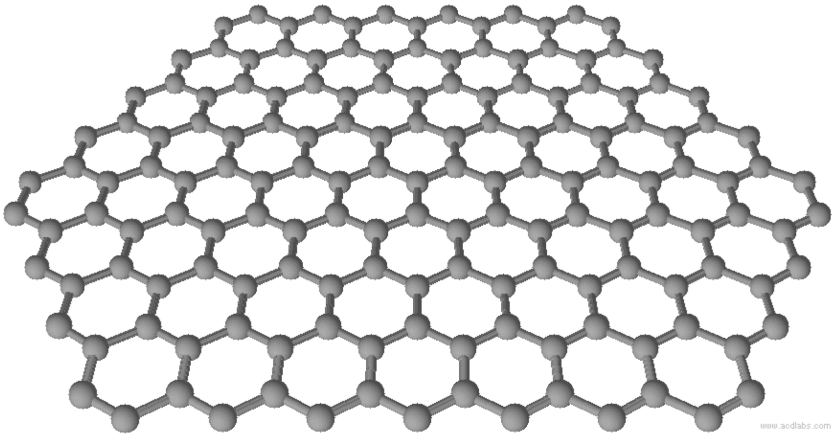

Figure 1.5: Graphene is a two-dimensional hexagonal lattice of carbon atoms.

experimental discovery of isolated two-dimensional graphene [6, 7]. The conduction band and the valence band of graphene touch each other at the Fermi points. The bandstructure close to these points is linear, and graphene can be described in terms of a relativistic massless Dirac equation. This opens the possibility to experimentally test the relativistic theory at low energies. Nevertheless, the value of graphene is not purely academic. Since its discovery it has been scrutinised for possible usage in nanotechnological applications. Due to its small spin-orbit coupling it is a promising candidate for spintronics. However the spin-orbit coupling is not zero and the actual value of the coupling strength is still being discussed. In our work we contribute to this discussion. We calculate the optical conductivity at low energies, including the two most important spin-orbit coupling terms. We found kinks and peaks in the optical conductivity that, if measured, will make experimental determination of the coupling strength possible. We published the results of this work in [26].

Chapter 2

Interplay of spin splitting and interaction in semiconductor quantum wires

2.1 Introduction

Spin transport in one-dimensional quantum wires continues to be a topic of much interest in solid-state and nanoscale physics. It offers interesting fundamental questions as well as possible technological applications [10]. Of particular interest to this field is the spintronic field effect transistor (spin-FET) proposal by Datta and Das [12], as described in the introduction. In this chapter we examine the properties of a quantum wire embedded in a two-dimensional electron gas (2DEG). This is done via gates on top of the 2DEG, to confine the electron further to one dimension. For a schematic figure of the setup see figure 2.1. The electrons in a quantum wire will be confined in a parabolic potential in the z-direction, see figure 2.1. We first want to consider a quantum wire without spin-orbit coupling. The Hamiltonian for a clean quantum wire reads

$$H_{QW} = \frac{1}{2m}\left(p_x^2 + p_z^2\right) + \frac{m}{2}\omega^2 z^2, \tag{2.1}$$

where the z dependent part is merely the quantum mechanical harmonic oscillator equation which is readily solved and can be found in every quantum mechanics text book. The discrete eigenenergies read $E(n) = \left(n + \frac{1}{2}\right)\hbar\omega$. In the x direction the electrons are described by free waves with momentum k_x. The total energy then adds up to

$$E(k_x, n) = \frac{\hbar^2 k_x^2}{2m} + \left(n + \frac{1}{2}\right)\hbar\omega. \tag{2.2}$$

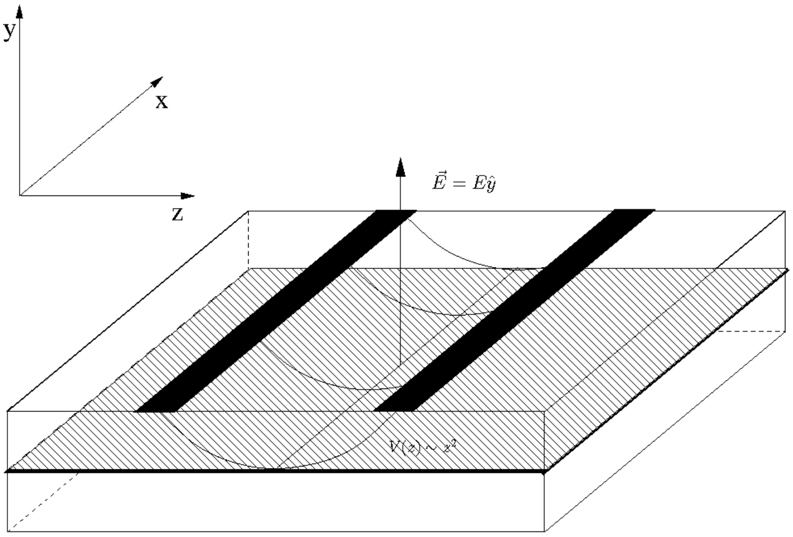

Figure 2.1: Schematic setup of a 2DEG in the $x - z$ plane with additional confinement in z-direction and the E field in y-direction causing the spin-orbit coupling. Figure used with the kind permission of A. Schulz.

The dispersion relation of a clean quantum wire is sketched in figure 2.2. States with different n belong to different subbands. The energy spacing between the subbands is $\hbar\omega$. The narrower the confinement, the larger the ω and the further apart are the subbands. Up to this point the subbands are spin degenerate, i.e., both spin directions have the same energy.

We now look at a situation where the spin degeneracy, or $SU(2)$ invariance, is broken. The spin degeneracy can be broken via a magnetic or an electric field. We first show the difference between these two effects. One-dimensional electrons in the lowest subbands are governed by the Hamiltonian

$$H_0 = \frac{p_x^2}{2m}, \tag{2.3}$$

where p_x is the momentum operator and m the electron mass. For the coupling of the electrons with a magnetic field we add the Zeeman term $H_Z = -\boldsymbol{\mu} \cdot \boldsymbol{B}$, where $\boldsymbol{\mu} = g\mu_B\boldsymbol{\sigma}$ is the magnetic moment of the electron, with g being the electron g-factor, μ_B the Bohr magneton, and $\boldsymbol{\sigma}$ the vector of Pauli matrices. With this we find a different dispersion relation for each spin state ($\pm$)

$$E_Z = \frac{k_x^2}{2m} \pm \frac{1}{2}\mu_B g|\boldsymbol{B}|, \tag{2.4}$$

where k_x is the momentum quantum number. The bands for the two spin directions are split by a constant energy, see figure 2.3 a). Note that the magnetic field not only breaks the $SU(2)$ symmetry, but also the time reversal symmetry. An electric field, however,

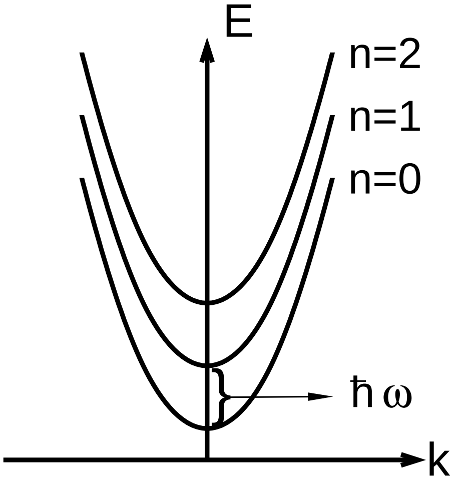

Figure 2.2: One-dimensional subbands due to the confining potential $V(z) = m\omega^2 z^2/2$

keeps the time reversal symmetry untouched and causes the spin and the momentum of the electron to couple in the following way

$$H_{SO} = \frac{e}{4m^2c^2}\left(\boldsymbol{p} \times \boldsymbol{E}\right) \cdot \boldsymbol{\sigma}. \tag{2.5}$$

In the case of free one-dimensional electrons with a perpendicular field this reads

$$H_{SO} = \alpha \sigma_z p_x, \tag{2.6}$$

where $\alpha = Ee/(4m^2c^2)$. The dispersion relation reads

$$E_R = \frac{k_x^2}{2m} \pm \alpha k_x, \tag{2.7}$$

see 2.3 b). The dispersion parabola is now shifted in momentum for the two spin directions. The situation is more complicated if more than just the lowest subband is taken into account as we will see below.

As mentioned above, there is always a perpendicular electric field present in a two-dimensional electron gas, due to a structural inversion asymmetry [27–29]. Thus the Rashba spin-orbit coupling is always present in a 2DEG and reads in two dimensions

$$H_{SO} = \alpha \left(\sigma_z p_x - \sigma_x p_z\right). \tag{2.8}$$

Via an additional external electric field the Rashba term becomes gate tunable. Additional sources for spin-orbit coupling can be present. In particular, for bulk inversion asymmetric

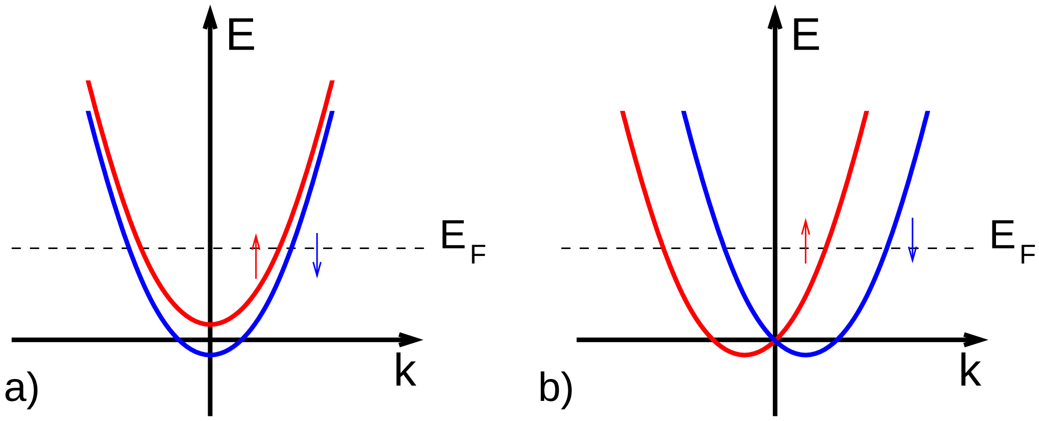

Figure 2.3: Dispersion relation of free one-dimensional electrons: a) Zeeman split bands: A magnetic field causes the dispersion relation to shift up or down in energy depending on whether the spins are aligned parallel or antiparallel to the field b) Rashba split bands: A perpendicular electric field also causes spin-orbit coupling, the shift in the dispersion relation depends on momentum and spin state

materials, the Dresselhaus term which reads

$$H_D = \beta(\sigma_z p_z - \sigma_x p_x), \tag{2.9}$$

should also be taken into account. By tuning the Rashba spin-orbit coupling (via gate voltages) to the special point $\alpha = \beta$, the spin-FET was predicted to show a remarkable insensitivity to disorder [30]. On top of these two, additional (though generally weaker) contributions may arise from the electric confinement fields forming the quantum wire. In this chapter, we focus on the case of Rashba spin-orbit coupling and disregard all other spin-orbit terms. This limit can be realized experimentally by applying sufficiently strong back-gate voltages [31–34], which create a large interfacial electric field and hence a significant and tunable Rashba spin-orbit coupling constant α. The model studied below may also be relevant to one-dimensional electron surface states, of self-assembled gold chains [35].

Treating Rashba spin-orbit coupling and the confinement together, will change the dispersions described above and the subbands will get mixed by the coupling of the spin and the orbital degree of freedom. The noninteracting theory of such a Rashba quantum wire has been discussed in the literature [20, 36–40], and is summarised below. Details are given in the next section.

We discuss electron-electron (e-e) interaction effects in the one-dimensional limit, where only the lowest (spinful) band is occupied. The bandstructure at low energy scales is then characterised by two velocities, $v_{A,B}$ [41]. These reduce to a single Fermi velocity v_F in the absence of Rashba spin-orbit coupling, but they will be different for $\alpha \neq 0$. This reflects the broken spin $SU(2)$ invariance in a spin-orbit coupled system, as reported in [42], and the velocity splitting is typically weak. While a similar velocity splitting also happens in a magnetic Zeeman field without spin-orbit coupling [43], the underlying physics is different since time-reversal symmetry is not broken by spin-orbit coupling. $\boldsymbol{p}$ and $\boldsymbol{\sigma}$ are both time-odd and hence the product is time-even.

The bandstructure of a single-channel quantum wire with Rashba spin-orbit coupling should be obtained by taking into account at least the lowest two (spinful) subbands. A restriction to the lowest subband alone would eliminate spin relaxation, see above and [20, 44, 45]. The problem in this truncated Hilbert space can be readily diagonalised, and the resulting energies yield the lowest (spinful) band relevant when describing a single-channel quantum wire.

For one-dimensional quantum wires, it is well known that the inclusion of electron-electron interactions leads to a breakdown of Fermi liquid theory, and often implies Luttinger liquid behaviour, see [46]. This non-Fermi liquid state of matter has a number of interesting features, including the phenomenon of spin-charge separation [47]. The excitations of this multi-particle system are not single electron excitations but collective charge and spin density waves. Interactions are commonly classified into different processes that describe how the electrons are scattered, such as forward or backward scattering. These different processes are then examined with renormalisation group analysis. Here, the main idea is to consider lower and lower energies and determine which processes are important and which may safely be neglected. In section 2.3 we discuss this method in detail.

Motivated mainly by the question of how the Rashba spin precession and Datta-Das oscillations are affected by e-e interactions, Rashba spin-orbit coupling effects on electronic transport in interacting quantum wires have been studied in recent papers [20,42,44,48–52]. However, all those works only took e-e forward scattering processes into account. These are interaction processes where the electrons involved are only on one side of the dispersion relation, i.e., have the same chirality. Because of the Rashba spin-orbit coupling, a modified Luttinger liquid phase with broken spin-charge separation is obtained [48, 49], leading to a drastic influence on observables. such as the spectral function or the tunnelling density of states. Moroz *et al.* [48, 49] argued that e-e backscattering processes (processes that scatter electrons from one side of the dispersion relation to the other) are irrelevant in the renormalisation group (RG) sense, and hence can be omitted in a low-energy theory [48,49]. Unfortunately, their theory relies on an incorrect spin assignment of the subbands [20, 44], which then invalidates several aspects of their treatment of interaction processes.

The possibility that e-e backscattering processes become relevant (in the RG sense) in a Rashba quantum wire was raised in [53], where a spin gap was found under a weak-coupling two-loop RG scheme. If valid, this result has important consequences for the physics of such systems, and would drive them into a spin-density-wave type state. To establish the spin gap, the authors of reference [53] start from a strictly one-dimensional single-band model and, assume both α and the e-e interaction as weak coupling constants flowing under the RG. Our approach below is different in that we include the Rashba coupling α from the outset in the single-particle sector, i.e., in a nonperturbative manner. We then consider the one-loop RG flow of all possible interaction couplings allowed by momentum conservation (for not too small α). This is an important difference to the scheme of reference [53], since the Rashba spin-orbit coupling eliminates certain interaction processes which become momentum-nonconserving. This mechanism is captured by our approach. The one-loop RG flow then turns out to be equivalent to a Kosterlitz-Thouless flow, and for the initial values realized in this problem, e-e backscattering processes are always irrelevant. Our conclusion is therefore that no spin gap arises because of the spin-orbit coupling, and a modified Luttinger liquid picture is always sufficient.

We apply our formalism to a study of the *Ruderman-Kittel-Kasuya-Yosida* (RKKY) interaction [54–58] between two spin-1/2 magnetic impurities, $\mathbf{\Sigma}_{1,2}$, separated by a distance x. This magnetic interaction is mediated by the conduction electrons in the quantum wire which are exchange-coupled (with coupling constant J) to the impurity spins. In the absence of both the e-e interaction and the spin-orbit coupling, an isotropic exchange (Heisenberg) Hamiltonian is found [57,58], where the $2k_F$-oscillatory RKKY range function $F_{\rm ex}(x) \propto \cos(2k_F x)/|x|$ is specified for the one-dimensional case. When the spin $SU(2)$ symmetry is broken by the spin-orbit coupling, spin precession sets in and the RKKY interaction is generally of a more complicated form. For a noninteracting Rashba quantum wire, it has been established [59–61] that the RKKY interaction becomes anisotropic and thus has a tensorial character. It can always be decomposed into an exchange (scalar) part, a Dzyaloshinsky-Moriya-like (vector) interaction, and an Ising-like (traceless symmetric tensor) coupling, where the different terms favour different alignment of the spin impurities. On the other hand, in the presence of e-e interactions, but without spin-orbit coupling, the range function has been shown [62, 63] to exhibit a slow power-law decay, $F_{\rm ex}(x) \propto \cos(2k_F x)|x|^{-\eta}$, with an interaction-dependent exponent $\eta < 1$. The RKKY interaction in interacting quantum wires with spin-orbit coupling has not been studied before.

This chapter is organised in the following way. In section 2.2 we discuss the bandstructure in the one particle picture. Interaction processes are then discussed in section 2.3, including a second-order, i.e., one-loop, renormalisation group analysis, while in section 2.4 we first introduce the Luttinger liquid concept in section 2.4.1, and then apply it to the interacting quantum wire with spin-orbit coupling in section 2.4.2. In section 2.5 we similarly first introduce the general concept of the RKKY interaction in section 2.5.1, to then apply it in our system in section 2.5.2. Finally we offer some conclusions in section 2.6.

2.2 One particle picture of a quantum wire with spin-orbit coupling

In this section we introduce the one particle Hamiltonian for free electrons with spin-orbit coupling in one dimension. We are considering a quantum wire that is confined in a two-dimensional electron gas (2DEG). Due to the tunable effective electric field in y-direction, the Rashba spin-orbit coupling must be included. A schematic picture of the setup is shown in figure 2.1. The noninteracting problem is then defined by the single-particle Hamiltonian [20, 27, 36, 37, 39]

$$H_{sp} = H_{2DEG} + V(z) + H_{SO}, \tag{2.10}$$

where

$$H_{2DEG} = \frac{1}{2m}\left(p_x^2 + p_z^2\right), \tag{2.11}$$

describes free electrons in the two-dimensional electron gas. The confinement reads

$$V(z) = \frac{m}{2}\omega^2 z^2. \tag{2.12}$$

The Rashba term in this case reads

$$H_{SO} = \alpha\left(\sigma_z p_x - \sigma_x p_z\right), \tag{2.13}$$

where $\alpha \propto E$ is the Rashba coupling and the Pauli matrices $\sigma_{x,z}$ act in spin space. For $\alpha = 0$, the transverse problem is diagonal in terms of the familiar one-dimensional harmonic oscillator eigenstates (Hermite functions) $H_n(z)$, with $n = 0, 1, 2, \ldots$ labelling the subbands. Eigenstates of equation (2.10) have conserved longitudinal momentum $p_x = k$, thereby stating $\hbar = 1$. With the z-direction as spin quantisation axis, $\sigma_z|\sigma\rangle = \sigma|\sigma\rangle$, where $\sigma = \uparrow, \downarrow = \pm$, the $\sigma_x p_z$ term implies mixing of adjacent subbands with associated spin flips. Retaining only the lowest ($n = 0$) subband from the outset thus excludes spin relaxation, as seen above. We follow reference [20] and keep the two lowest bands, $n = 0$ and $n = 1$. The higher subbands $n \geq 2$ yield only tiny corrections, which can in principle be included as in reference [39]. The resulting 4×4 matrix representing $\tilde{H}_{\mathrm{sp}}$ in this truncated Hilbert space then reads

$$\tilde{H}_{sp} = \begin{pmatrix} \frac{\omega}{2} + \frac{k^2}{2m} + \alpha k & 0 & 0 & i\alpha\sqrt{\frac{m\omega}{2}} \\ 0 & \frac{\omega}{2} + \frac{k^2}{2m} - \alpha k & i\alpha\sqrt{\frac{m\omega}{2}} & 0 \\ 0 & -i\alpha\sqrt{\frac{m\omega}{2}} & \frac{3\omega}{2} + \frac{k^2}{2m} + \alpha k & 0 \\ -i\alpha\sqrt{\frac{m\omega}{2}} & 0 & 0 & \frac{3\omega}{2} + \frac{k^2}{2m} - \alpha k \end{pmatrix}, \tag{2.14}$$

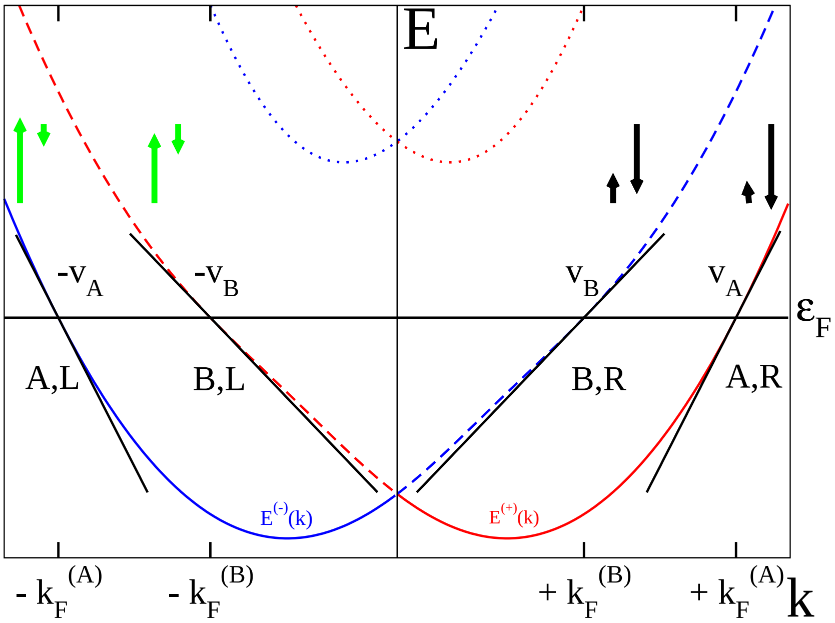

Figure 2.4: Schematic band structure (2.15) of a typical one-dimensional Rashba quantum wire. The red/blue curves show the $s = \pm$ bands, and the dotted curves indicate the next subband (the Fermi energy ϵ_F is assumed below that band). For the low-energy description, we linearise the dispersion. It is notationally convenient to introduce bands A (solid lines) and B (dashed lines). Green and black arrows indicate the respective spin amplitudes (exaggerated). The resulting Fermi momenta are $\pm k_F^{(A,B)}$, with Fermi velocities $v_{A,B}$.

which is readily diagonalised and yields four energy bands. We choose the Fermi energy such that only the lower two bands, labelled by $s = \pm$, are occupied, and arrive at a reduced two-band model, where the quantum number $s = \pm$ replaces the spin quantum number. The dispersion relation is

$$E_s(k) = \omega + \frac{k^2}{2m} - \sqrt{\left(\frac{\omega}{2} + s\alpha k\right)^2 + \frac{m\omega\alpha^2}{2}}, \tag{2.15}$$

with eigenfunctions $\sim e^{ikx}\phi_{k,s}(z)$. The resulting asymmetric energy bands (2.15) are shown in figure 2.4. The transverse spinors (in spin space) are given by

$$\begin{aligned} \phi_{k,+}(z) &= \begin{pmatrix} i\cos[\theta_+(k)]H_1(z) \\ \sin[\theta_+(k)]H_0(z) \end{pmatrix}, \qquad (2.16) \\ \phi_{k,-}(z) &= \begin{pmatrix} \sin[\theta_-(k)]H_0(z) \\ i\cos[\theta_-(k)]H_1(z) \end{pmatrix}, \end{aligned}$$

with k-dependent spin rotation angles (we take $0 \leq \theta_s(k) \leq \pi/2$)

$$\theta_s(k) = \frac{1}{2}\cot^{-1}\left(\frac{-2sk - \omega/\alpha}{\sqrt{2m\omega}}\right) = \theta_{-s}(-k). \tag{2.17}$$

As a result of subband mixing, the two spinor components of $\phi_{k,s}(z)$ carry a different z-dependence. They are therefore not just the result of a $SU(2)$ rotation. For $\alpha = 0$, we recover $\theta_s = \pi/2$, corresponding to the usual spin up and down eigenstates, with $H_0(z)$ as transverse wavefunction. The $s = +$ ($s = -$) component then describes the $\sigma =\downarrow$ ($\sigma =\uparrow$) spin eigenstate. However, for $\alpha \neq 0$, a peculiar implication of the Rashba spin-orbit coupling follows. From equation (2.17) we have $\lim_{k\to\pm\infty}\theta_s(k) = (1 \pm s)\pi/4$, such that both $s = \pm$ states have (approximately) spin $\sigma =\downarrow$ for $k \to \infty$ but $\sigma =\uparrow$ for $k \to -\infty$; the product of spin and chirality thus always approaches $\sigma \mathrm{sgn}(k) = -1$. Moreover, under the time-reversal transformation, $\mathcal{T} = i\sigma_y\mathcal{C}$ with the complex conjugation operator $\mathcal{C}$, the two subbands are exchanged,

$$e^{-ikx}\phi_{-k,-s}(z) = s\mathcal{T}[e^{ikx}\phi_{k,s}(z)], \quad E_{-s}(-k) = E_s(k). \tag{2.18}$$

Time-reversal symmetry, preserved in the truncated description, makes this two-band model of a Rashba quantum wire qualitatively different from Zeeman spin-split models [43].

In the next step, since we are interested in the low-energy physics, we linearise the dispersion relation around the Fermi points $\pm k_F^{(A,B)}$, see figure 2.4, which results in two velocities v_A and v_B, see [41],

$$v_{A,B} = v_F(1 \pm \delta), \quad \delta(\alpha) \propto \alpha^4. \tag{2.19}$$

These reduce to a single Fermi velocity v_F in the absence of Rashba spin-orbit coupling ($\delta = 0$ for $\alpha = 0$). The linearisation of the dispersion relation is known to be an excellent approximation for weak e-e interaction [46, 47]. Explicit values for δ in equation (2.19) can be derived from equation (2.15), and we find $\delta(\alpha) \propto \alpha^4$ for $\alpha \to 0$, in accordance with previous estimates [42]. We mention that $\delta \lesssim 0.1$ has been estimated for typical geometries in reference [49]. The transverse spinors $\phi_{ks}(z)$, equation (2.16), entering the low-energy description can be taken at $k = \pm k_F^{(A,B)}$, where the spin-rotation angle (2.17) only assumes one of the two values

$$\theta_A = \theta_+\left(k_F^{(A)}\right), \quad \theta_B = \theta_-\left(k_F^{(B)}\right). \tag{2.20}$$

The electron field operator $\Psi(x, z)$ for the linearised two-band model with $\nu = A, B = +, -$ can then be expressed in terms of one-dimensional fermionic field operators $\psi_{\nu,r}(x)$, where

$r = R, L = +, -$ labels right- and left-movers,

$$\Psi(x,z) = \sum_{\nu,r=\pm} e^{irk_F^{(\nu)}x} \; \phi_{rk_F^{(\nu)},s=\nu r}(z) \; \psi_{\nu,r}(x), \tag{2.21}$$

with $\phi_{k,s}(z)$ specified in equation (2.16). Note that in the left-moving sector, band indices have been interchanged according to the labelling in figure 2.4.

In this way, the noninteracting second-quantised Hamiltonian takes the standard form for two inequivalent species of one-dimensional massless Dirac fermions with different velocities,

$$H_0 = -i \sum_{\nu,r=\pm} r v_\nu \int dx \; \psi^\dagger_{\nu,r} \partial_x \psi_{\nu,r}. \tag{2.22}$$

Note that the linearised picture is only valid at low energies. So we restrict the momentum to be smaller than a cutoff, $k < \Lambda$. For x this means the smallest distance taken into account here is $|x| > a > 0$, where $a \propto 1/\Lambda$. The velocity difference displays the breaking of the spin $SU(2)$ symmetry, a direct consequence of spin-orbit coupling. For $\alpha = 0$, the index ν coincides with the spin quantum number σ for left-movers and with $-\sigma$ for right-movers, and the above formulation reduces to the usual Hamiltonian for a spinful single-channel quantum wire.

2.3 Interaction effects and RG analysis

We now include e-e interactions in such a single-channel disorder-free Rashba quantum wire. With the expansion (2.21) and $\mathbf{r} = (x,z)$, the second-quantised two-body Hamiltonian

$$H_I = \frac{1}{2} \int d\mathbf{r}_1 d\mathbf{r}_2 \; \Psi^\dagger(\mathbf{r}_1)\Psi^\dagger(\mathbf{r}_2)V(\mathbf{r}_1 - \mathbf{r}_2)\Psi(\mathbf{r}_2)\Psi(\mathbf{r}_1), \tag{2.23}$$

leads to one-dimensional interaction processes. We here assume that the e-e interaction potential $V(\mathbf{r}_1 - \mathbf{r}_2)$ is externally screened, allowing the one-dimensional interactions to be described as effectively local. Using (2.21) and defining relative and centre of mass coordinates $x = x_1 - x_2$ and $X = x_1 + x_2$ we find

$$\begin{aligned} H_I &= \frac{1}{2} \sum_{\nu_i, r_i} \int dx \int dz_1 \int dz_2 V(x, z_1 - z_2) e^{-iq_- \frac{x}{2}} \\ &\quad \times \left[\phi^\dagger_{r_1 k_F^{(\nu_1)}, \nu_1 r_1} \cdot \phi_{r_4 k_F^{(\nu_4)}, \nu_4 r_4} \right](z_1) \left[\phi^\dagger_{r_2 k_F^{(\nu_2)}, \nu_2 r_2} \cdot \phi_{r_3 k_F^{(\nu_3)}, \nu_3 r_3} \right](z_2) \\ &\quad \times \int dX e^{-iq_+ X} \psi^\dagger_{\nu_1, r_1}\left(X + \frac{x}{2}\right) \psi^\dagger_{\nu_2, r_2}\left(X - \frac{x}{2}\right) \psi_{\nu_3, r_3}\left(X - \frac{x}{2}\right) \psi_{\nu_4, r_4}\left(X + \frac{x}{2}\right), \end{aligned} \tag{2.24}$$

where

$$\begin{aligned} q_+ &= r_1 k_F^{\nu_1} + r_2 k_F^{\nu_2} - r_3 k_F^{\nu_3} - r_4 k_F^{\nu_4}, && (2.25)\\ q_- &= r_1 k_F^{\nu_1} - r_2 k_F^{\nu_2} + r_3 k_F^{\nu_3} - r_4 k_F^{\nu_4}. && (2.26)\end{aligned}$$

Next we expand the fermion operators in orders of x: $\psi_{\nu,r}(X \pm x/2) = \psi_{\nu,r}(X) \pm \mathcal{O}(x)$, where the higher order terms contain spatial derivatives, which makes the four fermion operators irrelevant in the RG sense. The additional spatial dimension in ∂_x will reduce the scaling dimension such that the operator will always flow to zero in the RG flow. This leaves us with

$$\begin{aligned} H_I &= \frac{1}{2}\sum_{\nu_i, r_i} \int dx \int dz_1 \int dz_2 V(x, z_1 - z_2) e^{-iq_- \frac{x}{2}} \\ &\times \left[\phi^\dagger_{r_1 k_F^{(\nu_1)}, \nu_1 r_1} \cdot \phi_{r_4 k_F^{(\nu_4)}, \nu_4 r_4}\right](z_1) \left[\phi^\dagger_{r_2 k_F^{(\nu_2)}, \nu_2 r_2} \cdot \phi_{r_3 k_F^{(\nu_3)}, \nu_3 r_3}\right](z_2) \qquad (2.27)\\ &\times \int dX e^{-iq_+ X} \psi^\dagger_{\nu_1, r_1}(X)\, \psi^\dagger_{\nu_2, r_2}(X)\, \psi_{\nu_3, r_3}(X)\, \psi_{\nu_4, r_4}(X)\,. \end{aligned}$$

We now assume that the four fermion operator in the last line of equation (2.27) varies in X slowly on a length scale $1/k_F^{(\nu)}$, because of the short-distance/large-momentum cutoff used in the linearisation process. Thus we can approximate

$$\begin{aligned} &\int dX e^{-iq_+ X} \psi^\dagger_{\nu_1, r_1}(X)\, \psi^\dagger_{\nu_2, r_2}(X)\, \psi_{\nu_3, r_3}(X)\, \psi_{\nu_4, r_4}(X) \\ &\simeq \delta_{q_+, 0} \int dX \psi^\dagger_{\nu_1, r_1}(X)\, \psi^\dagger_{\nu_2, r_2}(X)\, \psi_{\nu_3, r_3}(X)\, \psi_{\nu_4, r_4}(X)\,, \qquad (2.28)\end{aligned}$$

where the Kronecker-δ denotes the momentum conservation

$$r_1 k_F^{(\nu_1)} + r_2 k_F^{(\nu_2)} = r_3 k_F^{(\nu_3)} + r_4 k_F^{(\nu_4)}. \qquad (2.29)$$

We then obtain the local one-dimensional interaction Hamiltonian [64]

$$H_I = \frac{1}{2}\sum_{\{\nu_i, r_i\}} V_{\{\nu_i, r_i\}} \int dx\ \psi^\dagger_{\nu_1, r_1} \psi^\dagger_{\nu_2, r_2} \psi_{\nu_3, r_3} \psi_{\nu_4, r_4}, \qquad (2.30)$$

where the summation runs over all quantum numbers $\nu_1, \ldots, \nu_4$ and $r_1, \ldots, r_4$ and is subject to momentum conservation (2.29). With the momentum transfer $q_- = r_1 k_F^{(\nu_1)} - r_4 k_F^{(\nu_4)}$ and the partial Fourier transform

$$\tilde{V}(q_-; z) = \int dx\ e^{-iq_- x} V(x, z) \qquad (2.31)$$

of the interaction potential, the interaction matrix elements in equation (2.30) are given by

$$\begin{aligned} V_{\{\nu_i,r_i\}} &= \int dz_1 dz_2 \; \tilde{V}(q_-; z_1 - z_2) \\ &\times \left[\phi^{\dagger}_{r_1 k_F^{(\nu_1)}, \nu_1 r_1} \cdot \phi_{r_4 k_F^{(\nu_4)}, \nu_4 r_4} \right](z_1) \left[\phi^{\dagger}_{r_2 k_F^{(\nu_2)}, \nu_2 r_2} \cdot \phi_{r_3 k_F^{(\nu_3)}, \nu_3 r_3} \right](z_2). \end{aligned} \tag{2.32}$$

Since the Rashba spin-orbit coupling produces a splitting of the Fermi momenta for the two bands, $\left| k_F^{(A)} - k_F^{(B)} \right| \simeq 2\alpha m$, the condition (2.29) eliminates one important interaction process available for $\alpha = 0$, namely interband backscattering. This is a distinct spin-orbit coupling effect besides the broken spin $SU(2)$ invariance. Obtaining the complete *g-ology* classification [47] of all possible interaction processes allowed for $\alpha \neq 0$ is then a straightforward exercise, see figures 2.5 to 2.8. The corresponding values of the interaction matrix elements are generally difficult to evaluate explicitly, but in the most important case of a thin wire,

$$d \gg \frac{1}{\sqrt{m\omega}}, \tag{2.33}$$

where d is the screening length (representing, e.g., the distance to a back-gate), analytical expressions can be obtained. Note that equation (2.33) excludes the case of ultra-local contact interactions. To simplify the analysis and allow for analytical progress, we therefore employ the thin-wire approximation (2.33) in what follows. In that case, we can neglect the z dependence in equation (2.31). Going beyond this approximation would only imply slightly modified values for the e-e interaction couplings used below. Using the identity

$$\int dz \; \left[\phi^{\dagger}_{r k_F^{(\nu)}, \nu r} \cdot \phi_{r' k_F^{(\nu')}, \nu' r'} \right](z) = \delta_{\nu\nu'} \delta_{rr'} + \cos(\theta_A - \theta_B) \delta_{\nu,-\nu'} \delta_{r,-r'}, \tag{2.34}$$

where the angles $\theta_{A,B}$ were specified in equation (2.20), only two different values W_0 and W_1 for the matrix elements in equation (2.32) emerge. These nonzero matrix elements are

$$\begin{aligned} V_{\nu r, \nu' r', \nu' r', \nu r} &\equiv W_0 = \tilde{V}(q = 0), \\ V_{\nu r, \nu' r', -\nu' -r', -\nu -r} &\equiv W_1 = \cos^2(\theta_A - \theta_B) \; \tilde{V}\left(q = k_F^{(A)} + k_F^{(B)} \right). \end{aligned} \tag{2.35}$$

We then introduce one-dimensional chiral fermion densities $\rho_{\nu r}(x) = \, : \psi^{\dagger}_{\nu r} \psi_{\nu r} :$, where the colons indicate normal-ordering, i.e., destruction operators are moved to the right and creation operators to the left. The interacting one-dimensional Hamiltonian is $H =$

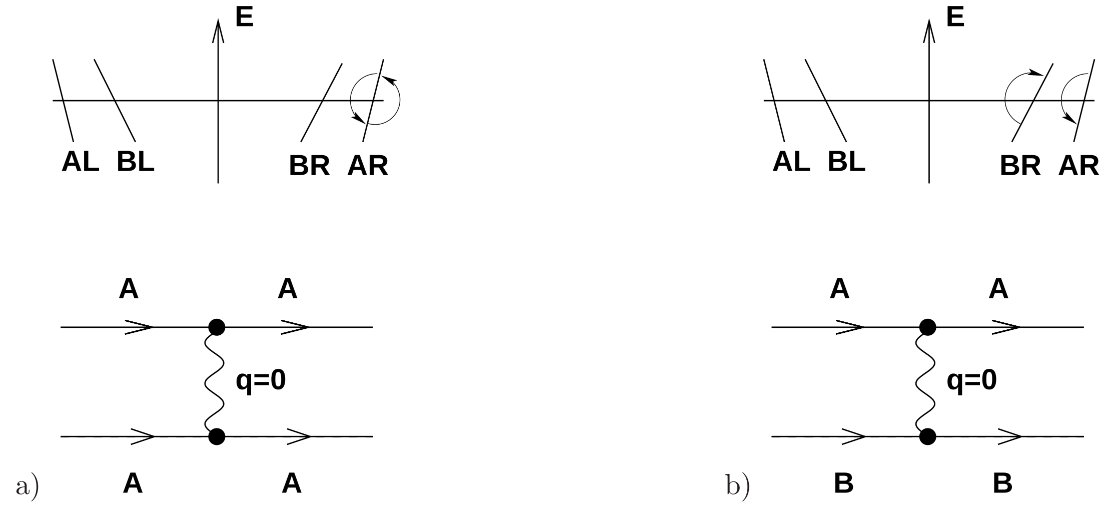

Figure 2.5: Schematic view and Feynman diagram of the interaction processes (solid lines indicate right movers and dashed lines left movers). a) $g_{4\|A}$, which couples only fermions on the same branch (analogous for B), describing forward scattering and b) $g_{4\perp}$, in which the coupled fermions are still on the same side of the Fermi surface but couple different branches A and B. The momentum transfer in both cases is close to zero, thus the coupling constant for these processes is $W_0 = \tilde{V}(q=0)$.

$H_0 + H_I$ with equation (2.22) and

$$\begin{aligned} H_I &= \frac{1}{2}\sum_{\nu\nu',rr'}\int dx\Big([g_{2\|\nu}\delta_{\nu,\nu'} + g_{2\perp}\delta_{\nu,-\nu'}]\delta_{r,-r'} + [g_{4\|\nu}\delta_{\nu,\nu'} + g_{4\perp}\delta_{\nu,-\nu'}]\delta_{r,r'}\Big)\ \rho_{\nu r}\rho_{\nu' r'} \\ &\quad + \frac{g_f}{2}\sum_{\nu r}\int dx\ \psi^\dagger_{\nu r}\psi^\dagger_{\nu,-r}\psi_{-\nu r}\psi_{-\nu,-r}. \end{aligned} \tag{2.36}$$

The e-e interaction couplings are denoted in analogy to the standard g-ology, whereby the g_4 (g_2) processes describe forward scattering of one-dimensional fermions with equal (opposite) chirality ($r = R, L = +, -$), see figure 2.5, 2.6, and 2.7 a), and the labels $\|$, $\perp$, and f denote intraband, interband, and band flip processes, respectively. Since the bands ($\nu = A, B = +, -$) are inequivalent, we keep track of the band index in the intraband couplings. The g_f term corresponds to intraband backscattering with band flip, see figure 2.7 b). The interband backscattering without band flip is strongly suppressed since it does not conserve total momentum and is neglected in the following. It is in principle possible that such a process becomes important if a collective density readjustment between subbands takes place in the wire. However, this can only happen for almost equivalent subbands, see reference [64] for a detailed discussion.

Here we assume that the spin-orbit coupling is strong enough to guarantee that such a readjustment does not occur. For $\alpha = 0$, the $g_{4,\|/\perp}$ couplings coincide with the usual

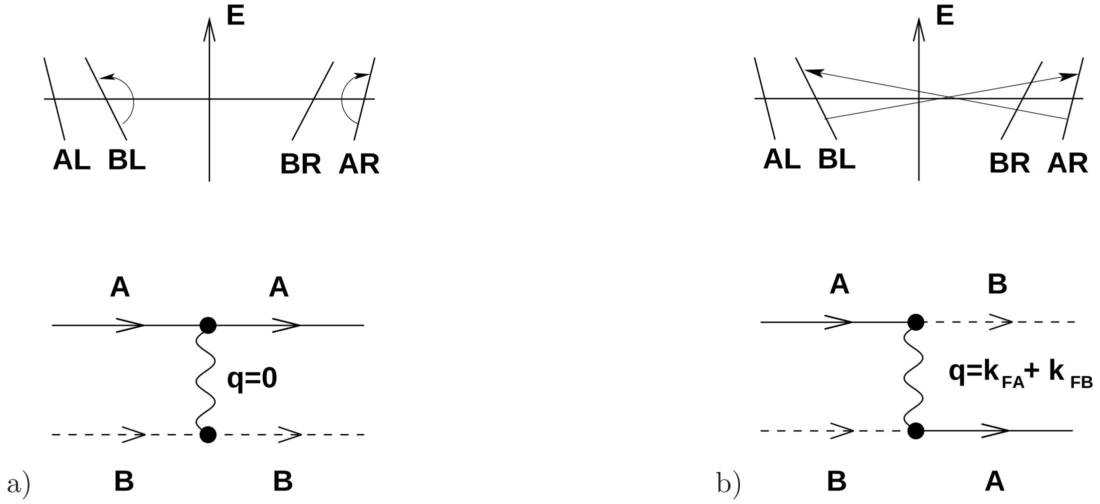

Figure 2.6: Schematic view and Feynman diagram of the interaction processes (solid lines indicate right movers and dashed lines left movers). the $g_{2\perp}$ consists of two contributions that have the same operator structure after commuting the fermions a) $W_0 = \tilde{V}(q = 0)$. b) $W_1 = \cos^2(\theta_A - \theta_B)\tilde{V}(q = k_F^{(A)} + k_F^{(B)})$. Commutation of the fermions gives the minus sign in equation (2.37).

ones [47] for spinful electrons, while g_f reduces to $g_{1\perp}$ and $g_{2,\|/\perp}$ to $g_{2,\perp/\|}$ due to our exchange of band indices in the left-moving sector. According to equation (2.35), the bare values of these coupling constants are

$$g_{4\|\nu} = g_{4\perp} = g_{2\|\nu} = W_0, \quad g_{2\perp} = W_0 - W_1, \quad g_f = W_1. \tag{2.37}$$

The corresponding processes are visualised in figures 2.5 to 2.7. The equality of the intra-band coupling constants for the two bands is a consequence of the thin-wire approximation, which also eliminates certain exchange matrix elements, see figure 2.8.

An abbreviation for the four fermion operators that corresponds to the processes found above to simplify the renormalisation group analysis is defined as

$$O_{2\|\nu}(x) = \frac{1}{2}\sum_r \rho_{\nu r}(x)\rho_{\nu -r}(x) \tag{2.38}$$

$$O_{2\perp}(x) = \frac{1}{2}\sum_{r,\nu} \rho_{\nu r}(x)\rho_{-\nu -r}(x) \tag{2.39}$$

$$O_{4\|\nu}(x) = \frac{1}{2}\sum_r \rho_{\nu r}(x)\rho_{\nu r}(x) \tag{2.40}$$

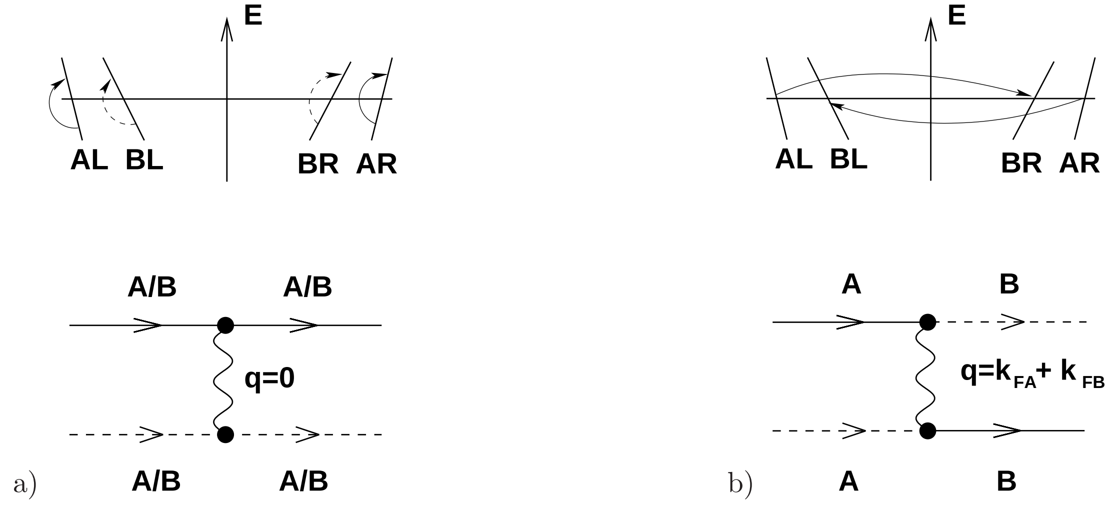

Figure 2.7: Schematic view and Feynman diagram of the interaction processes (solid lines indicate right movers and dashed lines left movers). a) $g_{2\|\nu}$ the transferred momentum is close to zero, hence the coupling is $W_0 = \tilde{V}(q = 0)$. b) g_f corresponds to intra band scattering with band flip. For the coupling on finds $W_1 = \cos^2(\theta_A - \theta_B)\tilde{V}(q = k_F^{(A)} + k_F^{(B)})$.

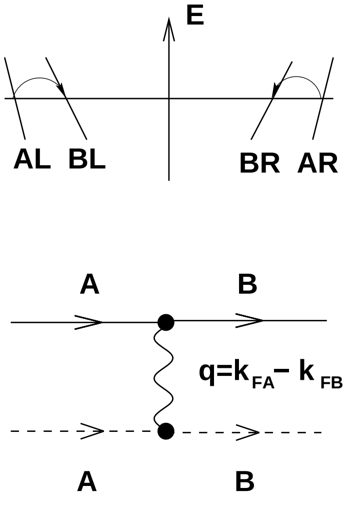

Figure 2.8: Example for a term that would be possible from a momentum conservation point of view and contribute to g_f, the momentum transfer would equal the difference between the two Fermi points $k_F^{(A)} - k_F^{(B)}$. The thin wire approximation, though, kills this term since equation (2.34) contains exchange integral between the harmonic oscillator functions $H_0(z)$ and $H_1(z)$, which are orthogonal and thus the integral is zero. (Solid lines indicate right movers and dashed lines left movers.)

$$\begin{aligned} O_{4\perp}(x) &= \frac{1}{2}\sum_{r,\nu} \rho_{\nu r}(x)\rho_{-\nu r}(x) && (2.41)\\ O_f(x) &= \frac{1}{2}\sum_{\nu r} \psi^\dagger_{\nu r}(x)\psi^\dagger_{\nu,-r}(x)\psi_{-\nu r}(x)\psi_{-\nu,-r}(x). && (2.42) \end{aligned}$$

Our interaction Hamiltonian can now be cast as

$$H_I = \sum_j g_j \int dx\, O_j(x). \tag{2.43}$$

We will now investigate the remaining coupling constants in a renormalisation group (RG) sense. The main idea behind RG is that we want to know the properties of the system at very low energies. In the linearisation process we used a cutoff Λ to restrict our theory to the linear low energy regime, with $v_F k \leq k_B T < \Lambda$. The physics of the system should not depend on the actual value of Λ. Therefore, we lower the cutoff iteratively and change the coupling constants in a way that the physics, i.e., the partition function stays the same. In appendix A we give a detailed derivation of the second order RG equations.

The Hamiltonian $H_0 + H_I$ then corresponds to a specific realization of a general asymmetric two band-model, where the one-loop RG equations are known [64, 65]. Using RG invariants (A.26) to (A.28), we arrive after some algebra, see appendix A, at the two-dimensional Kosterlitz-Thouless RG flow equations,

$$\frac{d\bar{g}_2}{dl} = -\bar{g}_f^2, \quad \frac{d\bar{g}_f}{dl} = -\bar{g}_f\bar{g}_2, \tag{2.44}$$

for the rescaled couplings

$$\begin{aligned} \bar{g}_2 &= \frac{g_{2\parallel A}}{2\pi v_A} + \frac{g_{2\parallel B}}{2\pi v_B} - \frac{g_{2\perp}}{\pi v_F}, && (2.45)\\ \bar{g}_f &= \sqrt{\frac{1+\gamma}{2}}\frac{g_f}{\pi v_F}, \end{aligned}$$

where we use the dimensionless constant

$$\gamma = \frac{v_F^2}{v_A v_B} = \frac{1}{1-\delta^2} \geq 1. \tag{2.46}$$

As usual, the g_4 couplings do not contribute to the one-loop RG equations. The initial values of the couplings can be read off from equation (2.37),

$$\begin{aligned} \bar{g}_2(l=0) &= \frac{(\gamma-1)W_0 + W_1}{\pi v_F}, \\ \bar{g}_f(l=0) &= \sqrt{\frac{1+\gamma}{2}}\frac{W_1}{\pi v_F}. && (2.47) \end{aligned}$$

The solution of Eq. (2.44) is textbook material [47], and $\bar{g}_f$ is known to be marginally irrelevant for all initial conditions with $|\bar{g}_f(0)| \leq \bar{g}_2(0)$. Using equations (2.35) and (2.47), this implies with $\gamma \simeq 1 + \delta^2$ the condition

$$\tilde{V}(0) \geq \frac{1}{4} \cos^2(\theta_A - \theta_B)\ \tilde{V}\left(k_F^{(A)} + k_F^{(B)}\right), \tag{2.48}$$

which is satisfied for all physically relevant repulsive e-e interaction potentials. As a consequence, intraband backscattering processes with band flip, described by the coupling $\bar{g}_f$, are always marginally irrelevant, i.e., they flow to zero coupling as the energy scale is reduced, $\bar{g}_f^* = \bar{g}_f(l \to \infty) = 0$. Therefore no gap arises, and a modified Luttinger liquid model is the appropriate low-energy theory. We mention in passing that even if we neglect the velocity difference in Eq. (2.19), no spin gap is expected in a Rashba wire, i.e., the broken $SU(2)$ invariance in our model is not required to establish the absence of a gap.

The above RG procedure also allows us to extract renormalised couplings entering the low-energy Luttinger liquid description. The fixed-point value $\bar{g}_2^* = \bar{g}_2(l \to \infty)$ now depends on the Rashba spin-orbit coupling through γ in equation (2.46). With the interaction matrix elements $W_{0,1}$ in equation (2.35), it is given by

$$\bar{g}_2^* = \frac{\sqrt{[(\gamma - 1)W_0 + W_1]^2 - (\gamma + 1)W_1^2/2}}{\pi v_F}. \tag{2.49}$$

For $\alpha = 0$, we have $\gamma = 1$ and therefore $\bar{g}_2^* = 0$. The Rashba spin-orbit coupling produces the nonzero fixed-point value (2.49), reflecting the broken $SU(2)$ symmetry.

2.4 Luttinger liquid description

As mentioned above, we used a modified Luttinger liquid model to describe our system. In the next section we summarise the key points of the Luttinger liquid theory before we apply this theory to our system in section 2.4.2.

2.4.1 Luttinger liquid for a one-dimensional interaction electron gas

Let us start with a graphic argument before we construct a rigid mathematical theory and look at two- and one-dimensional interacting electrons. In two (or more) dimensions interacting electrons are very well described by the *Fermi liquid* theory, see e.g., [46]. The main idea in Fermi liquid theory is that the electrons can be described as quasi particles, electrons that are dressed with a charged cloud of other electrons. These quasi particles are essentially free and behave almost like free electrons. This is why it is possible to describe many properties of metals in the noninteracting Fermi gas theory. The situation in one dimension drastically changes. If an electron is confined to one dimension it does

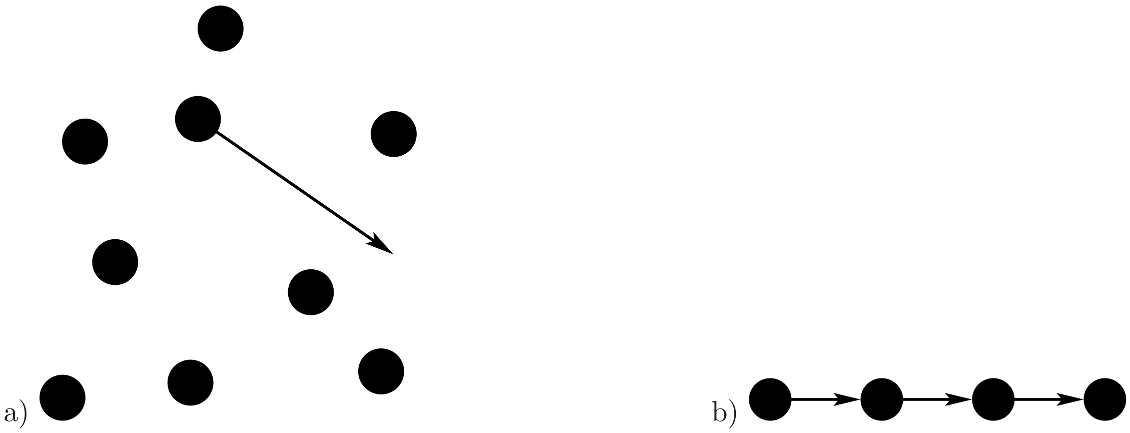

Figure 2.9: a) In higher dimensions quasi free excitations are possible. One can define quasi particles that essentially behave like free electrons, but b) in one dimension every excitation in an interacting system has to be collective.

not simply pass its neighbours but drags its neighbours along, see figure 2.9. Hence, in one dimension, single particle states are suppressed and only collective excitations are possible. Mathematically this is captured in the so called Luttinger liquid theory, which describes a mapping between the fermionic representation and a bosonic picture, which describes the collective modes. Since the spin part of the particle interacts with a different strength than the charge part, we find the astonishing result of spin-charge separation, where the two collective modes either carry charge or spin.

Let us now introduce the mathematical framework called *bosonisation*. Bosonisation refers to the possibility of describing fermions obeying standard anti-commutations rules in terms of bosonic degrees of freedom which obey standard commutation rules. This is in principle possible in all dimensions, but it has only proved useful in $d = 1$, as only in this case the bosonic version of the given fermionic theory is local and simple, often simpler than the fermionic theory. Here we only illustrate this equivalence by giving the main identities, for more details see appendix B.

A fermionic one-dimensional spinful system is described by the Hamiltonian

$$H_f = \sum_{\sigma\nu} \int dx \; \psi^\dagger_{\sigma\nu}(-i\nu\partial_x)\psi_{\sigma\nu}, \tag{2.50}$$

which is equivalent to a bosonic theory with the Hamiltonian

$$H_b = \frac{v}{2} \int \sum_{\sigma\nu} dx \; \left(\partial_x \phi_{\sigma\nu}\right)^2 , \tag{2.51}$$

where $\nu = R/L$ is the chirality and when used in a mathematical formula $\nu = +/-$. The key formula is given by

$$\psi_{\sigma\nu}(x) = \frac{\eta_{\sigma\nu}}{\sqrt{2\pi a}} e^{i\nu\phi_{\sigma\nu}(x)}, \tag{2.52}$$

where a is a small length cutoff that needs to be understood as the smallest length scale in the system. It is needed to eliminate divergences due to the infinite linear spectrum. The Klein factors $\eta_{\sigma\nu}$ and $\eta^\dagger_{\sigma\nu}$ are fermionic operators without dynamics, that obey $\eta_{\sigma\nu} = \eta^\dagger_{\sigma\nu}$ and $\{\eta_{\sigma\nu}, \eta_{\sigma'\nu'}\} = 2\delta_{\nu\nu'}\delta_{\sigma\sigma'}$, see also [47,62,63]. We now include forward scattering which is given by the interaction Hamiltonian

$$H_{int} \simeq \frac{1}{2} \sum_{\sigma\sigma'} \sum_{\nu\nu'} \int dx \rho_{\sigma\nu} V_0 \rho_{\sigma'\nu'}, \tag{2.53}$$

where $\rho_{\sigma\nu} = \psi^\dagger_{\sigma\nu}\psi_{\sigma\nu}$. The bosonic form of the Hamiltonian then reads

$$H_{int} = \frac{V_0}{8\pi^2} \int dx \left(\sum_{\nu\sigma} \partial_x \phi_{\sigma\nu} \right)^2 . \tag{2.54}$$

Non chiral charge and spin fields are defined as $\phi_{c,s} = (\sum_\nu \phi_{\uparrow\nu} \pm \sum_\nu \phi_{\downarrow\nu})/\sqrt{8\pi}$ and their conjugate phase fields $\theta_{c,s} = (\phi_{\uparrow L} - \phi_{\uparrow R} \pm [\phi_{\downarrow L} - \phi_{\downarrow R}])/\sqrt{8\pi}$, where the upper sign refers to the charge fields (index c) and the lower sign to the spin fields (index s). Moreover, the canonically conjugated momentum of $\phi_{c,s}$ is given as $\Pi_{c,s} = \partial_x \theta_{c,s}$, where ϕ_j and Π_i obey canonical commutation relations

$$[\phi_i(x), \Pi_j(y)] = i\delta_{i,j}\delta(x-y), \qquad i,j = s,c. \tag{2.55}$$

In this basis the Hamiltonian is diagonal in charge and spin fields and reads

$$\begin{aligned} H &= H_c + H_s, && (2.56)\\ H_c &= \frac{v_c}{2} \int dx \frac{1}{K} (\partial_x \phi_c)^2 + K\Pi_c^2, && (2.57)\\ H_s &= \frac{v_s}{2} \int dx (\partial_x \phi_s)^2 + \Pi_s^2, && (2.58) \end{aligned}$$

where $K^{-1} = \sqrt{1 + \frac{2V_0}{\pi v_F}}$ is the Luttinger liquid parameter, $v_c = v_F/K$ and $v_s = v_F$. $K = 1$ corresponds to the non-interacting case. For $K < 1$ this describes the case of repulsively interacting electrons. If the interaction is attractive, $K > 1$. For a detailed derivation of the Hamiltonian (2.56) and the resulting correlation functions see appendix B. The Hamiltonian (2.56) describes long wavelength oscillations of the charge and the spin density, with a linear dispersion relation $\omega_{c,s} = v_{c,s}|q|$. The system is conducting and the physical excitations are charge-density waves and spin-density waves. From the different

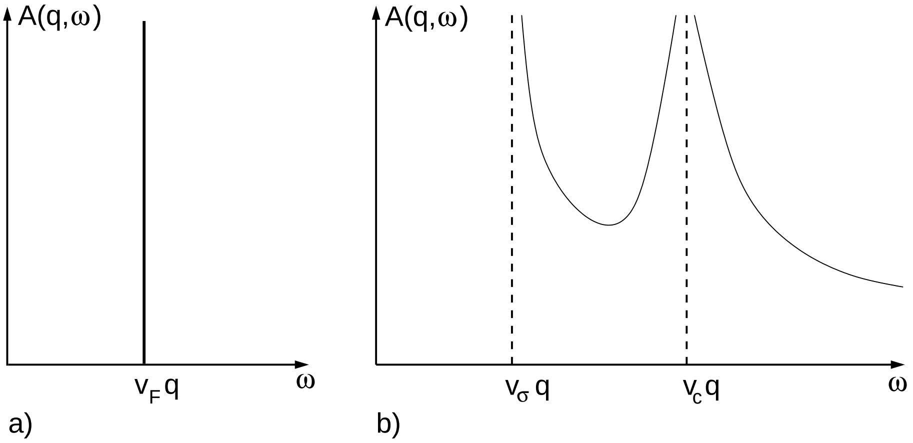

Figure 2.10: Schematic view of the spectral function of one-dimensional electrons. a) Free noninteracting electrons. The spectral function is a simple delta peak at $\omega = v_F q$ indicating the true single particle excitation. b) Interacting electrons described by the Luttinger liquid theory. Instead of a delta function one finds two divergencies corresponding to the charge density waves ($v_c q = \omega$) and spin density waves ($v_\sigma q = \omega$) with different power laws. So no single particle excitation can exist in a Luttinger liquid.

velocities it is obvious that these two excitations travel with different speed. The spectral function of free electrons is a delta function, indicating a single particle excitation. In a Luttinger liquid the spectral function has two divergencies with different power laws, see figure 2.10 and [66]. A single particle excitation can not exit in a Luttinger liquid. Consequently, in one dimension the electron can not exit as one particle with spin and charge, and splits into two independent excitations carrying spin or charge respectively. The most important feature of (2.56) is that an interacting fermionic system can be described in terms of a free non-interacting quadratic bosonic theory.

2.4.2 Luttinger liquid description for our system

In this section, we describe the resulting effective low-energy Luttinger liquid theory of an interacting single-channel Rashba wire. Employing Abelian bosonisation, introduced in the last section, see also [47], we introduce a boson field and its conjugate momentum for each band $\nu = A, B = +, -$. It is useful to switch to symmetric (charge) fields, $\Phi_c(x)$ and $\Pi_c(x) = -\partial_x \Theta_c(x)$, antisymmetric (spin for $\alpha = 0$) fields, $\Phi_s(x)$ and $\Pi_s(x) = -\partial_x \Theta_s$, and linear combinations of these fields and their momenta. The dual fields Φ and Θ then allow to express the electron operator from equation (2.21) and the bosonisation dictionary,

$$\begin{aligned} \Psi(x,z) &= \sum_{\nu,r} \phi_{rk_F^{(\nu)},\nu r}(z) \frac{\eta_{\nu r}}{\sqrt{2\pi a}} \\ &\times \; e^{irk_F^{(\nu)}x + i\sqrt{\pi/2}[r\Phi_c + \Theta_c + \nu r \Phi_s + \nu \Theta_s]}, \end{aligned} \qquad (2.59)$$

where a is a small cutoff length and $\eta_{\nu r}$ are the standard Klein factors, see above and [47, 62, 63]. We adopt the convention $\eta_{\nu R}\eta_{\nu L}\eta_{-\nu,R}\eta_{-\nu,L} = 1$. To recover the conventional expression for $\alpha = 0$, due to our convention for the band indices in the left-moving sector, one should replace $\Phi_s, \Theta_s \to -\Theta_s, -\Phi_s$. Using the identity (2.34), we can now express the one-dimensional charge and spin densities,

$$\rho(x) = \int dz\, \Psi^\dagger \Psi, \quad \boldsymbol{S}(x) = \int dz\, \Psi^\dagger \frac{\boldsymbol{\sigma}}{2} \Psi, \tag{2.60}$$

in bosonised form. The one-dimensional charge and spin densities (2.60) can be written as the sum of slow and fast (oscillatory) contributions. Slow contributions have a spatial oscillation frequency of $k_A - k_B$ or slower, and fast oscillatory modes have frequencies $2k_A$, $2k_B$, or $k_A + k_B$. Using equation (2.34), the bosonised form for the one-dimensional charge density is

$$\begin{aligned}\rho(x) \quad &= \quad \sqrt{\frac{2}{\pi}}\, \partial_x \Phi_c - \frac{2i}{\pi a} \eta_{AR}\eta_{AL} \cos(\theta_A - \theta_B) \\ &\quad\quad \times \sin\left[\left(k_F^{(A)} + k_F^{(B)}\right) x + \sqrt{2\pi}\Phi_c\right] \cos(\sqrt{2\pi}\Theta_s). \end{aligned} \tag{2.61}$$

Similarly, using the identity

$$\begin{aligned} &\int dz \left[\phi^\dagger_{rk_F^{(\nu)},\nu r}\, \boldsymbol{\sigma}\, \phi_{r'k_F^{(\nu')},\nu' r'}\right](z) = \\ &\delta_{r,r'} \begin{pmatrix} \cos\left(\theta_A - \theta_B\right) \delta_{\nu,-\nu'} \\ -i\nu r\, \cos\left(\theta_A + \theta_B\right) \delta_{\nu,-\nu'} \\ \nu r\, \cos\left(2\,\theta_\nu\right) \delta_{\nu,\nu'} \end{pmatrix} + \delta_{r,-r'} \begin{pmatrix} \delta_{\nu,\nu'} \\ -i\nu r\, \cos\left(2\,\theta_\nu\right) \delta_{\nu,\nu'} \\ \nu r\, \cos\left(\theta_A + \theta_B\right) \delta_{\nu,-\nu'} \end{pmatrix}, \end{aligned} \tag{2.62}$$

the one-dimensional spin density vector has the components

$$\begin{aligned} S^x(x) \quad &= \quad -i\frac{\eta_{AR}\eta_{BR}}{\pi a} \cos\left(\theta_A - \theta_B\right) \cos\left[\left(k_F^{(A)} - k_F^{(B)}\right) x + \sqrt{2\pi}\Phi_s\right] \sin(\sqrt{2\pi}\Theta_s) \\ &\quad\quad -i\frac{\eta_{AR}\eta_{AL}}{\pi a} \cos\left[\left(k_F^{(A)} + k_F^{(B)}\right) x + \sqrt{2\pi}\Phi_c\right] \sin\left[\left(k_F^{(A)} - k_F^{(B)}\right) x + \sqrt{2\pi}\Phi_s\right], \end{aligned} \tag{2.63}$$

$$\begin{aligned} S^y(x) \quad &= \quad i\frac{\eta_{AR}\eta_{BR}}{\pi a} \cos\left(\theta_A + \theta_B\right) \sin\left[\left(k_F^{(A)} - k_F^{(B)}\right) x + \sqrt{2\pi}\Phi_s\right] \sin(\sqrt{2\pi}\Theta_s) \\ &\quad\quad -i \sum_{\nu=A,B=+,-} \nu \frac{\eta_{\nu R}\eta_{\nu L}}{2\pi a} \cos(2\theta_\nu) \cos\left[2k_F^{(\nu)} x + \sqrt{2\pi}\left(\Phi_c + \nu\Phi_s\right)\right], \end{aligned} \tag{2.64}$$

$$\begin{aligned} S^z(x) &= \frac{1}{\sqrt{8\pi}}\left[(\cos 2\theta_A + \cos 2\theta_B)\,\partial_x\Theta_s + (\cos 2\theta_A - \cos 2\theta_B)\,\partial_x\Theta_c\right] \\ &- i\frac{\eta_{AR}\eta_{BL}}{\pi a}\cos(\theta_A+\theta_B)\cos\left[\left(k_F^{(A)}+k_F^{(B)}\right)x + \sqrt{2\pi}\Phi_c\right]\sin(\sqrt{2\pi}\Phi_s). \end{aligned} \tag{2.65}$$

Note that while $\partial_x\Phi_c$ is proportional to the (slow part of the) charge density, the (slow) spin density is determined by both c and s sectors.

The low-energy Hamiltonian is then taken with the fixed-point values for the interaction constants, i.e., backscattering processes are disregarded and only appear via the renormalised value of $\bar{g}_2^*$ in equation (2.49). Following standard steps summarised in the last section, the kinetic term H_0 and the forward scattering processes then lead to the exactly solvable Gaussian field theory of a modified (extended) Luttinger liquid,

$$\begin{aligned} H &= \sum_{j=c,s}\frac{v_j}{2}\int dx\,\left(K_j\Pi_j^2 + \frac{1}{K_j}(\partial_x\Phi_j)^2\right) \\ &+ v_\lambda\int dx\,\left(K_\lambda\Pi_c\Pi_s + \frac{1}{K_\lambda}(\partial_x\Phi_c)(\partial_x\Phi_s)\right). \end{aligned} \tag{2.66}$$

Using the notations $\bar{g}_4 = W_0/\pi v_F$ and

$$y_\delta = \frac{g^*_{2\|A} - g^*_{2\|B}}{4\pi v_F}, \tag{2.67}$$

$$y_\pm = \frac{g^*_{2\|A} + g^*_{2\|B} \pm 2g^*_{2\perp}}{4\pi v_F}, \tag{2.68}$$

where explicit (but lengthy) expressions for the fixed-point values $g^*_{2\|A/B}$ and $g^*_{2\perp}$ can be straightforwardly obtained from equations (2.45) and (2.49), using the integrals of motion equations (A.26) to (A.28), the renormalised velocities appearing in equation (2.66) are

$$\begin{aligned} v_c &= v_F\sqrt{(1+\bar{g}_4)^2 - y_+^2} \\ &\simeq v_F\sqrt{\left(1+\frac{W_0}{\pi v_F}\right)^2 - \left(\frac{2W_0 - W_1}{2\pi v_F}\right)^2}, \\ v_s &= v_F\sqrt{1-y_-^2} \simeq v_F, \\ v_\lambda &= v_F\sqrt{\delta^2 - y_\delta^2} \simeq v_F\delta\sqrt{1-\left(\frac{W_1}{4\pi v_F}\right)^2}. \end{aligned} \tag{2.69}$$

In the respective second equalities, we have specified the leading terms in $|\delta| \ll 1$, since the spin-orbit coupling-induced relative velocity asymmetry δ is small even for rather large α, see equation (2.19). The corrections to the quoted expressions are of $\mathcal{O}(\delta^2)$ and are negligible in practice. It is noteworthy that the spin velocity v_s is not renormalised for a Rashba wire, although it is well-known that v_s will be renormalised due to W_1 for $\alpha = 0$ [47]. This difference can be traced to our thin-wire approximation (2.33). When releasing this approximation, there will be a renormalisation in general. Finally, the dimensionless Luttinger liquid interaction parameters in equation (2.66) are given by

$$\begin{aligned} K_c &= \sqrt{\frac{1+\bar{g}_4-y_+}{1+\bar{g}_4+y_+}} \simeq \sqrt{\frac{2\pi v_F+W_1}{2\pi v_F+4W_0-W_1}}, \\ K_s &= \sqrt{\frac{1-y_-}{1+y_-}} \simeq 1-\frac{\sqrt{W_0W_1}}{\sqrt{2}\,\pi v_F}|\delta|, \\ K_\lambda &= \sqrt{\frac{\delta-y_\delta}{\delta+y_\delta}} \simeq \sqrt{\frac{4\pi v_F+W_1}{4\pi v_F-W_1}}, \end{aligned} \tag{2.70}$$

where the second equalities again hold up to contributions of $\mathcal{O}(\delta^2)$. When the $2k_F$ component of the interaction potential $W_1 = 0$, see equation (2.35), we obtain $K_s = K_\lambda = 1$, and thus recover the theory of reference [44]. The broken spin $SU(2)$ symmetry is reflected in $K_s < 1$ when both $\delta \neq 0$ and $W_1 \neq 0$.

Since we arrived at a Gaussian field theory, equation (2.66), all low-energy correlation functions can now be computed analytically without further approximation.

2.5 RKKY interaction

In this section we apply the low energy theory of the interacting quantum wire with spin-orbit coupling, derived above, to compute the RKKY range function. The RKKY theory [54–56] describes the interaction between two localised spins that is mediated via the conduction band electrons. For better understanding we will first summarise the theory and compute the range function for a noninteraction one-dimensional system without spin-orbit coupling following [57, 58].

A single localised spinful impurity $\mathbf{\Sigma}_n$, with spatial components Σ_n^a, interacting with the electron gas is described by

$$H_S = J\sum_i \boldsymbol{\sigma}_i \cdot \mathbf{\Sigma}_n \delta(x_i - x_n), \tag{2.71}$$

where $\boldsymbol{\sigma}_i$ are vectors of Pauli matrices describing the spins of the ith electron. In lowest order we find the interaction between the two impurities to be

$$H_{RKKY} = -J^2 \sum_{ab} \Sigma_1^a \Sigma_2^b F^{ab}(x), \tag{2.72}$$

where the rangefunction matrix $F^{ab}(x)$ is diagonal for an $SU(2)$ invariant system i.e.,

$F^{ab}(x) = F(x)\delta_{ab}$.

2.5.1 One-dimensional free electron gas

We now derive the range function for a free one-dimensional electron gas. We start by finding the spin susceptibility χ_q which is defined via the magnetisation $\mathbf{M}$ in the following way

$$\mathbf{M}(x) = \frac{1}{V}\int dx'\chi(x-x')\mathbf{H}(x'), \tag{2.73}$$

where V is the volume, $\mathbf{H}(\mathbf{x})$ is the magnetic field, and $\chi(x-x') = \sum_q \chi_q \exp[iq(x-x')]$. The one-dimensional kinetic Hamiltonian for N electrons reads

$$H_0 = \sum_{i=1}^{N} \frac{p_i}{2m}. \tag{2.74}$$

To compute χ_q we include the effect of a magnetic field

$$H_M = \mu_B \sum_{i=1}^{N} \boldsymbol{\sigma}_i \cdot \mathbf{h}_q \cos qx, \tag{2.75}$$

to the Hamiltonian as a perturbation, where μ_B is the Bohr magneton and $\mathbf{h}_q$ is the Fourier transformation of $\mathbf{H}(x)$, we set $\mathbf{h}_q = \hat{x}h_q$. The unperturbed states are the momentum and spin eigenstates $|k\uparrow\rangle$ and $|k\downarrow\rangle$. In first order perturbation H_M does not contribute. The first non-zero perturbation is in second order. The energy correction for momentum k reads

$$\epsilon_k^{(2)} = \frac{1}{4}(\mu_B h_q)^2\left[\frac{(1-n_{k+q})n_k}{\epsilon_k-\epsilon_{k+q}} + \frac{(1-n_{k-q})n_k}{\epsilon_k-\epsilon_{k-q}}\right], \tag{2.76}$$

where only unoccupied states are allowed as intermediate states. The total energy correction is now easily obtained by summing over all occupied states, given as

$$\begin{aligned} E^{(2)} &= \frac{1}{4}(\mu_B h_q)^2\sum_k\left[\frac{(1-n_{k+q})n_k}{\epsilon_k-\epsilon_{k+q}} + \frac{(1-n_{k-q})n_k}{\epsilon_k-\epsilon_{k-q}}\right] & (2.77)\\ &= -\frac{1}{4}(\mu_B h_q)^2 F(q), & (2.78)\end{aligned}$$

hereby defining the function $F(q)$. The spin susceptibility is then given by

$$\chi_q = -2\frac{\partial^2 E^{(2)}}{\partial h_q^2} = \mu_B F(q). \tag{2.79}$$

In a free one-dimensional electron gas with $\epsilon_k = \frac{\hbar^2 k^2}{2m}$ one finds

$$\begin{aligned} F(q) &= \frac{2m}{\hbar^2 \pi} \int_{-k_F}^{k_F} dk \left(\frac{1}{q+2k} + \frac{1}{q+2k} \right) && (2.80) \\ &= \frac{2m}{\hbar^2 \pi q} \log \left| \frac{2k_F + q}{2k_F - q} \right| , && (2.81) \end{aligned}$$

where the k-sum is changed into an integral over the occupied states between the Fermi points $\pm k_F$. The range function $F(x)$ is defined via

$$\begin{aligned} F(x) &= \frac{\mu_B^2}{2\pi} \int_{-\infty}^{\infty} dq \exp[iqx] F(q) && (2.82) \\ &= \frac{\mu_B^2 m}{2\pi^2 \hbar^2} \int_{-k_F}^{k_F} \frac{dk}{k} \int_{-\infty}^{\infty} dq \exp[iqx] \left(\frac{1}{q-2k} - \frac{1}{q+2k} \right) . && (2.83) \end{aligned}$$

Using the Cauchy method of residues one finds

$$F(x) = -\frac{\mu_B^2 m}{2\pi \hbar^2} \int_{-k_F}^{k_F} dk \frac{\sin 2kx}{k} = \frac{2\mu_B^2 m}{\pi \hbar^2} \left(\frac{\pi}{2} - \mathrm{Si}(2k_F x) \right) , \qquad (2.84)$$

where Si is the sine integral function, which in the long distance (i.e., low energy) limit can be simplified to

$$F(x) \approx \frac{2\mu_B^2 m}{\pi \hbar^2} \frac{\cos 2k_F x}{x} . \qquad (2.85)$$

Here we can see that the range function will decay as x^{-1} and oscillate with a period of $2k_F$. In the following we show that including spin-orbit coupling and e-e interaction will cause different periods of oscillation in different directions and power laws instead of a simple x^{-1} decay.

2.5.2 RKKY Interaction in our system

Following our discussion in section 2.1, we now investigate the combined effects of the Rashba spin-orbit coupling and the e-e interaction on the RKKY range function. We include the exchange coupling, $H' = J \sum_{i=1,2} \mathbf{\Sigma}_i \cdot \boldsymbol{S}(x_i)$, of the one-dimensional conduction electron spin density $\boldsymbol{S}(x)$ to localised spin-1/2 magnetic impurities, separated by $x = x_1 - x_2$. The RKKY interaction H_{RKKY}, describing spin-spin interactions between the two magnetic impurities, is then obtained by perturbation theory in J [57, 58]. In the simplest one-dimensional case (no spin-orbit coupling, no interactions), it is given by equation (2.85). In the general case, it can always be expressed in the form

$$H_{\mathrm{RKKY}} = -J^2 \sum_{a,b} F^{ab}(x) \Sigma_1^a \Sigma_2^b, \tag{2.86}$$

with the range function now appearing as a tensor ($\beta = 1/k_B T$ for temperature T),

$$F^{ab}(x) = \int_0^\beta d\tau \; \chi^{ab}(x, \tau). \tag{2.87}$$

Here, the imaginary-time (τ) spin-spin correlation function

$$\chi^{ab}(x, \tau) = \langle S^a(x, \tau) S^b(0, 0) \rangle \tag{2.88}$$

appears. The one-dimensional spin densities $S^a(x)$ (with $a = x, y, z$) were defined in equation (2.60), and their bosonised expression is given in equation (2.63) to (2.65), which then allows computing the correlation functions (2.88) using the unperturbed ($J = 0$) Luttinger liquid model (2.66). The range function thus effectively coincides with the static space-dependent spin susceptibility tensor. When spin $SU(2)$ symmetry is realized, $\chi^{ab}(x) = \delta^{ab} F_{\mathrm{ex}}(x)$, and equation (2.85) is recovered, but in general this tensor is not diagonal. For a Luttinger liquid without Rashba spin-orbit coupling, $F_{\mathrm{ex}}(x)$ is as in equation (2.85) but with a slow power-law decay [62, 63].

If spin $SU(2)$ symmetry is broken, general arguments imply that equation (2.86) can be decomposed into three terms, namely, (i) an isotropic exchange scalar coupling, (ii) a Dzyaloshinsky-Moriya (DM) vector term, and (iii) an Ising-like interaction,

$$H_{\mathrm{RKKY}}/J^2 = -F_{\mathrm{ex}}(x) \boldsymbol{\Sigma}_1 \cdot \boldsymbol{\Sigma}_2 - \boldsymbol{F}_{\mathrm{DM}}(x) \cdot (\boldsymbol{\Sigma}_1 \times \boldsymbol{\Sigma}_2) - \sum_{a,b} F^{ab}_{\mathrm{Ising}}(x) \Sigma_1^a \Sigma_2^b, \tag{2.89}$$

where $F_{\mathrm{ex}}(x) = \frac{1}{3} \sum_a F^{aa}(x)$. The DM vector has the components

$$F^c_{\mathrm{DM}}(x) = \frac{1}{2} \sum_{a,b} \epsilon^{cab} F^{ab}(x),$$

and the Ising-like tensor

$$F^{ab}_{\mathrm{Ising}}(x) = \frac{1}{2} \left(F^{ab} + F^{ba} - \frac{2}{3} \sum_c F^{cc} \delta^{ab} \right)(x)$$

is symmetric and traceless.

For a one-dimensional noninteracting quantum wire with Rashba spin-orbit coupling, the RKKY Hamiltonian (2.89) has recently been discussed [59–61], and all range functions appearing in equation (2.89) were shown to decay $\propto |x|^{-1}$, as expected for a noninteracting system. Moreover, it has been emphasised [60] that there are different spatial oscillation periods, reflecting the presence of different Fermi momenta $k_F^{(A,B)}$ in a Rashba quantum wire.

Let us then consider the extended Luttinger liquid model (2.66), which includes the effects of both the e-e interaction and the Rashba spin-orbit coupling. The correlation functions (2.88) obey $\chi^{ba}(x,\tau) = \chi^{ab}(-x,-\tau)$, and since we find $\chi^{xz} = \chi^{yz} = 0$, the anisotropy acts only in the xy-plane. The four nonzero correlators are specified below, where only the long-ranged $2k_F$ oscillatory terms are kept, the terms we defined as fast oscillatory terms. These are the relevant correlations determining the RKKY interaction in the interacting quantum wire. We note that in the noninteracting case, there is also a slow oscillatory component, corresponding to a contribution to the RKKY range function $\propto \cos\left[\left(k_F^{(A)} - k_F^{(B)}\right)x\right]/|x|$. Remarkably, we find that this $1/x$ decay law is not changed by interactions. However, we will show below that interactions cause a slower decay of certain fast oscillatory terms, e.g., the contribution $\propto \cos(2k_F^{(B)}x)$. We therefore do not further discuss the slow oscillatory terms in what follows.

Next we compute the nonzero components of the imaginary-time spin-spin correlation function $\chi^{ab}(x,\tau)$, see equation (2.88). Using the above bosonised expressions, (2.63) to (2.65), some algebra yields

$$\chi^{xx}(x,\tau) = \sum_{\nu} \frac{\cos\left(2k_F^{(\nu)}x\right)}{2(2\pi a)^2} \tilde{F}_\nu^{(1)}(x,\tau), \tag{2.90}$$

$$\chi^{yy}(x,\tau) = \sum_{\nu} \frac{\cos^2(2\theta_\nu)\cos\left(2k_F^{(\nu)}x\right)}{2(2\pi a)^2} \tilde{F}_\nu^{(1)}(x,\tau), \tag{2.91}$$

$$\chi^{zz}(x,\tau) = \sum_{\nu r} \frac{\cos^2(\theta_A + \theta_B)}{2(2\pi a)^2} \tag{2.92}$$

$$\times \cos\left[\left(k_F^{(A)} + k_F^{(B)}\right)x\right] \tilde{F}_\nu^{(2)}(x,\tau), \tag{2.93}$$

and

$$\chi^{xy}(x,\tau) = \sum_{\nu} \frac{\nu\cos(2\theta_\nu)\sin\left(2k_F^{(\nu)}x\right)}{2(2\pi a)^2} \tilde{F}_\nu^{(1)}(x,\tau). \tag{2.94}$$

Here, the functions $\tilde{F}^{(1,2)}_{\nu=A,B=+,-}(x,\tau)$ are given by

$$\tilde{F}_\nu^{(1)}(x,\tau) = \prod_{j=1,2} \left| \frac{\beta u_j}{\pi a} \sin\left(\frac{\pi(u_j\tau - ix)}{\beta u_j}\right) \right|^{-\left(\Gamma^{(j)}_{\Phi_c\Phi_c} + \Gamma^{(j)}_{\Phi_s\Phi_s} + 2\nu\Gamma^{(j)}_{\Phi_c\Phi_s}\right)} \tag{2.95}$$

and

$$\tilde{F}_\nu^{(2)}(x,\tau)=\prod_{j=1,2}\left|\frac{\beta u_j}{\pi a}\sin\left(\frac{\pi(u_j\tau-ix)}{\beta u_j}\right)\right|^{-\left(\Gamma^{(j)}_{\Phi_c\Phi_c}+\Gamma^{(j)}_{\Theta_s\Theta_s}\right)}\left[\frac{\sin\left(\frac{\pi(u_j\tau+ix)}{\beta u_j}\right)}{\sin\left(\frac{\pi(u_j\tau-ix)}{\beta u_j}\right)}\right]^{\nu\Gamma^{(j)}_{\Phi_c\Theta_s}}. \tag{2.96}$$

The dimensionless numbers $\Gamma^{(j)}$ appearing in the exponents follow from the straightforward (but lengthy) diagonalisation of the extended Luttinger liquid Hamiltonian (2.66), where the u_j are the velocities of the corresponding normal modes. With the velocities $v_{c,s}$ (2.69) and the dimensionless Luttinger parameters (2.70), the result of this linear algebra problem can be written as follows. The normal-mode velocities u_1 and u_2 are

$$\begin{aligned}2u^2_{j=1,2} &= v_c^2+v_s^2+2v_\lambda^2 \qquad (2.97)\\ &\quad -(-1)^j\sqrt{(v_c^2-v_s^2)^2+4v_\lambda^2\left[v_cv_s\left(\frac{K_\lambda^2}{K_cK_s}+\frac{K_cK_s}{K_\lambda^2}\right)+v_c^2+v_s^2\right]},\end{aligned}$$

and the exponents $\Gamma^{(j=1,2)}$ appearing in $\tilde{F}_\nu^{(1,2)}(x,\tau)$ are given by

$$\Gamma^{(j)}_{\Phi_c\Phi_c}=\frac{(-1)^jK_cv_c}{u_j(u_1^2-u_2^2)}\left(v_s^2-u_j^2-\frac{K_\lambda^2v_\lambda^2v_s}{K_cK_sv_c}\right), \tag{2.98}$$

$$\Gamma^{(j)}_{\Phi_s\Phi_s}=\frac{(-1)^jK_sv_s}{u_j(u_1^2-u_2^2)}\left(v_c^2-u_j^2-\frac{K_\lambda^2v_\lambda^2v_c}{K_cK_sv_s}\right), \tag{2.99}$$

$$\Gamma^{(j)}_{\Phi_c\Phi_s}=\frac{(-1)^jK_\lambda v_\lambda}{u_j(u_1^2-u_2^2)}\left(v_\lambda^2-u_j^2-\frac{K_cK_sv_sv_c}{K_\lambda^2}\right), \tag{2.100}$$

$$\Gamma^{(j)}_{\Theta_s\Theta_s}=\frac{(-1)^jv_s}{K_su_j(u_1^2-u_2^2)}\left(v_c^2-u_j^2-\frac{K_cK_sv_\lambda^2v_c}{K_\lambda^2v_s}\right), \tag{2.101}$$

$$\Gamma^{(j)}_{\Phi_c\Theta_s}=\frac{(-1)^jv_\lambda}{u_1^2-u_2^2}\left(\frac{K_\lambda}{K_s}v_s+\frac{K_c}{K_\lambda}v_c\right). \tag{2.102}$$

Since $|\delta|\ll 1$, we now employ the simplified expressions for the velocities in equation (2.69) and the Luttinger liquid parameters in equation (2.70), which are valid up to $\mathcal{O}(\delta^2)$ corrections. In the interacting case, this yields for the normal-mode velocities simply $u_1=v_c$ and $u_2=v_s$. In the noninteracting limit, the above equation instead yields $u_1=v_A$ and $u_2=v_B$, see equation (2.19). Furthermore, the exponents $\Gamma^{(j)}$ simplify to

$$\Gamma^{(1)}_{\Phi_c\Phi_c}=K_c,\quad \Gamma^{(2)}_{\Phi_c\Phi_c}=\Gamma^{(1)}_{\Phi_s\Phi_s}=\Gamma^{(1)}_{\Theta_s\Theta_s}=0, \tag{2.103}$$

$$\Gamma^{(2)}_{\Phi_s\Phi_s}=K_s,\quad \Gamma^{(2)}_{\Theta_s\Theta_s}=1/K_s, \tag{2.104}$$

$$\Gamma^{(1)}_{\Phi_c\Phi_s}=\frac{v_\lambda}{v_c^2-v_s^2}(K_\lambda v_c+K_cv_s/K_\lambda), \tag{2.105}$$

$$\Gamma^{(2)}_{\Phi_c\Phi_s} = -\frac{v_\lambda}{v_c^2 - v_s^2}(K_\lambda v_s + K_c v_c/K_\lambda), \tag{2.106}$$

$$\Gamma^{(1,2)}_{\Phi_c\Theta_s} = \pm\Gamma^{(2)}_{\Phi_c\Phi_s}. \tag{2.107}$$

Collecting everything and taking the zero-temperature limit, the functions $\tilde{F}^{(1,2)}_{\nu=\pm}(x,\tau)$ take the form

$$\tilde{F}^{(1)}_\nu(x,\tau) = \left|\frac{v_c\tau - ix}{a}\right|^{-K_c - 2\nu v_\lambda \frac{K_\lambda v_c + K_c v_s/K_\lambda}{v_c^2 - v_s^2}} \left|\frac{v_s\tau - ix}{a}\right|^{-K_s + 2\nu v_\lambda \frac{K_\lambda v_s + K_c v_c/K_\lambda}{v_c^2 - v_s^2}}, \tag{2.108}$$

and

$$\tilde{F}^{(2)}_\nu(x,\tau) = \left|\frac{v_c\tau - ix}{a}\right|^{-K_c} \left|\frac{v_s\tau - ix}{a}\right|^{-1/K_s} \left(\frac{(v_s\tau - ix)(v_c\tau + ix)}{(v_s\tau + ix)(v_c\tau - ix)}\right)^{-\nu\frac{v_\lambda(K_\lambda v_s + K_c v_c/K_\lambda)}{v_c^2 - v_s^2}}. \tag{2.109}$$

The known form of the spin-spin correlations in a Luttinger liquid with $\alpha = 0$ is recovered by putting $v_\lambda \propto \delta = 0$.

With this, we find the various range functions in equation (2.89) for the interacting case,

$$\begin{aligned}
F_{\text{ex}}(x) &= \frac{1}{6}\sum_\nu \Big[\big(1 + \cos^2(2\theta_\nu)\big)\cos\left(2k_F^{(\nu)}x\right)F^{(1)}_\nu(x) \\
&\quad + \cos^2(\theta_A + \theta_B)\cos\left[(k_F^{(A)} + k_F^{(B)})x\right]F^{(2)}_\nu(x)\Big], \\
\boldsymbol{F}_{\text{DM}}(x) &= \hat{e}_z\sum_\nu \frac{\nu}{2}\cos(2\theta_\nu)\sin\left(2k_F^{(\nu)}x\right)F^{(1)}_\nu(x), \\
F^{ab}_{\text{Ising}}(x) &= \left[\frac{1}{2}\sum_\nu G^a_\nu(x) - F_{ex}(x)\right]\delta^{ab},
\end{aligned} \tag{2.110}$$

with the auxiliary vector

$$\boldsymbol{G}_\nu = \begin{pmatrix} \cos\left(2k_F^{(\nu)}x\right)F^{(1)}_\nu(x) \\ \cos^2(2\theta_\nu)\cos\left(2k_F^{(\nu)}x\right)F^{(1)}_\nu(x) \\ \cos^2(\theta_A + \theta_B)\cos\left[(k_F^{(A)} + k_F^{(B)})x\right]F^{(2)}_\nu(x) \end{pmatrix}.$$

The functions $F^{(1,2)}_\nu(x)$ follow by integration over τ from $\tilde{F}^{(1,2)}_\nu(x,\tau)$, see equations (2.108) and (2.109) above. This implies the respective decay laws for $a \ll |x| \ll v_F/k_BT$,

$$\begin{aligned}
F^{(1)}_\nu(x) &\propto |a/x|^{-1+K_c+K_s+2\nu(1-K_c/K_\lambda^2)\frac{v_\lambda K_\lambda}{v_c+v_s}}, \\
F^{(2)}_\nu(x) &\propto |a/x|^{-1+K_c+1/K_s}.
\end{aligned} \tag{2.111}$$

All these exponents approach unity in the noninteracting limit, in accordance with previous results [59, 60]. Moreover, in the absence of spin-orbit coupling ($\alpha = \delta = 0$), equation (2.111) reproduces the known $|x|^{-K_c}$ decay law for the RKKY interaction in a conventional Luttinger liquid [62, 63].

Since $K_s < 1$ for an interacting Rashba wire with $\delta \neq 0$, see equation (2.70), we conclude that $F_\nu^{(1)}$ with $\nu = B$, corresponding to the slower velocity $v_B = v_F(1-\delta)$, leads to the slowest decay of the RKKY interaction. For large distance x, the RKKY interaction is therefore dominated by the $2k_F^{(B)}$ oscillatory part, and all range functions decay $\propto |x|^{-\eta_B}$ with the exponent

$$\eta_B = K_c + K_s - 1 - 2\left(1 - \frac{K_c}{K_\lambda^2}\right)\frac{v_\lambda K_\lambda}{v_c + v_s} < 1. \tag{2.112}$$

This exponent depends on both the e-e interaction potential, and on the Rashba coupling α. The latter dependence also implies that electric fields are able to change the power-law decay of the RKKY interaction in a Rashba wire. The DM vector coupling also illustrates that the spin-orbit coupling is able to effectively induce off-diagonal couplings in spin space, reminiscent of spin precession effects. Also these RKKY couplings are $2k_F^{(B)}$ oscillatory and show a power-law decay with the exponent (2.112).

2.6 Discussion

In this chapter, we have presented a careful derivation of the low-energy Hamiltonian of a homogeneous one-dimensional quantum wire, with Rashba spin-orbit interactions. We have studied the simplest case (no magnetic field, no disorder, and single-channel limit), in particular analysing the possibility for a spin gap to occur due to electron-electron backscattering processes. The initial values for the coupling constants entering the one-loop RG equations were determined for rather general conditions. These are such that backscattering is marginally irrelevant and no spin gap opens. The resulting low-energy theory is a modified Luttinger liquid, equation (2.66), which is a Gaussian field theory formulated in terms of the boson fields $\Phi_c(x)$ and $\Phi_s(x)$, and their dual fields. In this state, spin-charge separation is violated due to the Rashba coupling. Two collective modes are still found, but now they are mixes of spin and charge fields. The theory allows exact results for essentially all low-energy correlation functions.

Based on our bosonised expressions for the one-dimensional charge and spin density, the frequency dependence of various susceptibilities of interest, e.g., charge- or spin-density wave correlations, can then be computed. As the calculation closely mirrors the one in [49, 50], we do not repeat it here. A *phase diagram* from the study of the dominant susceptibilities can then be inferred. According to our calculations, due to a conspiracy of the Rashba spin-orbit coupling and the e-e interaction, spin-density-wave correlations in the xy plane are always dominant for repulsive interactions.

We have studied the RKKY interaction between two magnetic impurities in such an interacting one-dimensional Rashba quantum wire. On general grounds, the RKKY interaction can be decomposed into an exchange term, a DM vector term, and a traceless symmetric tensor interaction. For a noninteracting wire, the corresponding three range functions have several spatial oscillation periods with a common overall decay $\propto |x|^{-1}$. We have shown that interactions modify this picture. The dominant contribution (characterised by the slowest power-law decay) to the RKKY range function is now $2k_F^{(B)}$ oscillatory for all three terms, with the same exponent $\eta_B < 1$, see equation (2.112). This exponent depends both on the interaction strength and on the Rashba coupling. This raises the intriguing possibility to tune the power-law exponent η_B governing the RKKY interaction by an electric field, since α is tunable via a back-gate voltage. We stress again that interactions imply that a single spatial oscillation period (wavelength $\pi/k_F^{(B)}$) becomes dominant, in contrast to the noninteracting situation where several competing wavelengths are expected.

The above formulation also holds promise for future calculations of spin transport in the presence of both interactions and Rashba spin-orbit couplings, and possibly with disorder. Under a perturbative treatment of impurity backscattering, otherwise exact statements are possible even out of equilibrium.

Chapter 3

Spin-dependent transport in conducting polymers

3.1 Introduction

In this chapter we consider a different class of materials that have attracted a lot of interest in recent years, conducting organic polymers. Unlike most polymers, i.e., plastics we know as insulators in everyday life, these polymers are semiconductors with unconventional transport properties [22]. Since their discovery, interesting new fundamental insights have been gained, as well as the prospect of new applications and devices functioning at room temperature [67,68]. A particularly interesting aspect comes from the spin degree of freedom, leading to plastic spintronics [69]. Organic materials such as polymers may be superior to inorganic semiconductor devices because of their small spin-orbit and hyperfine couplings, in principle allowing for very long spin coherence times. The ground state of conducting polymers displays a gapped bandstructure as usual for semiconductors. However, the conduction mechanism in polymers is fundamentally different to that of conventional semiconductors where electrons in the conduction band, or holes in the valence band transport the current. In polymers the coupling between lattice vibrations (phonons) and the electronic states plays a vital role for the understanding of the excitations and the transport physics. The excitations are combined states of lattice deformations and electronic states, such as polarons, bipolarons, and in fewer cases solitons. Polarons and bipolarons exist in all conjugated polymers whereas for the formation of solitons an additional symmetry in the lattice structure is needed. All these excitations are spatially localised states that energetically lie deep inside the gap. In addition to the mix between phonons and electrons some of these excitations also have a non-standard spin-charge relation. Whereas, polarons have a simple electronic spin-charge relation (singly charged with spin-1/2), bipolarons (the bound state of two polarons) are doubly charged and spinless. Solitons are most peculiar and occur as singly charged spinful quasiparticles or as spinful but chargeless particles [23]. This raises the possibility of unconventional spin-transport properties. Spin transport through conjugated semiconducting organic polymers has consequently been studied in a number of recent experiments. Clear evidence for spin-polarised current injection and giant magnetoresistance in organic spin valves [70–73] has been reported, as well as spin-dependent optical effects [74, 75]. For most polymers, it has been established that the dominant charge and spin carriers, at low energy scales well below the gap, correspond to polarons and bipolarons [23, 67, 76], whereas solitons can safely be ignored.

In the following, we discuss spin transport through slightly doped, semiconducting organic polymers, where polarons and bipolarons are the relevant charge carriers. In a typical two-terminal geometry (transport along the x axis), the organic polymer is contacted at $x = 0$ and $x = L$ by two ferromagnetic metallic electrodes, where L is the length of the polymer. The left (right) electrode is characterised by a magnetisation unit vector $\hat{m}_L$ ($\hat{m}_R$), with the angle θ between them. We do not attempt a microscopic modelling of the interface between a ferromagnetic electrode and the organic polymer, but follow the arguments of Refs. [76–79], where it has been established that carriers injected into the polymer tunnel predominantly into polaron states close to the ferromagnetic contact. We therefore impose the boundary condition that no bipolaron states near the boundaries (at $x = 0$ and $x = L$) are filled by the injected current. Both contacts can then be completely described by spin-dependent conductances $G^{\uparrow}$ and $G^{\downarrow}$, which take into account the spin-dependent density of states in the ferromagnets and the disorder-averaged matrix elements for tunnelling into polaron states [80]. Moreover, for noncollinear magnetisations, one also has to include the complex-valued mixing conductance $G^{\uparrow\downarrow}$ reflecting boundary exchange processes [81–83].

Transport in the polymer itself has so far been modelled either numerically, using lattice simulations of charge transport [84–87], or analytically, using simple master equations [88] or drift-diffusion models. The latter approaches have also been applied to spin transport [89–92]. Here we use the network theory of Ref. [80, 81] combined with a diffusive model to obtain spin dependent transport properties of a doped organic polymer sandwiched between two ferromagnetic electrodes with noncollinear magnetisation directions. In the absence of bipolarons and for very high temperatures, this problem has been studied in Ref. [91]. Here we present a generalisation including the polaron-bipolaron conversion process.

This chapter is organised as follows. In Sec. 3.2 we summarise the theory of conjugated polymers following [23, 93], discussing the ground state and the excitations, i.e., solitons, polarons and bipolarons. In Sec. 3.3 we set up a model, which describes the diffusive transport trough the polymer, allowing two polarons to recombine into a bipolaron and

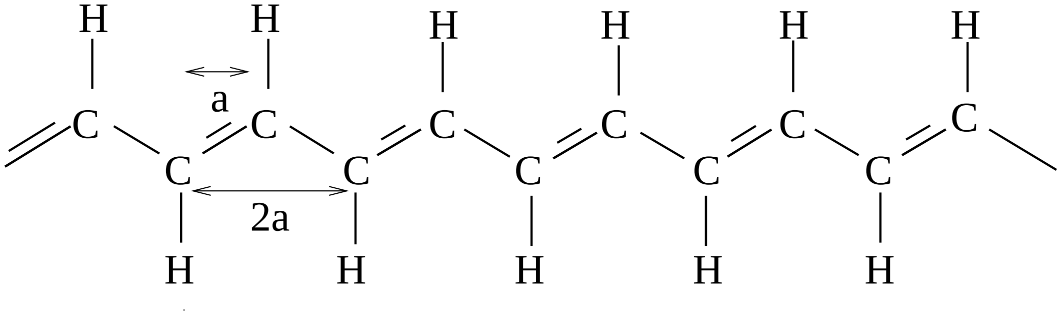

Figure 3.1: The structural diagram for *trans*-polyacetylene displays the typical dimerisation pattern. In *trans*-polyacetylene an additional symmetry is found, since the double and the single bonds can be interchanged without changing the energy of the system.

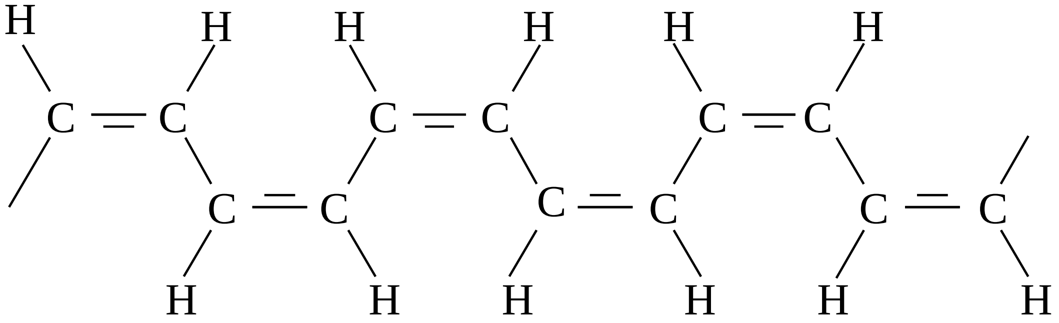

Figure 3.2: Structural diagram for *cis*-polyacetylene. Here the additional symmetry of *trans*-polyacetylene is broken.

vice versa. In Sec. 3.4.1 we solve the simplest case of collinear magnetisation, whereas in Sec. 3.4.2 we look at the general case of non-collinear magnetisation. In Sec. 3.5 we discuss our results.

3.2 Theoretical description of conducting polymers

We first consider the simplest polymer, namely polyacetylene $(CH)_x$. It exists in two variations, *trans* and *cis*-polyacetylene, see figures 3.1 and 3.2. We will use polyacetylene as a toy model for more complex polymers. Despite its relative simplicity, it already shows the gapped ground state and the exotic excitations that are typical for the whole group of conjugated polymers. We start our theoretical description with a tight-binding model that includes electron-phonon interaction. This was first proposed by Su, Schrieffer, and Heeger (SSH) [94, 95]. We then derive the continuum model proposed by Takayama, Lin-Liu, and Maki (TLM) [93], which we use to discuss the ground state and the excitations.

3.2.1 The Hamiltonian

The SSH model is defined by the Hamiltonian

$$\begin{aligned}
H_{SSH} &= H_{el} + H_{ph} + H_{el-ph}, \qquad (3.1)\\
H_{el} &= -t_0 \sum_{n,s} \left(c^{\dagger}_{n+1,s} c_{n,s} + c^{\dagger}_{n.s} c_{n+1,s} \right), \qquad (3.2)\\
H_{ph} &= \sum_{n} \frac{p_n^2}{2M} + \frac{K}{2} \sum_{n} \left(y_{n+1} - y_n \right)^2, \qquad (3.3)\\
H_{el-ph} &= \alpha \sum_{n,s} \left(y_{n+1} - y_n \right) \left(c^{\dagger}_{n+1,s} c_{n,s} + c^{\dagger}_{n.s} c_{n+1,s} \right), \qquad (3.4)
\end{aligned}$$

where H_{el} describes the hopping of the electrons on the chain, with c_n destroying an electron on the lattice site n on each carbon atom at distance a, see figure 3.1. H_{ph} describes the phonons, with y_n being the displacement coordinate of the nth atom along the chain. With H_{el-ph} the electron-phonon coupling is included. It is an addition to H_{el} with a distance dependent overlap integral proportional to $y_{n+1} - y_n$. The electronic and phononic part, following any standard text book like [96], in momentum representation read

$$\begin{aligned}
H_{el} &= \sum_{k} \varepsilon_k c^{\dagger}_k c_k, \qquad (3.5)\\
H_{ph} &= \sum_{q} \left[\frac{1}{2M} p_q p_{-q} + \frac{1}{2} M \omega_q^2 y_q y_{-q} \right], \qquad (3.6)
\end{aligned}$$

where $\varepsilon_k = -2t_o \cos ka$, and $\omega_q = 2\sqrt{K/M} |\sin \frac{qa}{2}|$, are the electron and phonon dispersion relation respectively, and where phononic momentum operator is $p_n = \frac{1}{\sqrt{N}} \sum_{k\epsilon 1^{st}BZ} p_k e^{ikna}$, the phonic displacement coordinate is $y_n = \frac{1}{\sqrt{N}} \sum_{k\epsilon 1^{st}BZ} y_k e^{ikna}$ and the electron operator is $c_n = \frac{1}{\sqrt{N}} \sum_{k\epsilon 1^{st}BZ} c_k e^{ikna}$. We have $[p_k, y_{k'}] = -i\delta_{k,k'}$ and standard anti-commutation relations apply for the fermions. N denotes the total number of electrons. The electron-phonon interaction term in momentum space reads

$$H_{el-ph} = \sum_{kq} g(k,q) y_q c^{\dagger}_{k+q} c_k, \tag{3.7}$$

where the phonon coupling strength is given by

$$g(q,k) = 2i\alpha \left(\sin{(q+k)a} - \sin ka \right). \tag{3.8}$$

A peculiarity for conjugated polymers is that one has a commensurate filling. In the simplest case, polyacetylene, one of the two states per lattice site is occupied, i.e., half

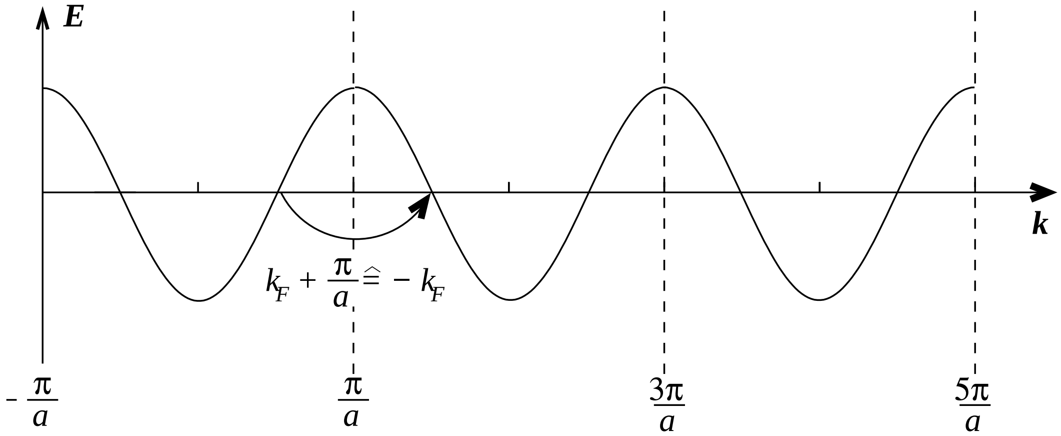

Figure 3.3: Schematic extended band structure for a one dimensional lattice with half filling without phonon effects.

filling. This will have, as we will see, drastic consequences for the ground state and the excitations. The ground state will be a chain of (C_2H_2) dimers, leading to a lattice with two atoms per unit cell and lattice spacing $2a$, instead of having a simple lattice with just one carbon per unit cell. To analyse this we expand the phonon coupling strength into *acoustical* and *optical* modes and around the Fermi momentum in lowest order

$$g(q, \pm k_F + k) = \pm i a^2 \alpha (2qk + q^2) \quad (acoustical), \tag{3.9}$$

$$g\left(\frac{\pi}{a} + q, \pm k_F + k\right) = \pm i 4\alpha \quad (optical). \tag{3.10}$$

The optical phonon mode is defined as $\tilde{y}_q = y_{\frac{\pi}{a}+q}$. Optical phonons only exist in lattices with more than one atom per unit cell. Thus it only makes sense using the term optical in the dimerised lattice. We want to find a linearised low energy theory around the Fermi points with Λ being the cutoff, as in chapter 2.2. At half filling we find the Fermi momentum and the reciprocal lattice vector being related as $k_F = \pi/2a$, see figure 3.3. We introduce left and right moving operators for the electrons on the two sides of the dispersion relation as $c_{R/L}(k) = c_{\pm k_F + k}$. Note that due to the lattice symmetries we have $c_R(\frac{\pi}{a} + k) = c_L(k)$. Thus, the electron-phonon coupling reads

$$\begin{aligned} H_{el-ph} &= i \sum_{q,k<\Lambda}{}' a^2 \alpha \left(qk + q^2\right) y_q \left(c_R^\dagger(k+q) c_R(k) - c_L^\dagger(k+q) c_L(k)\right) \\ &\quad + i \sum_{q,k<\Lambda}{}' 4\alpha \tilde{y}_q \left(c_L^\dagger(k+q) c_R(k) - c_R^\dagger(k+q) c_L(k)\right), \end{aligned} \tag{3.11}$$

where the first term is the acoustical coupling and the second represents the optical coupling, for low energies. Since the first term is quadratic in k and q and we only look at low energies we can safely neglect it. We now switch to a continuum model via $N \to \infty$

and $a \to 0$. We define new left and right moving fields as

$$c_R(k) = \int dx e^{-ikx} u(x), \tag{3.12}$$

$$c_L(k) = \int dx e^{-ikx} v(x), \tag{3.13}$$

and the dimerisation field

$$4\alpha \tilde{y}(q) = \int dx e^{-iqx} \Delta(x). \tag{3.14}$$

Summarising all terms in the Hamiltonian in this approximation and using a mean field approach, the following Bogoliubov de Gennes (BdG) equations are obtained

$$\begin{aligned} E_n u_n(x) &= -iv_F \partial_x u_n(x) + \Delta(x) v_n, \\ E_n v_n(x) &= iv_F \partial_x v_n(x) + \Delta(x) u_n, \end{aligned} \tag{3.15}$$

where $v_F = 2t_0 a$, and dimerisation field $\Delta(x)$ has to satisfy the selfconsistency equation

$$\Delta(x) = -\frac{g^2}{\omega_{ph}^2} \sum_n v_n^\dagger(x) u_n(x), \tag{3.16}$$

at $T = 0$, where $g = 4\alpha(a/M)^{1/2}$, and $\omega_{ph} = (4K/M)^{1/2}$. This model allows for analytical examination of the key properties of conducting polymers. In the next section we describe the ground state and the possible single particle excitations using the TLM model. Equation (3.15) allows for more complicated solutions than simple single particle states as described below. There is a possibility that due to hopping between single particle states a metallic band opens in the band gap [97]. In our work we only look at single particle excitations.

3.2.2 Ground state and exotic single particle excitations

The ground state of the polymer is characterised by a uniform dimerisation $\Delta(x) = \pm\Delta_0$ and the dispersion relation is found with (3.15) and (3.16) as

$$E(k) = \pm\sqrt{v_F^2 k^2 + \Delta_0^2}. \tag{3.17}$$

From total energy calculations [23,93], two minima at $\Delta_0 = \pm 0.7eV$ are found. Thus, the total energy is minimal for finite gap energy of $2\Delta_0$. From equation (3.17) it is easy to see that this ground state comes in two equivalent ways, and the sign of the dimerisation constant Δ_0 does not change the energy. $\Delta(x)$ is related to the displacement field in the following way $\Delta(na) \propto (-1)^n y_n$. So a constant Δ_0 indicates an alternating bond

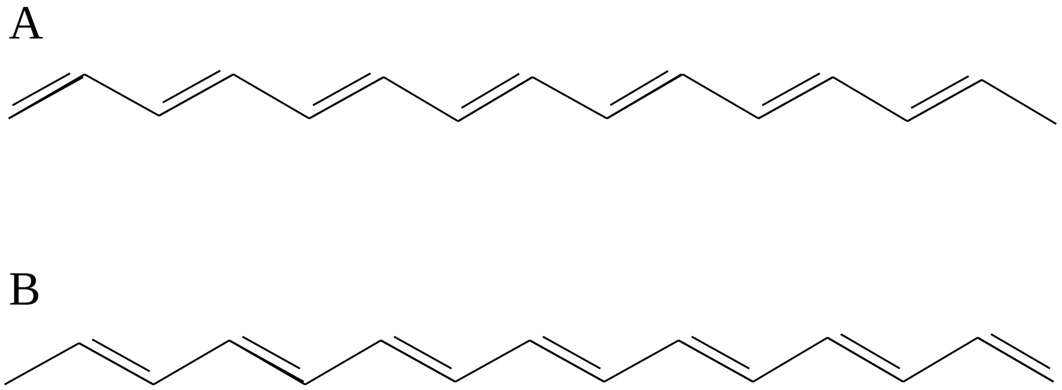

Figure 3.4: Degenerate ground states for $\Delta(x) = \pm\Delta_0$. Top: phase **A**, Bottom: phase **B**.

length in the system, i.e., dimerisation, as mentioned above. Chemically this means the bonds in the polymer backbone alternate between single and double bonds, of course for *trans*-polyacetylene it does not matter energetically if the odd or even numbered bonds are double or single bonds, causing the degeneracy of the ground state, see figure 3.4. The two different ground states are labelled phase **A** and **B**. The ground state displays a homogeneous dimerisation pattern. A gap opens at the Fermi energy, so the polymer is a semiconductor. But unlike conventional semiconductors, the lowest excitation is not an electron in the conduction band. In conducting polymers a whole range of mid gap states are possible due to the strong influence of the electron-phonon coupling.

Following [93], the first excitation we want to consider is the topological soliton solution in undoped *trans*-polyacetylene. We consider an infinite system in which the left side of the polymer is in phase **A** and the right in phase **B**. There will be a localised area in which the transition between the two phases happens. This is not dissimilar to the situation in a Bloch wall between ferromagnetic domains, where the magnetisation is turned around over a finite distance. In the transition area there will be a localised electronic state available, see figure 3.5. The width of this area is determined by the competing electronic energy that is lowered due to the possible electronic state within the transition area and the phononic energy being minimised in the dimerised phase. Now this single electron state can be filled with one, two, or zero electrons. From counting the available bonds and states the spin charge relation of this excitation is found to be exotic. There are positively and negatively charged solitons, that are spinless and chargeless spinful solitons, see figure 3.5. Mathematically, this solution is found using a variational technique and the test function

$$\Delta(x) = \Delta_0 \tanh\left(\frac{x}{\xi}\right), \tag{3.18}$$

where the width of the soliton ξ is the variational parameter. The solution of equation

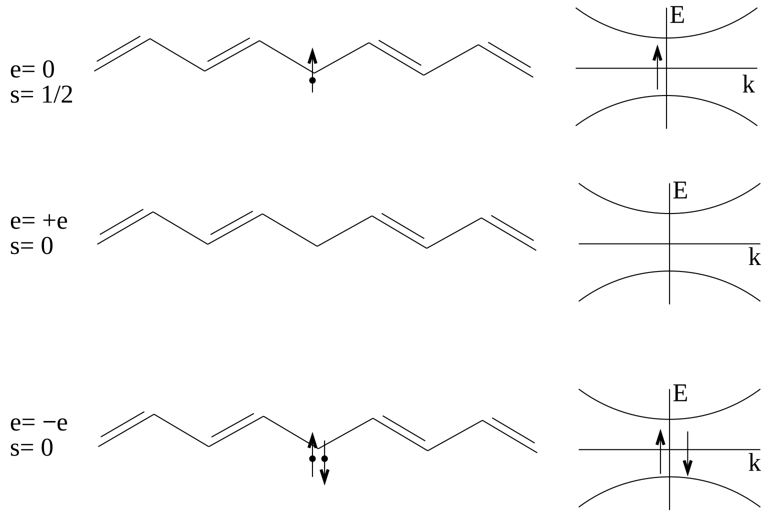

Figure 3.5: Left: Schematic figure of a soliton excitation. On the left side of the polymer the system is in phase **A** and the right in phase **B**. The single electron state can now be filled with one, two, or zero electrons. Top left: one electron causing a charge neutral but spinful excitation. Middle left: the electronic state is empty, thus one has a localised positive, but spinless charge. Bottom left: two electrons lead to a spinless negative excitation. Right: The corresponding dispersion relation with the localised midgap states is shown.

(3.15) with (3.18) is text book material [93, 98]. The width is found to be $\xi_0 = \hbar v_F/\Delta_0$, and the energy of the single particle state is in the middle of the gap. The valence and the conduction band remain the same as in the clean system without the additional state. Although in a less symmetrical situation the two possible dimeration patterns are not degenerate, see e.g., figure 3.2. The nonequivalence of the bonds is modelled via adding a constant Δ_ϵ to the dimerisation parameter $\Delta(x)$. Due to this offset in $\Delta(x)$, it is not possible that two different ground states are on each side of the excitation, hence single topological solitons cannot exist, in doped *trans*-polyacetylene or any other less symmetric polymers. It is still worthwhile to study solitons as they will be important for the understanding of the bipolaron excitation, see below.

The second kind of excitations we consider are polarons. In contrast to the topological soliton solution, in the case of polarons the dimerisation pattern does not change on the two sides of excitation. These excitations are not only possible for undoped *trans*-polyacetylene but for most conjugated polymers. Following [99] a localised electron solution is found for a dimerisation pattern described by

$$\Delta(x) = \Delta_0 - \kappa_0 v_F (t_+ - t_-) = \Delta_0 - \frac{(\kappa_0 v_F)^2}{\omega_0} s_+ s_-, \tag{3.19}$$

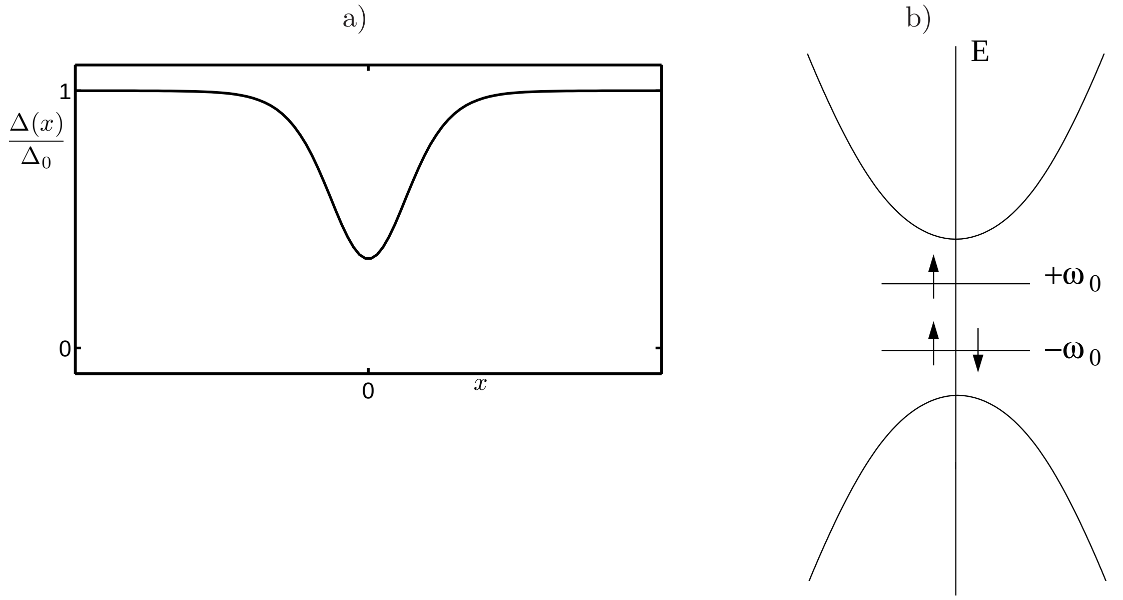

Figure 3.6: a) Dimerisation potential for a polaron excitation. b) Band structure and single particle states, here the occupation of the states leads to an electron polaron, with spin 1/2.

where $(\kappa_0 v_F)^2 + \omega_0^2 = \Delta_0^2$, and $\tanh 2\kappa_0 x_0 = \frac{\kappa_0 v_F}{\Delta_0}$, using the following abbreviations

$$t_\pm = \tanh\kappa_0(x \pm x_0), \qquad s_\pm = \mathrm{sech}\kappa_0(x \pm x_0).$$

The polaron energy is found to be $\pm\omega_0 = \Delta_0/\sqrt{2}$, having four spinful states at two energies. For a positively charged hole polaron, the lower state is singly occupied and for an electron polaron the lower state is filled with two electrons, and the upper is filled with one electron, see figure 3.6. The spin charge relation is the same as for free electrons or holes.

Total energy calculations show that only hole and electron polarons are stable in *trans*-polyacetylene. If a second electron is added to an electron polaron, a bipolaron would be obtained, but due to electron-electron repulsion, x_0 will grow infinite, to lower the energy leaving the system with effectively two separate solitons. Thus, a bipolaron would decay in the case where the ground state is degenerate into two separate kink solitons described above. The situation is different if we look at a system like *cis*-polyacetylene which, as most polymers, has a lower symmetry and one of the *groundstates*, $\pm\Delta_0$, has a lower energy than the other, leaving the system with only one real ground state. In this system the doubly charged polaron, i.e., bipolaron, can not split into two separate solitons. The distance x_0 will grow only to a point, lowering the electronic energy of the states in the gap, but the doubly charged state stays a local and stable excitation. In most

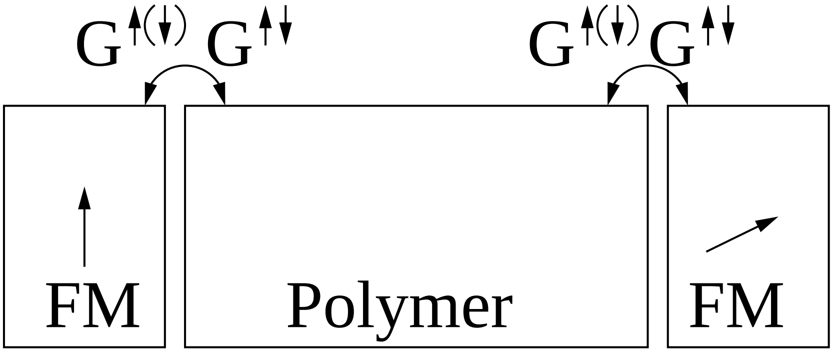

Figure 3.7: Schematic view of the two terminal device. A conducting polymer will be contacted with arbitrarily magnetised ferromagnetic contacts. $G^{\uparrow(\downarrow)}$ describe the spin dependent tunnelling into the polymer and $G^{\uparrow\downarrow}$ has to be included for noncollinear magnetisation, to account for boundary exchange effects.

polymers only polaron excitations, with conventional spin charge relation and bipolarons, which are spinless and doubly charged, are found. If a spin up polaron and a spin down polaron exist in close proximity it is possible that a bipolaron forms. This happens with a recombination rate k. The scattering rate for the opposite process, splitting up a bipolaron into two polarons, is given as b.

3.3 Modelling the transport

We now discuss spin transport through a conducting polymer. We do not attempt a microscopic modelling of the system on the basis of equation (3.15), but want to construct an effective model. The device we want to study has a typical two terminal geometry. We have two ferromagnetic contacts on each side of the polymer of length L. The left (right) ferromagnetic contact has a magnetisation in direction of the unit vector $\hat{m}_L$ ($\hat{m}_R$), see figure 3.7. Numerical studies [76–79] have established, that from the ferromagnetic contact, electrons only tunnel into polaron states near the interface, and hence we assume that the bipolaron density is zero at the edges of the polymer and no tunnelling into the bipolaron states is possible. The charge carriers in the polymer will be described via the distribution functions $\hat{f}_P(x,\epsilon)$, for the polarons and $f_{BP}(x,\epsilon)$, for the bipolarons. These functions describe the distribution of polaron and bipolarons in energy. If the size of the system is longer than the spin diffusion length these functions are also dependent on the position x along the polymer. The polaron distribution function $\hat{f}_P(x,\epsilon)$ at location $0 < x < L$ can be decomposed into a spin-independent scalar part $f_0(x,\epsilon)$ and a spin-polarisation vector $\mathbf{f}(x,\epsilon)$,

$$\hat{f}_P(x,\epsilon) = f_0\sigma_0 + \mathbf{f}\cdot\boldsymbol{\sigma}, \tag{3.20}$$

with the standard Pauli matrices σ_i in spin space, σ_0 is the unit matrix, and we assume homogeneity in the transverse direction. Note that a polaron has charge e and spin 1/2, and bipolarons are spinless with charge $2e$ [23,67]. With the average density of states $\rho(\epsilon)$, we introduce normalised densities,

$$\begin{aligned} \hat{n}_P(x) &= \int d\epsilon \rho(\epsilon) \hat{f}_P(x,\epsilon) = n_0(x) + \mathbf{n}(x)\cdot\boldsymbol{\sigma}, \\ n_{BP}(x) &= \int d\epsilon \rho(\epsilon) f_{BP}(x,\epsilon). \end{aligned} \tag{3.21}$$

These densities are defined relative to an equilibrium reference value, and reflect nonequilibrium charge and spin accumulation in the polymer. Since our model does not include the quasiparticle states outside the mean-field gap $2\Delta_0$, but only retains the polaron and bipolaron states inside the gap, we choose $\rho(\epsilon) \simeq (2\Delta_0)^{-1}\Theta(\Delta - |\epsilon|)$.

In typical organic polymers, disorder is present and implies diffusive transport for both polarons and bipolarons. To describe the diffusion we use Fick's second law, with the respective diffusion constants D_P and D_{BP}. This describes the diffusive time evolution of the normalised densities. In addition to that we add terms that describe the conversion process between polarons and bipolarons, spin relaxation, and the precession that is caused by a possible magnetic field, $\mathbf{B}$. The equations of motion for $\hat{n}_P(x,t)$ and $n_{BP}(x,t)$ are thus

$$\begin{aligned} \partial_t \hat{n}_P &= D_P \partial_x^2 \hat{n}_P - \tau_{sf}^{-1}\left(\hat{n}_P - n_0\sigma_0\right) && (3.22) \\ &\quad + i[\mathbf{h}\cdot\boldsymbol{\sigma}, \hat{n}_P]_- - S_P\sigma_0, \\ \partial_t n_{BP} &= D_{BP}\partial_x^2 n_{BP} + S_P, && (3.23) \end{aligned}$$

where τ_{sf} is the polaron spin-relaxation time and S_P models conversion processes between polarons and bipolarons [92],

$$S_P(x) = k\left(n_0^2 - \mathbf{n}^2\right) - b n_{BP}. \tag{3.24}$$

The parameter k describes the local recombination rate for two polarons of opposite spin forming a bipolaron, while b comes from the reverse process, where a bipolaron decomposes into two polarons of opposite spin. The spin precession term in equation (3.22) comes from an applied homogeneous magnetic field, where $\mathbf{h} = g\mu_B\mathbf{B}/\hbar$. We are interested in the steady-state case, where $\partial_t\hat{n}_P = \partial_t n_{BP} = 0$ in equations (3.22) and (3.23). According to Fick's first law, the stationary spin-dependent particle current in the polymer is then encoded in the 2×2 matrix in spin space

$$\hat{J}(x) = -D_P\partial_x\hat{n}_P(x) - D_{BP}\partial_x n_{BP}(x)\sigma_0. \tag{3.25}$$

Equation (3.22) yields a decoupled equation for the spin polarisation vector,

$$D_P \partial_x^2 \mathbf{n}(x) = \begin{pmatrix} \tau_{sf}^{-1} & -h_z & h_y \\ h_z & \tau_{sf}^{-1} & -h_x \\ -h_y & h_x & \tau_{sf}^{-1} \end{pmatrix} \cdot \mathbf{n}(x). \tag{3.26}$$

Equation (3.26) is a linear second order differential equation and easily solved analytically, see [81]. Given the solution to equation (3.26), by taking the scalar part of equation (3.22) and combining it with equation (3.23), the bipolaron density is determined by

$$n_{BP}(x) = -\frac{D_P}{D_{BP}} \left(\mathcal{O}\frac{x}{L} + \mathcal{P} + n_0(x) \right), \tag{3.27}$$

with two integration constants $\mathcal{O}$ and $\mathcal{P}$. The only nontrivial equation that needs to be solved is given by

$$D_P \partial_x^2 n_0 = k(n_0^2 - \mathbf{n}^2) + \frac{b D_P}{D_{BP}} \left(\frac{\mathcal{O}}{L} x + \mathcal{P} + n_0 \right). \tag{3.28}$$

As discussed above, we impose the boundary condition

$$n_{BP}(0) = n_{BP}(L) = 0, \tag{3.29}$$

since tunnelling into the polymer involves only polaron states. With equation (3.27), this implies boundary conditions for equation (3.28),

$$n_0(0) = -\mathcal{P}, \quad n_0(L) = -(\mathcal{P} + \mathcal{O}). \tag{3.30}$$

In order to solve equation (3.26), we need six additional integration constants. Therefore we have to specify boundary conditions reflecting spin and charge current continuity at the contacts to the left and right ferromagnets. The ferromagnets are taken as reservoirs with identical temperature T and chemical potentials $\mu_{L/R}$, where the applied voltage is $eV = \mu_L - \mu_R$. As before, we introduce (normalised) densities,

$$n_{L/R}^{FM} = \int d\epsilon \rho(\epsilon) n_F(\epsilon - \mu_{L/R}), \tag{3.31}$$

with the Fermi function $n_F(\epsilon) = 1/[e^{\epsilon/k_B T} + 1]$. Boundary conditions then follow by relating the current (3.25) at $x = 0$ ($x = L$) to the injected current at the left (right) interface [81],

$$\begin{aligned}\hat{J}(0) &= -\sum_{\sigma=\uparrow,\downarrow} G^{\sigma}\hat{u}_L^{\sigma}(\hat{n}_P(0) - n_L^{FM}\sigma_0)\hat{u}_L^{\sigma} - \left(G^{\uparrow\downarrow}\hat{u}_L^{\uparrow}\hat{n}_P(0)\hat{u}_L^{\downarrow} + \text{h.c.}\right), &(3.32)\\ \hat{J}(L) &= \sum_{\sigma=\uparrow,\downarrow} G^{\sigma}\hat{u}_R^{\sigma}(\hat{n}_P(L) - n_R^{FM}\sigma_0)\hat{u}_R^{\sigma} + \left(G^{\uparrow\downarrow}\hat{u}_R^{\uparrow}\hat{n}_P(L)\hat{u}_R^{\downarrow} + \text{h.c.}\right). &(3.33)\end{aligned}$$

Note that equation (3.29) implies that bipolarons do not enter this boundary condition. The matrices $\hat{u}_{L,R}^{\sigma} = \frac{1}{2}(1+\sigma\hat{m}_{L,R}\cdot\boldsymbol{\sigma})$ project the spin direction $\sigma =\uparrow,\downarrow= +,-$ in the polymer onto the respective ferromagnets magnetisation direction. For simplicity, we assumed identical spin-polarised $(G^{\uparrow}, G^{\downarrow})$ and mixing $(G^{\uparrow\downarrow})$ conductances for both contacts. They must obey $\text{Re}G^{\uparrow\downarrow} \geq (G^{\uparrow}+G^{\downarrow})/2$ [81]. The 2×2 matrix equations (3.32) and (3.33) allow us to determine the eight integration constants, and thereby yield the spin-polarised current through the system for arbitrary θ. Moreover, this gives access to the bipolaron density from equation (3.27) after solving equation (3.28). We stress that all eight integration constants do not depend on the parameters k and b in equation (3.24).

The remaining task is to solve the nonlinear equation (3.28) for $n_0(x)$ under the boundary condition (3.30), using the analytical solutions for $\mathbf{n}$. Luckily the conversion rates k and b are reported to be small [92] which allows us to use a perturbative iteration scheme and rewrite equation (3.28) as

$$\partial_x^2 n_0(x) = \kappa n_0^2(x) + \lambda n_0(x) - \mu h(x), \tag{3.34}$$

with

$$\begin{aligned}\kappa &= \frac{k}{D_P}, \quad \lambda = \frac{b}{D_{BP}}, &(3.35)\\ \mu h(x) &= \frac{1}{D_P}\left(\frac{b}{D_{BP}}(\frac{\mathcal{O}}{L}x + \mathcal{P}) + k|\mathbf{n}(x)|^2\right). &(3.36)\end{aligned}$$

We know the vector $\mathbf{n}(x)$ from the solution of equation (3.26), thus $h(x)$ is also known. Assuming that $\lambda, \mu, \kappa = O(\varepsilon)$, with $\varepsilon \ll 1$, we can now expand our ansatz perturbatively as

$$n_0(x) = \sum_{n=0}^{\infty} \varepsilon^n n_0^{(n)}(x) \tag{3.37}$$

and solve equation (3.34) by each order of ε.

$$\sum_{n=0}^{\infty} \varepsilon^n \partial_x^2 n_0^{(n)}(x) = k \sum_{n,m=0}^{\infty} \varepsilon^{n+m} n_0^{(n)} n_0^{(m)} + \lambda \sum_{n=0}^{\infty} \varepsilon n_0^{(n)} - \mu h^{(n)}(x). \tag{3.38}$$

For the lowest order we find

$$\partial_x^2 n_0^{(0)} = 0. \tag{3.39}$$

Here we use the boundary conditions (3.30) with $n_0 \approx n_0^{(0)}$. The first order equation then reads

$$\partial_x^2 n_0^{(1)}(x) = \kappa {n_0^{(0)}}^2(x) + \lambda n_0^{(0)}(x) - \mu h^{(0)}(x), \tag{3.40}$$

where we again use the boundary conditions (3.30) only this time with $n_0 \approx n_0^{(0)} + n_0^{(1)}$.

From equations (3.25) and (3.27), we can immediately see that charge current $J_c = D_P \mathcal{O}/L$ is conserved exactly,

$$\hat{J}(x) = J_c \sigma_0 + \mathbf{J}_s(x) \cdot \boldsymbol{\sigma}, \tag{3.41}$$

and the spin current, $\mathbf{J}_s(x) = -D_P \partial_x \mathbf{n}(x)$, follows from the solution of equation (3.26). Remarkably, both J_c and $\mathbf{J}_s(x)$ are independent of the polaron-bipolaron transition rates k and b in equation (3.24), and the spin-dependent current alone cannot detect the presence of bipolarons in the polymer. Nevertheless, as we show below, the bipolaron density $n_{BP}(x)$, which is induced by the nonequilibrium spin accumulation in the polymer, is sensitive magnetisation angle. As a useful measure, we will employ the integrated density,

$$N(\theta) = \int_0^L dx\; n_{BP}(x;\theta). \tag{3.42}$$

The θ-dependence of the bipolaron density is then encoded in the dimensionless quantity

$$R(\theta) = \frac{N(0) - N(\theta)}{N(0) - N(\pi)}. \tag{3.43}$$

By definition, this quantity interpolates between $R(0) = 0$ and $R(\pi) = 1$ as θ is varied from the parallel to the antiparallel configuration.

3.4 Solutions for our model

We computed the polaron and bipolaron density first for the collinear case which allows for a simple analytical solution. In the second step we computed the densities for arbitrary magnetisation of the ferromagnetic leads.

3.4.1 Collinear case: a readily solvable limit

We first discuss a simple yet important limit, where a direct analytical solution can be obtained. This limit is defined by collinear magnetisations, $\hat{m}_R = p\hat{m}_L$ with $p = \pm$ (parallel or antiparallel configuration, $\theta_+ = 0$, or $\theta_- = \pi$) and $\hat{m}_L = \hat{e}_z$. Moreover, we consider the length of the polymer as short compared to the spin coherence length, $L \ll \sqrt{D_P \tau_{sf}}$, and put $\mathbf{h} = 0$ (no magnetic field). In that case, equation (3.26) has the general solution $\mathbf{n}(x) = -(\mathbf{F}x/L + \mathbf{G})$, with constant vectors $\mathbf{F}$ and $\mathbf{G}$. For $\hat{m}_L = \hat{e}_z = \pm \hat{m}_R$, the

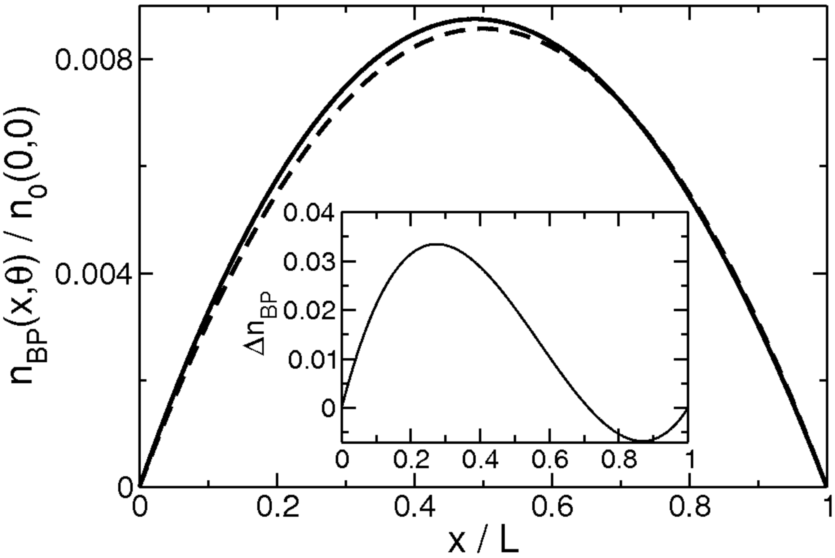

Figure 3.8: Bipolaron density $n_{BP}(x, \theta)$ in equation (3.47) for collinear magnetisations, i.e., $\theta = 0$ (solid curve) and $\theta = \pi$ (dashed curve). We use a representative parameter set for hole transport. In units where $G_P = D_P/L = 1$, the parameters are $D_{BP} = 2L/3, G^{\uparrow} = 10^4, G^{\downarrow} = 10^{-2}, k = D_P/10, b = D_{BP}/10$, $2\Delta_0 = 3.5$, $\bar{\mu} = -2$, $T = 0$, and $eV = 1$, see text. The inset shows $\Delta n_{BP} = [n_{BP}^{(+)}(x) - n_{BP}^{(-)}(x)]/n_{BP}^{(-)}(L/2)$ for the same curves.

boundary conditions (3.32) and (3.33) imply that the x and y components of both vectors vanish, and the spin current is conserved,

$$\mathbf{n}(x) = -\hat{e}_z \left(\frac{\mathcal{F}}{L} x + \mathcal{G} \right), \quad \mathbf{J}_s = \frac{D_P \mathcal{F}}{L} \hat{e}_z. \tag{3.44}$$

The four remaining integration constants $(\mathcal{O}, \mathcal{P}, \mathcal{F}, \mathcal{G})$ readily follow by solving the boundary conditions (3.32) and (3.33) [81]. For the parallel ($p = +$) configuration, they are

$$\begin{aligned} \mathcal{O}_+ &= 2(\mathcal{P}_+ + \bar{\mu}) = \frac{G^{\uparrow} G^{\downarrow} + 2(G^{\uparrow} + G^{\downarrow}) G_P}{(G^{\uparrow} + 2G_P)(G^{\downarrow} + 2G_P)} eV, \\ \mathcal{F}_+ &= -2\mathcal{G}_+ = \frac{(G^{\uparrow} - G^{\downarrow}) G_P}{(G^{\uparrow} + 2G_P)(G^{\downarrow} + 2G_P)} eV, \end{aligned} \tag{3.45}$$

while for the antiparallel ($p = -$) case, we find $\mathcal{F}_- = 0$ and

$$\begin{aligned} \mathcal{O}_- &= -2(\mathcal{P}_- + \bar{\mu}) = \frac{G^{\uparrow} G^{\downarrow}}{G^{\uparrow} G^{\downarrow} + 2G_P(G^{\uparrow} + G^{\downarrow})} eV, \\ \mathcal{G}_- &= -\frac{(G^{\uparrow} - G^{\downarrow}) G_P}{G^{\uparrow} G^{\downarrow} + 2G_P(G^{\uparrow} + G^{\downarrow})} \frac{eV}{2}, \end{aligned} \tag{3.46}$$

where $\bar{\mu} = (\mu_L + \mu_R)/2$ is the mean chemical potential and $G_P \equiv D_P/L$. The charge current for the respective configuration is then $J_c = G_P \mathcal{O}_\pm$, while the spin current is $\mathbf{J}_s = G_P \mathcal{F}_\pm \hat{e}_z$.

The last step is to solve (for given $p = \pm$) the nonlinear equation (3.28) for $n_0(x)$ under the boundary condition (3.30), using equations (3.44), (3.45) and (3.46). Using the perturbative scheme introduced above, which needs to be solved under Dirichlet boundary conditions at $x = 0$ and $x = L$, we find a solution for $n_0(x)$. Via (3.27) we find the bipolaron density for the parallel and antiparallel configuration in closed form,

$$n_{BP}^{(p=\pm)}(x) = -\frac{k}{D_{BP}}\left(\mathcal{C}_\pm x + (\mathcal{P}_\pm^2 - \mathcal{G}_\pm^2)\frac{x^2}{2} + \frac{\mathcal{P}_\pm\mathcal{O}_\pm - \mathcal{F}_\pm\mathcal{G}_\pm}{L}\frac{x^3}{3} + \frac{\mathcal{O}_\pm^2 - \mathcal{F}_\pm^2}{L^2}\frac{x^4}{12}\right), \tag{3.47}$$

where the integration constant $\mathcal{C}_\pm$ follows from the condition $n_{BP}(L) = 0$. The integrated bipolaron density $N(\theta)$ is then given for $\theta_+ = 0$ and $\theta_- = \pi$ by

$$N_\pm = \frac{kL^3}{12 D_{BP}}\left(\mathcal{P}_\pm^2 - \mathcal{G}_\pm^2 + \mathcal{P}_\pm\mathcal{O}_\pm - \mathcal{F}_\pm\mathcal{G}_\pm + \frac{3}{10}(\mathcal{O}_\pm^2 - \mathcal{F}_\pm^2)\right). \tag{3.48}$$

Note that $N_+ \neq N_-$ follows immediately from equations (3.45) and (3.46), indicating that the bipolaron density indeed is sensitive to the spin accumulation in the polymer. The bipolaron density (3.47) is shown in figure 3.8, taking parameters for sexithienyl as organic spacer [91]. Where for units defined via $G_P = D_P/L = 1$, the parameters are $D_{BP} = 2L/3, G^\uparrow = 10^4, G^\downarrow = 10^{-2}, k = D_P/10, b = D_{BP}/10$, $2\Delta_0 = 3.5$, $\bar{\mu} = -2$, $T = 0$, and $eV = 1$. A difference between the parallel and the antiparallel configuration is clearly observed. In figure 3.9 we show the scattering rates for bipolaron creation, which is proportional to $n_\uparrow n_\downarrow$, for each magnetisation. On the left side of the polymer there is more scattering for the parallel case, but at $x_0/L \simeq 0.57$ there are more scattering processes in the anti-parallel configuration. At x_0 the difference between the bipolaron densities for two configurations, Δn_{BP}, has its turning point. Overall we find the bipolaron density to be larger in the parallel case. Although the current is not sensitive to the polaron-bipolaron transition rates k and b, the bipolaron density is influenced by the nonequilibrium spin accumulation in the polymer.

3.4.2 Noncollinear magnetisation

In the general case of arbitrary angle θ between $\hat{m}_L$ and $\hat{m}_R$, the problem is solved in an analogous manner but the equations become less transparent. The main difference is that now the mixing conductance $G^{\uparrow\downarrow}$ has to be taken into account. However, as reported previously [91], we find that the results are practically independent of the precise choice

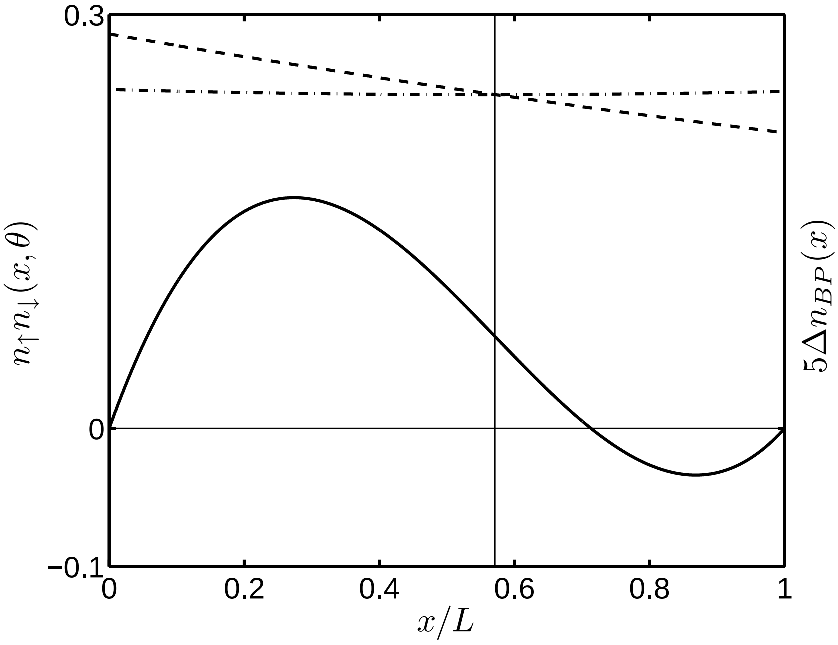

Figure 3.9: The scattering rate for bipolaron creation is proportional to $n_\uparrow n_\downarrow(x,\theta)$. This rate is shown for $\theta = 0$ (dashed curve) and $\theta = \pi$ (dot dashed curve). The solid curve shows the change in bipolaron density for the respective magnetisations $\Delta n_{BP} = [n_{BP}^{(+)}(x) - n_{BP}^{(-)}(x)]/n_{BP}^{(-)}(L/2)$ (scaled with factor 5 for clarity). It is clearly seen that in the parallel case there is a bigger scattering rate at first, and hence more bipolarons. The two rates cross at $x/L = 0.57$ which is exactly the point of inflection in the bipolaron density difference, see vertical line. We used the same parameter set as in figure 3.8

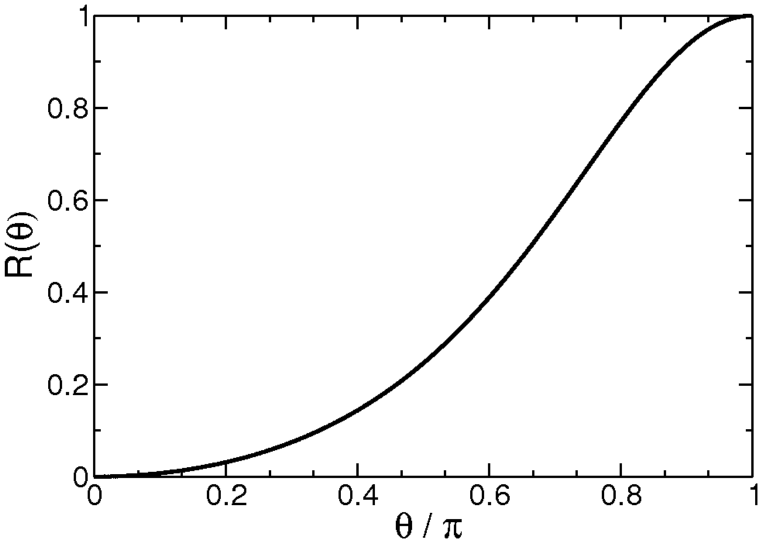

Figure 3.10: Spin accumulation sensitivity $R(\theta)$, see equation (3.43), of the bipolaron density as a function of the magnetisation tilt angle. Parameters are as in figure 3.8, additionally we set $\mathrm{Re}G^{\uparrow\downarrow} = \mathrm{Im}G^{\uparrow\downarrow} = 5.1 \times 10^3$.

for $G^{\uparrow\downarrow}$. We find a smooth crossover between the limiting values for $\theta = 0$ and $\theta = \pi$, see equation (3.47), illustrated for the integrated bipolaron density (3.42) in figure 3.10. We further find that even in the general case the spin current is not sensitive to polaron-bipolaron scattering rates k and b.

3.5 Discussion

In this chapter, we have discussed spin transport in doped organic polymers, employing a diffusive description of polaron and bipolaron transport. Under a two-terminal setup, where the polymer is sandwiched by (generally noncollinear) ferromagnetic electrodes, see figure 3.7, the problem can be solved analytically by exploiting the smallness of the polaron-bipolaron transition rates k and b. While the spin-dependent current through the device turns out to be independent of k and b, the nonequilibrium bipolaron density is a sensitive probe of spin accumulation. The possibility to measure this density in optical-absorption experiments [100–102], e.g., by adapting charge-modulation techniques [103] to the two-terminal transport geometry considered here, may offer a novel way to probe spin accumulation in organic polymers.

Our work generalises previous studies where bipolarons were neglected [91] or only a single ferromagnet-polymer interface was considered [92]. We also treat the nonequilibrium situation due to an applied voltage self-consistently instead of postulating the existence of a uniform electric field [92]. We mention in passing that a recent Monte Carlo simulation of bipolaron effects on the magnetoresistance [104] did also not consider magnetic contacts, but instead described the effect of low homogeneous magnetic field on the bipolaron formation rate. Another recent theoretical study [105] on magnetoresistance in polymers with polaron and bipolaron carriers used a diffusive approach and magnetic contacts (ferromagnet-polymer-ferromagnet configuration). In contrast to our work, however, Ref. [105] does not take into account conversion processes between polaron and bipolaron states, but simply assumes a constant density of bipolarons and includes this into the transport calculations. Surprisingly, a dependence of the magnetoresistance on the ratio of bipolarons and polarons is reported [105], whereas we find the spin-polarised current to be independent of the bipolaron formation rate. Our finding can be traced back to the well-established [78, 79] suppression of tunnelling into bipolaron states near the interface with a ferromagnetic electrode. This feature is ignored when simply assuming a constant bipolaron density.

Chapter 4

Optical conductivity in Graphene: Effects of spin-orbit coupling

4.1 Introduction

Graphene is a single sheet of carbon atoms forming a two-dimensional honeycomb lattice, see figure 1.5 and 4.1. It is the basic building block for other carbon based materials, like the football shaped fullerenes, and rolled up carbon nanotubes, and simply stacked graphene sheets making up graphite. Pure two dimensional lattices were thought to be unstable and curl up [25], but disproving this graphene has recently become available for experimental scrutiny. Its exotic physical properties have spurred a lot of interest [6, 7]. Known theoretically since the late 1940s [106, 107], graphene is a promising candidate for nano-sized applications due to its exceptional electronic properties [108].

The electronic band structure of graphene is that of a semimetal with the valence and the conduction band touching each other at the K points. The conical shape of conduction and valence bands near the K points in the Brillouin zone renders graphene an interesting type of quasi-relativistic condensed-matter system [109, 110] where massless Dirac-fermion-like quasiparticles are present at low energy. In contrast to the truly relativistic case, the spin degree of freedom in the Dirac equation here corresponds to a pseudo-spin that distinguishes degenerate states on two sublattices formed by two nonequivalent atom sites present in the unit cell of the hexagonal lattice.

The pseudo-spin degeneracy (the states on both lattice sites are energetically equivalent) can be broken by spin-orbit interaction, which mixes pseudospin degree of freedom with the real spin. This of course opens the opportunity to make use of this spin-orbit coupling for spintronic devices and consequently there has been huge interest in spin-orbit interaction in graphene, resulting in a large body of theoretical [111–121] and experimental [122–124] work. It is agreed that there are two main causes for the spin-orbit interaction

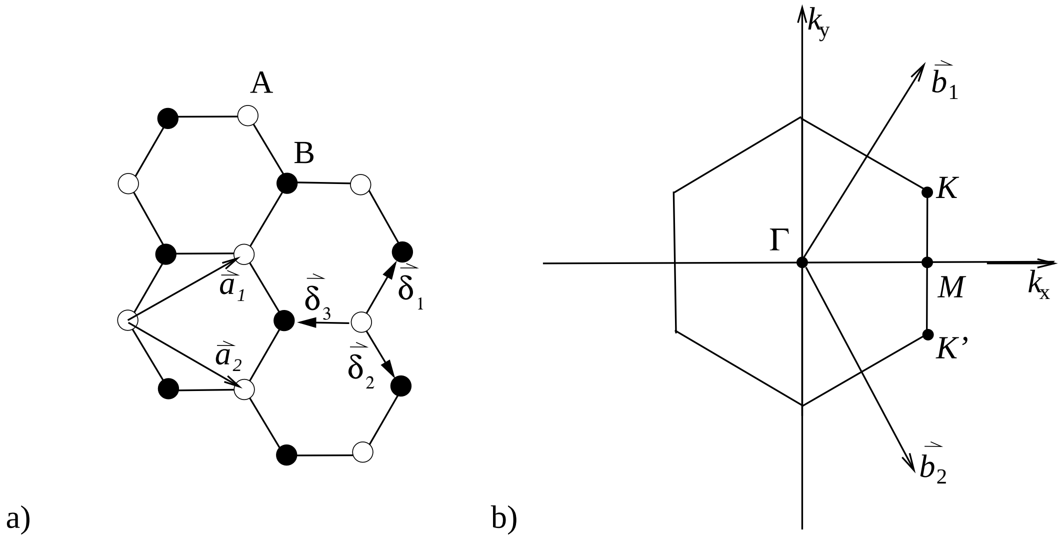

Figure 4.1: a) Carbon atoms form a hexagonal lattice. $\vec{\delta}_i$ define the distance between next neighbours and $\vec{a}_j$ define the unit cell. There are two inequivalent lattice sites per unit cell, denoted **A** and **B**. b) Reciprocal lattice with the reciprocal lattice vectors $\vec{b}_{1,2}$ and the symmetry points Γ, M, K, and K'. The Fermi point are K and K'.

in graphene. Firstly, external electric fields (e.g., due to the presence of a substrate or a back-gate) and local curvature fields (ripples), induce a spin-orbit coupling [115] whose coupling strength we denote by Δ_R. We refer to this contribution as the *Rashba* spin-orbit interaction in the following. Secondly, there is an *intrinsic* spin-orbit interaction with strength Δ_I, which is caused by the atomic Coulomb potentials.

In this chapter, we present a theoretical analysis of graphene's optical conductivity $\sigma(\omega)$, extending previous studies [125–131] to the situation with finite spin-orbit interaction. Spin-orbit interaction effects on the DC conductivity were investigated in a recent theoretical study for a bipolar graphene *pn* junction [132], and the effect of intrinsic spin-orbit interaction on the polarisation-dependent optical absorption of graphene was considered in [133]. Our study presents the analogous scenario for the richer case of the optical conductivity when both intrinsic and extrinsic types of spin-orbit interaction are present. Since Δ_R can be tuned by external fields, we will analyse various situations distinguished by the relative strengths of Δ_R and Δ_I.

Our findings suggest that optical-conductivity measurements can be useful to identify and separate different spin-orbit interaction sources. We work on the simplest theory level (linear response theory, no interactions, no disorder) and disregard boundary effects for the moment. The structure of the remainder of this chapter is as follows. In section 4.2 we present the theory of graphene first for flat graphene, and then summarise the derivation of the spin-orbit coupling terms. In section 4.3, we summarise basics of our calculation of the optical conductivity based on the Kubo formalism. In section 4.4, we show results for different relative magnitudes of spin-orbit interaction strengths at finite temperature T and chemical potential μ. Finally, in section 4.5, we summarise our results and discuss their applicability to actual experiments.

4.2 Theoretical description of graphene

In this section we present the theory of graphene. Starting from a tight-binding model we summarise the derivation of the effective low energy Hamiltonian including the spin-orbit coupling terms.

4.2.1 Clean flat Graphene

We first outline the derivation of the dispersion relation of flat graphene without spin-orbit coupling, following [108]. We use a nearest neighbour tight-binding model for the derivation of the bandstructure. In graphene the carbon atoms form a two dimensional honeycomb lattice. The honeycomb lattice is a triangular lattice with two atoms per unit cell, see figure 4.1 a), defined by the two unit vectors

$$\vec{a}_1 = \frac{a}{2}(3, \sqrt{3}), \qquad \vec{a}_2 = \frac{a}{2}(3, -\sqrt{3}) \tag{4.1}$$

where $a \simeq 1.42$ Å is the interatomic distance between the carbon atoms, and the three nearest neighbour vectors are

$$\vec{\delta}_1 = \frac{a}{2}(1, \sqrt{3}), \quad \vec{\delta}_2 = \frac{a}{2}(1, -\sqrt{3}), \quad \vec{\delta}_3 = \frac{a}{2}(1, \sqrt{3}). \tag{4.2}$$

The corner points of the Brillouin zone K and K' are especially important for the physics of graphene and are given by

$$\vec{K} = \frac{2\pi}{3a}\left(1, \frac{1}{\sqrt{3}}\right), \qquad \vec{K}' = \frac{2\pi}{3a}\left(1, -\frac{1}{\sqrt{3}}\right). \tag{4.3}$$

There are four electrons in each carbon atom. Three σ electrons are responsible for the bonding of the lattice and the remaining out of plane π states hybridise and electrons can hop from atom to atom. The tight-binding Hamiltonian for the π electrons in the nearest neighbours approximation reads

$$H_0 = -t\hbar \sum_{\vec{n},\vec{\delta}_i} a^\dagger_{\vec{n}} b_{\vec{n}+\vec{\delta}_i} + a_{\vec{n}} b^\dagger_{\vec{n}+\vec{\delta}_i}, \tag{4.4}$$

where $a_{\vec{n}}^{(\dagger)}$ and $b_{\vec{n}}^{(\dagger)}$ are creation and destruction operators in the respective sublattice. A straightforward calculation [106] yields the energy bands as

$$E_{\pm}(\vec{k}) = \pm t\hbar\sqrt{3 + 2\cos\left(\sqrt{3}k_y a\right) + 4\cos\left(\frac{\sqrt{3}}{2}k_y a\right)\left(\frac{3}{2}k_x a\right)}, \tag{4.5}$$

where the plus sign applies for the upper π^* band (conduction band) and the minus sign for the lower π band (valence band). The Fermi energy for undoped graphene is at zero. The valence and conduction bands touch each other at the Fermi points K and K', see figure 4.2. Thus clean single layer graphene is a semimetal. In our computation we only consider low energies and it is justified to linearise the dispersion relation around the two Fermi points. Introducing $\vec{k} = \vec{K}^{(\prime)} + \vec{q}$, the linearised dispersion reads

$$\varepsilon_{\pm}(\vec{q}) = \pm v_F \hbar |\vec{q}|, \tag{4.6}$$

where the Fermi velocity is defined as $v_F = 3ta/2$. With $\vec{q} \to \vec{k}$ the Hamiltonian in momentum space can be cast as

$$H_0(\vec{k}) = \hbar v_f \left(k_x\sigma_x + k_y\tau_z\sigma_y\right), \tag{4.7}$$

where the Pauli matrices $\sigma_{x,y}$ act in sublattice space, which is referred to as pseudo-spin space. The eigenvectors of σ_z correspond to quasiparticle states that are localised on sites of the sublattices **A** and **B**. The Pauli matrices $\tau_{x,y,z}$ act in the valley space spanned by the states near the $K^{(\prime)}$ points. The kinetic Hamiltonian is diagonal in spin space, which for later reference will be described by the set of Pauli matrices $s_{x,y,z}$. The Hamiltonian is represented by an 8×8 matrix in the basis

$$(A\uparrow K, B\uparrow K, A\downarrow K, B\downarrow K, A\uparrow K', B\uparrow K', A\downarrow K', B\downarrow K'). \tag{4.8}$$

The Hamiltonian (4.7) resembles the massless relativistic Dirac Hamiltonian, in which the pseudospin plays the role of the real spin in the relativistic theory. Therefore the quasiparticles in graphene behave like massless relativistic particles with velocity v_F.

4.2.2 Including spin-orbit coupling

In this section we introduce spin-orbit coupling into our system. There are mainly three ways to find an effective Hamiltonian that includes spin-orbit coupling. The authors of [114, 120] derive the spin-orbit coupling terms from symmetry arguments in graphene. Secondly the authors of [134–136] used density functional calculation to estimate the strength of the spin-orbit coupling, whereas the authors of [115, 116] derive the same spin-

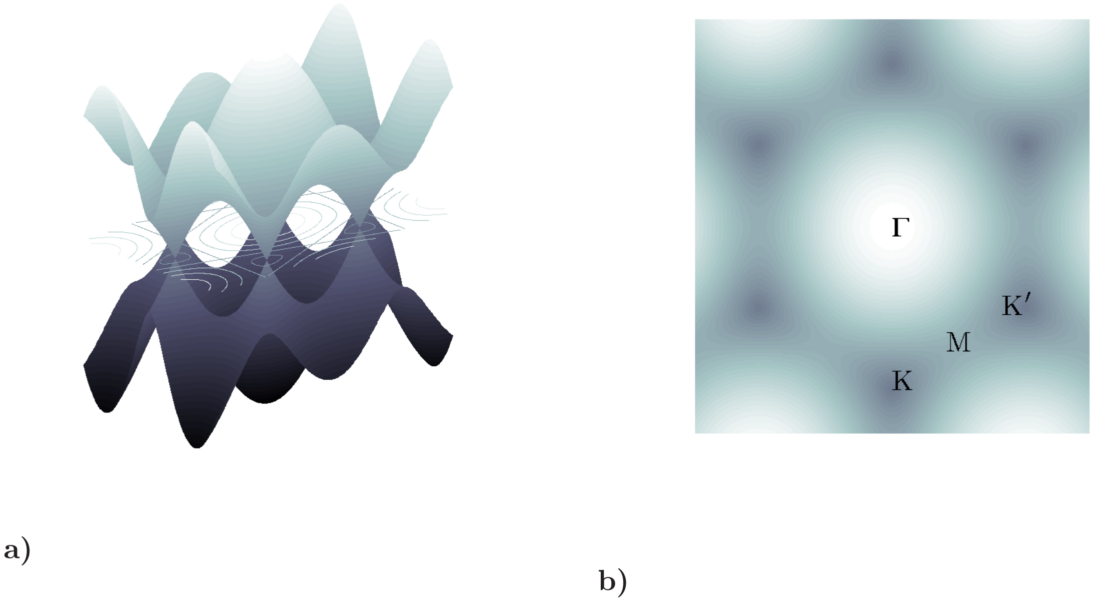

Figure 4.2: a) Tight-binding approximation of the bandstructure of graphene. One can clearly see the linear cones at the K and K' points, where the hole states (dark blue) and electron states (lighter blue) spectra touch each other. b) Top view of the bandstructure with symmetry points.

orbit coupling terms from a tight-binding approach. This approach includes not only the π electrons as above, but also considers hopping between the s and $p_{x,y,z}$ states of the carbon atoms. This results in a mixing of the σ and π band due to either an applied electric field or curvature. One also introduces a term describing the intrinsic atomic spin-orbit interaction. Here we briefly summarise the latter approach.

Min et al. [116] use a two centre Slater Koster [137] approximation for nearest neighbour hopping. They introduce the onsite energies t_s and t_p for the s and p orbital respectively, and hopping constants between all the orbitals $t_{\mu,\mu'}$, where $\mu^{(\prime)} = s, p_{x,y,z}$. To account for the inner atomic spin-orbit coupling they include a local atomic term

$$H_{at} = \sum_{n,l} P_{nl} \xi_l \vec{L}_n \vec{S}_n, \tag{4.9}$$

where n is the site index, P_{nl} is the projection operator onto angular momentum l on site n respectively, ξ_n is the atomic spin-orbit coupling constant for angular momentum l, and $\vec{S}_n$ and $\vec{L}_n$ are the spin and the angular momentum operators on site n. It is easy to see that the spin-orbit coupling does not appear for the s electrons in lowerst order. An applied gate voltage and the effective perpendicular electric field E resulting from that, lifts the inversion symmetry of graphene. This can be modelled by adding a local atomic

Stark effect term

$$H_E = eE \sum_n z_i. \tag{4.10}$$

Note that also curvature of the graphene sheet lifts the inversion symmetry. The effective spin-orbit Hamiltonian for the π bands is now derived in a second order perturbation approach, using the hopping Hamiltonian as the unperturbed Hamiltonian and $\Delta H = H_{at} + H_E$ as the perturbation. The effective Hamiltonian found this way given in basis (4.8) then reads

$$H_{at} + H_E \simeq H_{SO} = H_I + H_R, \tag{4.11}$$

where the single terms read

$$H_I = \Delta_I \, \sigma_z \tau_z s_z - \Delta_I, \tag{4.12}$$

which describes the effect of inner atomic intrinsic, spin-orbit coupling. The electric field (Rashba) term in the effective Hamiltonian reads

$$H_R = \frac{\Delta_R}{2} \left(\sigma_x \tau_z s_y - \sigma_y s_x\right), \tag{4.13}$$

where the effect of curvature is found to add onto the electric field induced term as $\Delta_R = \Delta_E + \Delta_{curv}$ [115]. The estimates for the constants Δ_I and Δ_R vary in the different approaches and experiments and spur an ongoing discussion which we aim to contribute to via finding measurable and distinguishable effects of the two couplings, i.e., in the low energy optical conductivity.

4.3 Optical conductivity

We compute the optical conductivity using the standard Kubo formula [138],

$$\sigma_{ab} = \int_{-\infty}^{0} dt \; e^{i(\omega - i0^+)t} K_{ab}(t), \tag{4.14}$$

where $a, b = x, y$ and the kernel reads

$$K_{ab} = \frac{ie}{\hbar} \mathrm{Tr} \left[e^{-\frac{i}{\hbar} H(\vec{k})t} j_a e^{\frac{i}{\hbar} H(\vec{k})t} \left[r_b, \rho_0\right] \right]. \tag{4.15}$$

Here ρ_0 is the equilibrium density matrix and the current operators are

$$j_a = \frac{ie}{\hbar} \left[H(\vec{k}), r_a \right] = \frac{e}{\hbar} \frac{\partial H(\vec{k})}{\partial k_a}. \tag{4.16}$$

Following [125], we use the single-particle eigenstates $|n\rangle$ and eigenenergies ε_n. The conductivity then reads

$$\begin{aligned}\sigma_{ab}(\omega) &= \frac{e^2}{i}\sum_{n,n'} \frac{\langle n\,|[H,r_a]|\,n'\rangle\,\langle n'\,|[H,r_b]|\,n\rangle}{(\varepsilon_{n'}-\varepsilon_n)(\varepsilon_{n'}-\varepsilon_n+\hbar\omega-i0^+)} \\ &\qquad\times\left[f(\varepsilon_n)-f(\varepsilon_{n'})\right], \end{aligned} \tag{4.17}$$

where $f(\varepsilon)$ is the Fermi-Dirac distribution

$$f(\varepsilon)=\frac{1}{e^{\beta(\varepsilon-\mu)+1}}, \tag{4.18}$$

containing the chemical potential μ and the inverse temperature $\beta=1/k_BT$.

In the absence of a magnetic field, the off-diagonal entries vanish, $\sigma_{xy}=0$, while symmetry arguments show that $\sigma_{xx}=\sigma_{yy}\equiv\sigma(\omega)$.

4.3.1 Graphene without spin-orbit coupling

First, we illustrate this formula by computing the optical conductivity of a clean system without spin-orbit coupling described by the spin degenerate Hamiltonian at one K point

$$H_0(\vec{k})=\begin{pmatrix} 0 & k_x-ik_y \\ k_x+ik_y & 0 \end{pmatrix}, \tag{4.19}$$

where we chose the basis to be (A,B). The Hamiltonian at the K' point is obtained via a unitary transformation and thus holds the same physics. Therefore the degeneracy factor is $g_v=4$. The energy reads $\varepsilon_\nu(\vec{k})=\pm v_F\hbar|\vec{k}|$ with the eigenstates

$$|n\rangle=|\vec{k}\rangle\otimes|\nu\rangle_{\vec{k}}, \tag{4.20}$$

composed of a plane wave state $\left|\vec{k}\right\rangle\sim e^{i\vec{k}\cdot\vec{x}}$, and a $\vec{k}$-dependent pseudospinor $|\nu\rangle_{\vec{k}}$, which reads

$$|\nu\rangle_{\vec{k}}=\frac{1}{\sqrt{2}}\left(-\nu\frac{\sqrt{k_x^2+k_y^2}}{(k_x+ik_y)},1\right), \tag{4.21}$$

where $\nu=\pm1$. The components of the current read

$$j_x=ev\begin{pmatrix} 0 & 1 \\ 1 & 0 \end{pmatrix},\quad \text{and}\quad j_y=ev\begin{pmatrix} 0 & -i \\ i & 0 \end{pmatrix}. \tag{4.22}$$

At finite ω in the clean system, only the inter-band contribution to the conductivity is relevant. Using the well known identity

$$\lim_{0^+\to 0}\frac{1}{\omega - i0^+} = \mathcal{P}\left[\frac{1}{\omega}\right] + i\pi\delta(\omega), \tag{4.23}$$

in equation (4.17), where $\mathcal{P}[1/\omega]$ denotes the Cauchy principal value of $1/\omega$, the real part of the conductivity is given by

$$\begin{aligned} \mathrm{Re}\ \sigma(\omega) &= \pi e^2 \int \frac{d^2\vec{k}}{(2\pi)^2} {\sum}' |w^a_{\nu,\nu'}(\vec{k})|^2 \frac{f(\varepsilon_{\vec{k},\nu}) - f(\varepsilon_{\vec{k},\nu'})}{\varepsilon_{\vec{k},\nu'} - \varepsilon_{\vec{k},\nu}} \\ &\quad \times \left[\delta(\varepsilon_{\vec{k},\nu} - \varepsilon_{\vec{k},\nu'} + \hbar\omega) + \delta(\varepsilon_{\vec{k}\nu'} - \varepsilon_{\vec{k}\nu} + \hbar\omega)\right], \end{aligned} \tag{4.24}$$

where

$$w^a_{\nu,\nu'}(\vec{k}) = {}_{\vec{k}}\langle \nu | \, j_a \, | \nu' \rangle_{\vec{k}}\,,$$

are the current operator matrix elements in the eigenbasis, and $\sum' = \sum_{\nu\neq\nu'}$. We also used

$$w^a_{\nu,\nu'}(\vec{k}) = \left[w^a_{\nu',\nu}(\vec{k})\right]^\dagger,$$

since the current operator is Hermitian. In what follows, we restrict ourselves to the real part of $\sigma(\omega)$ and omit the “Re” sign. After integrating and summing up all the degeneracies we obtain

$$\sigma(\omega) = \frac{e^2}{4\hbar}\left(f\left(-\frac{\hbar\omega}{2}\right) - f\left(\frac{\hbar\omega}{2}\right)\right). \tag{4.25}$$

The result is shown in figure 4.3.

4.3.2 Graphene with spin-orbit coupling

We now compute the optical conductivity of graphene including the intrinsic and the Rashba spin-orbit coupling. The Hamiltonian for the low-energy continuum description of graphene [108, 114–116, 120] reads,

$$H(\vec{k}) = H_0(\vec{k}) + H_R + H_I, \tag{4.26}$$

as shown above in (4.7), (4.13) and (4.12). The full Hamiltonian matrix turns out to be block-diagonal in the valley degree of freedom, and each block can be transformed into the other via a unitary transformation. The spin degeneracy is now broken due to the additional terms $H_R + H_I$. The bulk spectrum (ignoring subtleties related to the topological insulator phase encountered for $2\Delta_I > \Delta_R$ [114] for now) can then be obtained

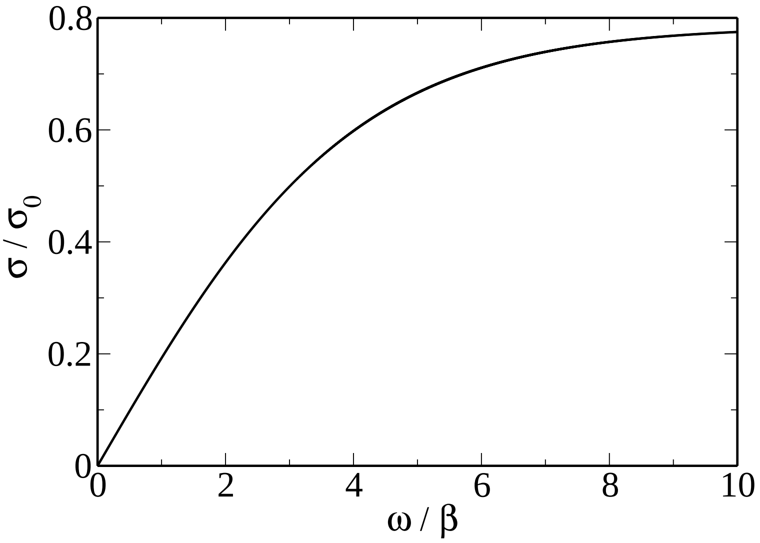

Figure 4.3: Optical conductivity for a flat sheet of graphene without spin-orbit coupling, where $\sigma_0 = 2e^2/h$. For $\omega \to \infty$ the optical conductivity reaches the universal value $e^2/(4\hbar)$.

from a 4×4 Hamiltonian matrix in the basis

$$(A\uparrow, B\uparrow, A\downarrow, B\downarrow) \tag{4.27}$$

at one K point

$$H(\vec{k}) = \begin{pmatrix} 0 & k_x - ik_y & 0 & 0 \\ k_x + ik_y & -2\Delta_I & -i\Delta_R & 0 \\ 0 & i\Delta_R & -2\Delta_I & k_x - ik_y \\ 0 & 0 & k_x + ik_y & 0 \end{pmatrix}. \tag{4.28}$$

The valley degree of freedom then merely manifests itself as a degeneracy factor $g_v = 2$. The energy spectrum is obtained as

$$\varepsilon_{\vec{k},\nu\nu'} = \frac{1}{2}\left(\nu'\Delta_R + \nu\sqrt{4(\hbar v_F)^2 \mid \vec{k} \mid + (\Delta_R - 2\nu'\Delta_I)^2} - 2\Delta_I\right), \tag{4.29}$$

where the combined indices $\nu, \nu' = \pm 1$ label the four bands. The corresponding eigenstates

$$|n\rangle = |\vec{k}\rangle \otimes |\nu\nu'\rangle_{\vec{k}}, \tag{4.30}$$

are composed of a plane wave state $\left|\vec{k}\right\rangle \sim e^{i\vec{k}\cdot\vec{x}}$, and a $\vec{k}$-dependent 4-spinor $|\nu\nu'\rangle_{\vec{k}}$, which reads in basis (4.27)

$$|\nu\nu'\rangle_{\vec{k}} = \frac{1}{N_{\nu\nu'}}\left(-\nu'\frac{ik_x+k_y}{k_x+ik_y}, -i\frac{\Delta_{-\nu'}+\nu\nu'\sqrt{4|\vec{k}|^2+\Delta_{-\nu'}^2}}{2(k_x+ik_y)}, -\frac{\Delta_{-\nu'}-\nu\sqrt{4|\vec{k}|^2+\Delta_{-\nu'}^2}}{2(k_x+ik_y)}, 1\right)^T, \tag{4.31}$$

where we used the definition $\Delta_\pm = \Delta_R \pm 2\Delta_I$, and $N_{\nu\nu'}$ normalises the spinor to unity. In the basis (4.27) the components of the current read

$$j_x = ev\begin{pmatrix} 0 & 1 & 0 & 0 \\ 1 & 0 & 0 & 0 \\ 0 & 0 & 0 & 1 \\ 0 & 0 & 1 & 0 \end{pmatrix}, \text{ and } j_y = ev\begin{pmatrix} 0 & -i & 0 & 0 \\ i & 0 & 0 & 0 \\ 0 & 0 & 0 & -i \\ 0 & 0 & i & 0 \end{pmatrix}. \tag{4.32}$$

As in the last section we only consider the inter-band contribution to the conductivity. Again using (4.23) in equation (4.17) the real part of the conductivity is given by

$$\begin{aligned}\sigma(\omega) &= \pi e^2\int\frac{d^2\vec{k}}{(2\pi)^2}{\sum}'|w^a_{\kappa\nu,\kappa'\nu'}(\vec{k})|^2\times\frac{f(\varepsilon_{\vec{k},\kappa\nu})-f(\varepsilon_{\vec{k},\kappa'\nu'})}{\varepsilon_{\vec{k},\kappa'\nu'}-\varepsilon_{\vec{k},\kappa\nu}} \\ &\quad\times\left[\delta(\varepsilon_{\vec{k},\kappa\nu}-\varepsilon_{\vec{k},\kappa'\nu'}+\hbar\omega)+\delta(\varepsilon_{\vec{k}\kappa'\nu'}-\varepsilon_{\vec{k}\kappa\nu}+\hbar\omega)\right],\end{aligned} \tag{4.33}$$

where

$$w^a_{\kappa\nu,\kappa'\nu'}(\vec{k}) = {}_{\vec{k}}\langle\kappa\nu|\,j_a\left|\kappa'\nu'\right\rangle_{\vec{k}},$$

are the current operator matrix elements in the eigenbasis, and $\sum' = \sum_{(\kappa\nu)\neq(\nu'\kappa')}$. We restrict ourselves to the real part of $\sigma(\omega)$, having omitted the "Re" sign. The result obtained for $\omega > 0$ can be expressed very generally as

$$\frac{\sigma(\omega)}{\sigma_0} = \sum_{n=1}^{6} F_n(\omega, \Delta_R, \Delta_I, \beta, \mu), \tag{4.34}$$

where $\sigma_0 = 2e^2/h$, and with the Heaviside function Θ, the quantities F_n are given by

$$\begin{aligned}
F_1 &= \tilde{F}_1\ \Theta(\hbar\omega - |\Delta_R - 2\Delta_I|), \\
F_2 &= \tilde{F}_2\ \Big[\Theta(\Delta_R - 2\Delta_I)\Theta(\hbar\omega - \Delta_R)\Theta(2\Delta_I + \Delta_R - \hbar\omega) \\
&\quad +\Theta(2\Delta_I - \Delta_R)\Theta(\hbar\omega - \Delta_R)\Theta(2\Delta_R - \hbar\omega)\Big], \\
F_3 &= \tilde{F}_3\ \Big[\Theta(\Delta_R - 2\Delta_I) + \Theta(2\Delta_I - \Delta_R)\Theta(\hbar\omega - 2\Delta_I + \Delta_R)\Big], \\
F_4 &= \tilde{F}_4\ \Big[\Theta(\Delta_R - 2\Delta_I)\Theta(\hbar\omega - 2\Delta_R) + \Theta(2\Delta_I - \Delta_R)\Theta(\hbar\omega - 2\Delta_I - \Delta_R)\Big], \\
F_5 &= \tilde{F}_5\ \Big[\Theta(\Delta_R - 2\Delta_I)\Theta(\hbar\omega - \Delta_R + 2\Delta_I)\Theta(\Delta_R - \hbar\omega) + \Theta(2\Delta_I - \Delta_R)\Theta(\Delta_R - \hbar\omega)\Big], \\
F_6 &= \tilde{F}_6\ \Theta(\hbar\omega - 2\Delta_I - \Delta_R). \qquad (4.35)
\end{aligned}$$

In figure 4.4, we show the regions in Δ_R-Δ_I-plane where the different $\tilde{F}_n$ contribute. To express the six functions $\tilde{F}_n(\omega, \Delta_R, \Delta_I, \beta, \mu)$, with $n = 1, \ldots, 6$, entering equation (4.35) we use the following abbreviations:

$$\begin{aligned}
\epsilon_1(y) &= \frac{1}{2}\left(\Delta_R - \sqrt{(\Delta_R - 2\Delta_I)^2 + 4y^2} - 2\Delta_I\right), \\
\epsilon_2(y) &= \frac{1}{2}\left(\Delta_R + \sqrt{(\Delta_R - 2\Delta_I)^2 + 4y^2} - 2\Delta_I\right), \\
\epsilon_3(y) &= \frac{1}{2}\left(-\Delta_R - \sqrt{(\Delta_R + 2\Delta_I)^2 + 4y^2} - 2\Delta_I\right), \\
\epsilon_4(y) &= \frac{1}{2}\left(-\Delta_R + \sqrt{(\Delta_R + 2\Delta_I)^2 + 4y^2} - 2\Delta_I\right).
\end{aligned}$$

Furthermore, we define the quantities (setting $\hbar = 1$ for simplicity)

$$y_1 = \frac{1}{2}\sqrt{-4\Delta_I^2 + 4\Delta_I\Delta_R - \Delta_R^2 + \omega^2},$$

$$y_2 = \frac{\sqrt{\omega}\sqrt{8\Delta_I^2\Delta_R - 2\Delta_R^3 - 4\Delta_I^2\omega + 5\Delta_R^2\omega - 4\Delta_R\omega^2 + \omega^3}}{\sqrt{4\Delta_R^2 - 8\Delta_R\omega + 4\omega^2}},$$

$$y_3 = \frac{\sqrt{-8\Delta_I^2\Delta_R\omega + 2\Delta_R^3\omega - 4\Delta_I^2\omega^2 + 5\Delta_R^2\omega^2 + 4\Delta_R\omega^3 + \omega^4}}{2\sqrt{\Delta_R^2 + 2\Delta_R\omega + \omega^2}},$$

$$y_4 = \frac{\sqrt{\omega}\sqrt{8\Delta_I^2\Delta_R - 2\Delta_R^3 - 4\Delta_I^2\omega + 5\Delta_R^2\omega - 4\Delta_R\omega^2 + \omega^3}}{\sqrt{4\Delta_R^2 - 8\Delta_R\omega + 4\omega^2}},$$

$$
\begin{aligned}
y_5 &= \frac{\sqrt{\omega}\sqrt{8\Delta_I^2\Delta_R - 2\Delta_R^3 - 4\Delta_I^2\omega + 5\Delta_R^2\omega - 4\Delta_R\omega^2 + \omega^3}}{\sqrt{4\Delta_R^2 - 8\Delta_R\omega + 4\omega^2}}, \\
y_6 &= \frac{1}{2}\sqrt{-4\Delta_I^2 - 4\Delta_I\Delta_R - \Delta_R^2 + \omega^2}.
\end{aligned}
$$

With these conventions, the functions $\tilde{F}_n(\omega, \Delta_R, \Delta_I, \beta, \mu)$ can be expressed as follows:

$$
\begin{aligned}
\tilde{F}_1 &= [f(\epsilon_1(y_1)) - f(\epsilon_2(y_1))]\frac{y_1\Delta_-^2}{16\left(4y_1^2 + \Delta_-^2\right)^{3/2}}\left|\frac{\sqrt{4y_1^2 + \Delta_-^2}}{y_1}\right|, \\
\tilde{F}_2 &= [f(\epsilon_1(y_2)) - f(\epsilon_3(y_2))]\left|\frac{4y_2}{\sqrt{4y_2^2 + \Delta_-^2}} - \frac{4y_2}{\sqrt{4y_2^2 + \Delta_+^2}}\right|^{-1} \times \\
&\frac{y_2^3\left(-2\Delta_R + \sqrt{4y_2^2 + \Delta_-^2} - \sqrt{4y_2^2 + \Delta_+^2}\right)}{\left(4y_2^2 + \Delta_-\left(\Delta_- - \sqrt{4y_2^2 + \Delta_-^2}\right)\right)\left(4y_2^2 + \Delta_+\left(\Delta_+ + \sqrt{4y_2^2 + \Delta_+^2}\right)\right)}, \\
\tilde{F}_3 &= [f(\epsilon_1(y_3)) - f(\epsilon_4(y_3))] \times \\
&\frac{y_3^2\sqrt{4y_3^2 + \Delta_-^2}\sqrt{4y_3^2 + \Delta_+^2}\left(-2\Delta_R + \sqrt{4y_3^2 + \Delta_-^2} + \sqrt{4y_3^2 + \Delta_+^2}\right)}{4\left(\sqrt{4y_3^2 + \Delta_-^2} + \sqrt{4y_3^2 + \Delta_+^2}\right)\prod_{i=\pm}\left(4y_3^2 + \Delta_i\left(\Delta_i - \sqrt{4y_3^2 + \Delta_i^2}\right)\right)}, \\
\tilde{F}_4 &= [f(\epsilon_2(y_4)) - f(\epsilon_3(y_4))] \times \\
&\frac{y_4^2\sqrt{4y_4^2 + \Delta_-^2}\sqrt{4y_4^2 + \Delta_+^2}\left(2\Delta_R + \sqrt{4y_4^2 + \Delta_-^2} + \sqrt{4y_4^2 + \Delta_+^2}\right)}{4\left(\sqrt{4y_4^2 + \Delta_-^2} + \sqrt{4y_4^2 + \Delta_+^2}\right)\prod_{i=\pm}\left(4y_4^2 + \Delta_i\left(\Delta_i + \sqrt{4y_4^2 + \Delta_i^2}\right)\right)}, \\
\tilde{F}_5 &= [f(\epsilon_2(y_5)) - f(\epsilon_4(y_5))]\left|\frac{4y_5}{\sqrt{4y_5^2 + \Delta_-^2}} - \frac{4y_5}{\sqrt{4y_5^2 + \Delta_+^2}}\right|^{-1} \times \\
&\frac{y_5^3\left(2\Delta_R + \sqrt{4y_5^2 + \Delta_-^2} - \sqrt{4y_5^2 + \Delta_+^2}\right)}{\left(4y_5^2 + \Delta_-\left(\Delta_- + \sqrt{4y_5^2 + \Delta_-^2}\right)\right)\left(4y_5^2 + \Delta_+\left(\Delta_+ - \sqrt{4y_5^2 + \Delta_+^2}\right)\right)},
\end{aligned}
$$

$\tilde{F}_1$	$\tilde{F}_2$	$\tilde{F}_3$	$\tilde{F}_4$	$\tilde{F}_5$	$\tilde{F}_6$
1-3, 5-7, 10, 11	6-8	1-3, 5-7, 9-11	1, 2	10-12	1, 2, 5

Table 4.1: List of $\tilde{F}_n$ functions and the regions in which they contribute, as illustrated in figure 4.4.

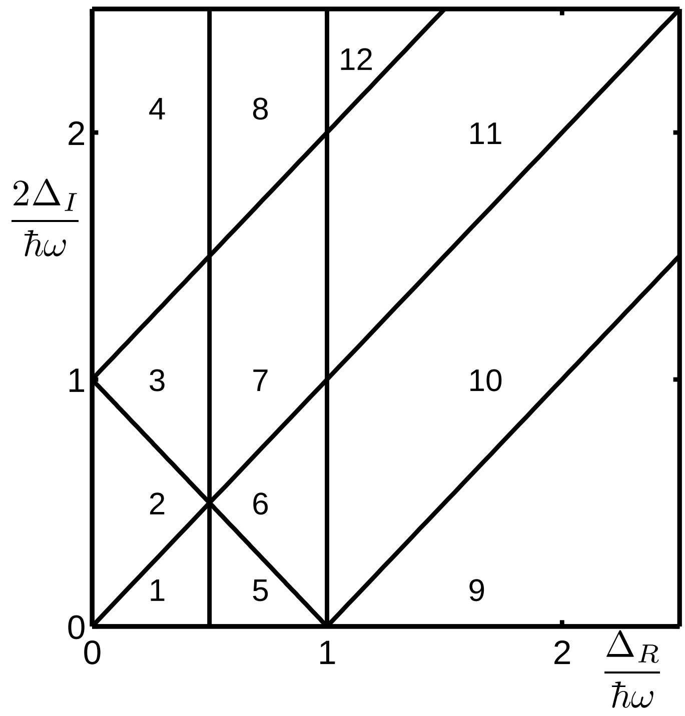

12
4
8
11
2
$\frac{2\Delta_I}{\hbar\omega}$
1
3
7
10
2
6
1
5
9
0
0
1
2
$\frac{\Delta_R}{\hbar\omega}$

Figure 4.4: Regions in the Δ_R-Δ_I-plane where the different $\tilde{F}_n$ contribute, cf. Table 4.1. There is no contribution to $\sigma(\omega)$ from region 4.

$$\tilde{F}_6 = [f(\epsilon_3(y_6)) - f(\epsilon_4(y_6))] \frac{y_6 \Delta_+^2}{16\left(4y_6^2 + \Delta_+^2\right)^{3/2}} \left| \frac{\sqrt{4y_6^2 + \Delta_+^2}}{y_6} \right| .$$

4.4 Results

We now discuss the main physical observations arising from equation (4.35). The behaviour of the conductivity is qualitatively different in the two regimes $\Delta_R > 2\Delta_I$ and $\Delta_R < 2\Delta_I$. It is well-known that the latter regime corresponds to a topological insulator phase while the former yields a conventional band insulator, with a quantum phase transition in between. For the topological insulator phase [114, 139–141], spin-polarised gapless edge states forming a helical liquid will dominate the optical conductivity when both $k_B T$

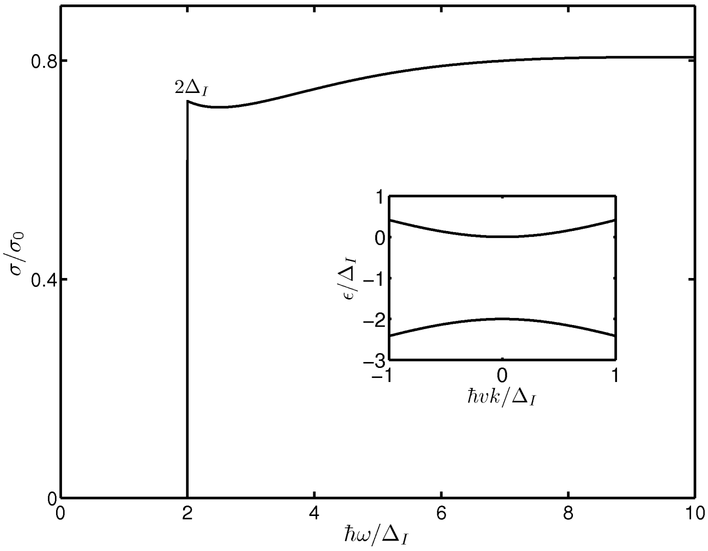

Figure 4.5: Optical conductivity at $T = 1$ K for graphene at the charge-neutrality point ($\mu = -\Delta_I$) with $\Delta_R = 0$ but finite $\Delta_I = 100\,\mu$eV. The spectral gap $2\Delta_I$ implies $\sigma(\omega) = 0$ for $\omega < 2\Delta_I$ when considering only bulk states. Inset: Low-energy part of the bandstructure.

and $\hbar\omega$ are smaller than the gap energy. In that regime, the conductivity is expected [114] to exhibit power-law behaviour analogous to that found for ordinary one-dimensional electron systems [142,143]. In what follows, we consider the frequency and temperature range such that the optical conductivity is still mostly determined by the bulk states.

The kink structure represented by the Heaviside and δ-functions depends on the relative strength of the two spin-orbit coupling terms, and this pronounced feature should allow for a clear identification of these couplings. For $\Delta_I = 0$, we find an expression analogous to the conductivity of bilayer graphene [144], where the McClure interlayer hopping constant is replaced by Δ_R. We give the analytical expression for completeness, using $\hbar v_F k = \epsilon$:

$$\begin{aligned}\frac{\sigma}{\sigma_0} &= \frac{\pi}{2}\delta\left(\hbar\omega-\Delta_R\right)\int_0^\infty d\epsilon\frac{\epsilon\Delta_R}{4\epsilon^2+\Delta_R^2} \\ &\quad\times\left[g\left(\frac{1}{2}\left(\Delta_R+\sqrt{4\epsilon^2+\Delta_R^2}\right)\right)+g\left(\frac{1}{2}\left(\Delta_R-\sqrt{4\epsilon^2+\Delta_R^2}\right)\right)\right] \qquad (4.36)\\ &\quad+\frac{\pi}{8}g\left(\frac{\hbar\omega}{2}\right)\left[\frac{\hbar\omega+2\Delta_R}{\hbar\omega+\Delta_R}+\frac{\hbar\omega-2\Delta_R}{\hbar\omega-\Delta_R}\Theta(\hbar\omega-2\Delta_R)\right] \\ &\quad+\frac{\pi}{8}\frac{\Delta_R^2}{(\hbar\omega)^2}\left[g\left(\frac{\hbar\omega+\Delta_R}{2}\right)+g\left(\frac{\hbar\omega-\Delta_R}{2}\right)\right]\Theta(\hbar\omega-\Delta_R),\end{aligned}$$

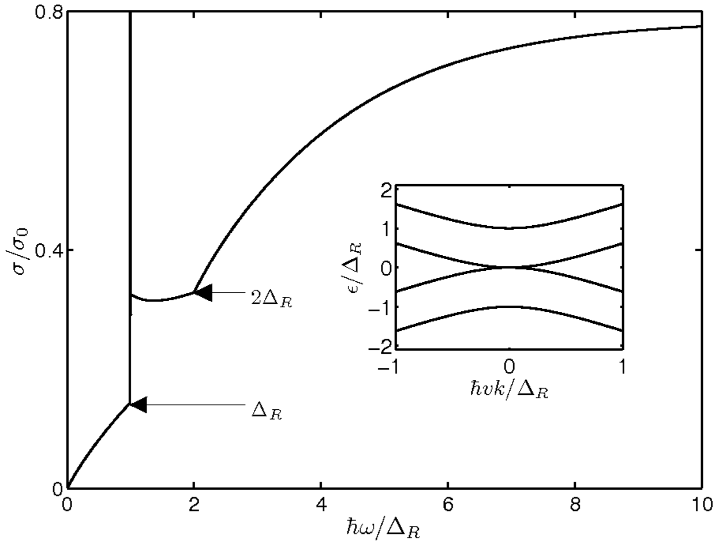

Figure 4.6: Same quantity plotted and parameters used as in figure 4.5, except that $\Delta_I = 0$ and $\Delta_R = 100\,\mu\text{eV}$ and $\mu = 0$. Kinks arise when new transitions between different bands become possible at certain critical values of ω (see inset).

where we define the function

$$g(\varepsilon) = \frac{\sinh(\varepsilon\beta)}{\cosh(\mu\beta) + \cosh(\varepsilon\beta)}. \tag{4.37}$$

For $\Delta_R = \Delta_I = 0$, we recover the optical conductivity of clean graphene (4.25) with a spin-degenerate linear dispersion [126, 127]. For large frequencies, ω, the conductivity approaches the well-known universal value $e^2/4\hbar$. We find that the high-frequency behaviour is independent of the spin-orbit coupling, and for all investigated cases we find the same asymptotic behaviour.

The optical conductivity for various parameter regimes in the $\Delta_R - \Delta_I$ plane is shown next in a series of figures. In particular, in figure 4.5 we set $\Delta_R = 0$, in figure 4.6 we have $\Delta_I = 0$, in figure 4.7 both couplings are finite but in the regime $\Delta_R > 2\Delta_I$, and in figure 4.8 we are at the special point $\Delta_R = 2\Delta_I$. Furthermore, figure 4.9 shows the regime $\Delta_I > 2\Delta_R$. To be specific, all these figures are for $T = 1$ K (where $k_BT \simeq 100\mu\text{eV}$ and $k_BT/h \approx 24$ GHz). Finally, figure 4.10 displays the effects of thermal smearing.

For $\Delta_R = 0$ but finite Δ_I, we find a gapped but still doubly (spin-)degenerate dispersion. The gap leads to vanishing conductivity for $\hbar\omega < \Delta_I$, see figure 4.5. Although the chosen value is probably unphysically large, similar figures are obtained for smaller Δ_I.

For $\Delta_I = 0$ but finite Δ_R, on the other hand, the band structure mimics that of bilayer graphene but with a gap smaller by up to 4 orders of magnitude [111, 144]. The optical conductivity for this case is shown in figure 4.6 and has the same functional form as the

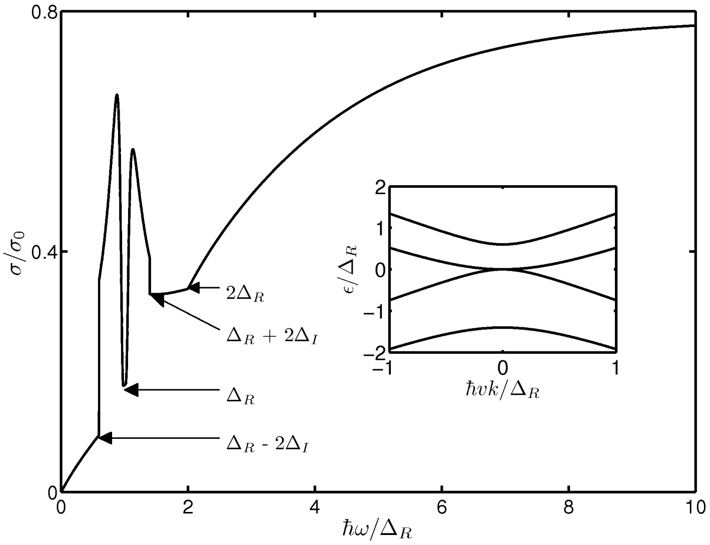

Figure 4.7: Same quantity plotted and parameters used as in figure 4.5, except that $\Delta_R = 100\,\mu$eV and $\Delta_I = 0.2\Delta_R$, thus realizing the case $2\Delta_I < \Delta_R$. We set $\mu = 0$ to maintain charge neutrality. More kinks appear as the bands are less symmetric than for the cases shown in figures 4.5 and 4.6.

conductivity for bilayer graphene [129]. In particular, it has a δ-peak at $\hbar\omega = \Delta_R$ and a kink at $\hbar\omega = 2\Delta_R$. The gap opened by the intrinsic spin-orbit coupling, see figure 4.5, is closed by the Rashba spin-orbit coupling, see insets of figures 4.7 to 4.9.

For $2\Delta_I < \Delta_R$, we observe a splitting and widening of the δ-peak at Δ_R, while the kink at $2\Delta_R$ stays at the same position. In addition, we observe kinks at $\Delta_R \pm 2\Delta_I$, see figure 4.7.

At the quantum phase transition point $2\Delta_I = \Delta_R$, the dispersion exhibits a crossing of two massless branches with a massive branch, see inset of figure 4.8. As a consequence, certain sharp features exhibited by the optical conductivity in other cases disappear .

For $2\Delta_I > \Delta_R$, see figure 4.9, the conductivity shows kinks at $\hbar\omega = \Delta_R$, at $\hbar\omega = 2\Delta_R$, and at $2\Delta_I \pm \Delta_R$.

We have chosen to show a very wide range of spin-orbit coupling parameters Δ_R and Δ_I in these figures. Previous estimates for these parameters [114–116, 134–136] range from 0.5 μeV to 100 μeV for Δ_I, and 0.04 μeV to 23 μeV for Δ_R. The Rashba coupling is expected to be linear in the electric back-gate field, with proportionality constant 10 μeV m/V [136], allowing for an experimental lever to sweep through a wide parameter range. On the experimental side, the picture is currently mixed. One recent experimental study finds $\Delta_R = 370\,\mu$eV ($210\,\mu$eV) for electrons (holes) in carbon nanotubes [122]. A much larger value $\Delta_R = 13$ meV has been reported for graphene sheets fabricated on a nickel surface [123, 124].

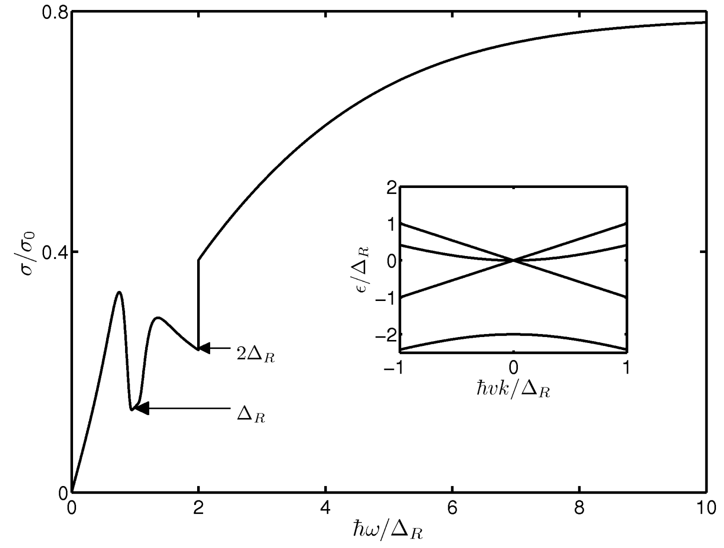

Figure 4.8: Same as figure 4.5 but for the special case $2\Delta_I = \Delta_R$ with $\Delta_R = 100\,\mu$eV, setting $\mu = 0$ to ensure charge neutrality. Inset: The bandstructure shows that three bands cross at $k = 0$, and hence some of the kinks in $\sigma(\omega)$ disappear.

For low temperatures (e.g., at $T = 1$ K in the above figures), the spin-orbit couplings can be distinguished by the different peak structures appearing in the optical conductivity. Increasing the temperature leads to thermal smearing of those features, as illustrated in figure 4.10. However, the characteristic spin-orbit coupling-induced peak and kink features should still be visible in the optical conductivity up to $T \approx 10$K, albeit with a smaller magnitude.

4.5 Discussion

We have calculated the optical conductivity for a graphene monolayer including the two most relevant spin-orbit couplings, namely the intrinsic atomic contribution Δ_I and the curvature and electric-field-induced Rashba term Δ_R. Our result for the optical conductivity, which we presented for finite temperature and chemical potential at the charge neutrality point, shows kinks and/or peaks at frequencies corresponding to Δ_R, $2\Delta_R$, and $|(\Delta_R \pm 2\Delta_I)|$. Measuring the optical conductivity in a frequency range covering these energy scales can be expected to yield detailed insights into the nature of spin-orbit interactions in graphene.

We did not analyse disorder effects but expect all sharp features to broaden since the δ-functions in equation (4.33) effectively become Lorentzian peaks. We also did not consider the effect of electron-electron interactions. While renormalisation group studies indicate that weak unscreened interactions are marginally irrelevant [108], interactions may still play an important role. For instance, the authors of [145] consider interaction effects on the optical properties of doped graphene without spin-orbit coupling. Interactions cause inter-band (optical) and intra-band (Drude) transitions and thus a finite DC conductivity. Reference [131] studies the optical conductivity with an interaction induced gap and weak impurity scattering. We expect that the peak and kink structures arising from the spin-orbit couplings survive however, because the relevant contributions are additive. We only took the zeroth order in $\vec{k}$ of the spin-orbit coupling into account. More detailed calculations [117] show that there are higher order terms. These cause the Dirac cones near the K points to split into four cones. A similar picture holds for bilayer graphene [146]. In both cases the spin-orbit couplings split the bands, which in turn is expected to leave a distinct imprint on the optical conductivity.

Recent experimental studies suggest that an optical measurement of the conductivity in the energy range relevant for spin-orbit coupling should be possible. Fei *et al.* [147] have measured the optical conductivity from $\hbar\omega = 1.54$ eV up to 4.13 eV. Slightly lower energies (0.2 eV to 1.2 eV) were reached in reference [148]. We suggest to perform low-temperature experiments at microwave frequencies, with energies ranging from several μeV to a few meV, for both single and double layer graphene, to determine Δ_I as well as Δ_R.

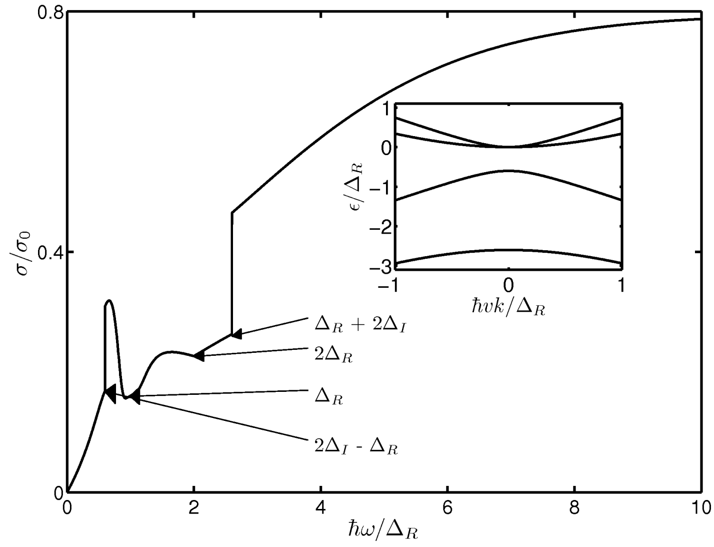

Figure 4.9: Same as figure 4.5, except that $\Delta_I = 0.8\Delta_R$ with $\Delta_R = 100\,\mu$eV, thus realizing the case $2\Delta_I > \Delta_R$. Charge neutrality is maintained by setting $\mu = (\Delta_R - 2\Delta_I)/2$.

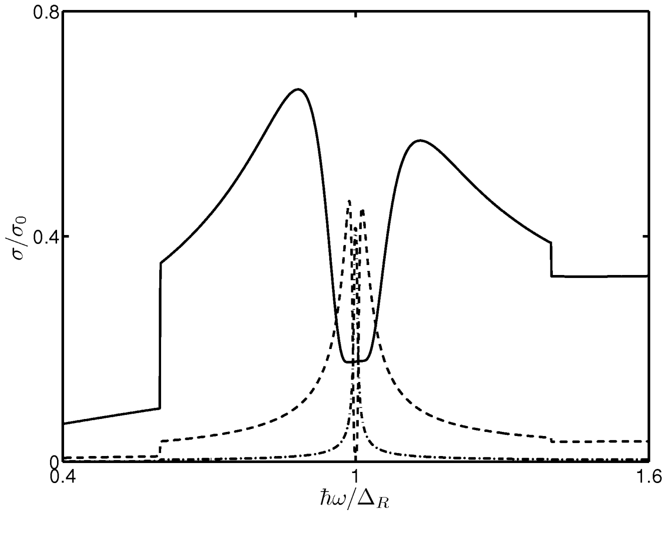

Figure 4.10: Same as figure 4.7, focusing on the region $0.4 < \hbar\omega/\Delta_R < 1.6$. The solid curve is for $T = 1$ K, the dashed curve for $T = 10$ K, and the dot-dashed one for $T = 100$ K. The distinct kinks are thermally smeared and suppressed at elevated temperatures, but remain visible up to $T \approx 10$ K.

Chapter 5

Summary and Conclusions

In this thesis I examined the spin and spin transport properties of three different systems relevant for future spintronic applications. I first focused on the combined effect of Rashba spin-orbit coupling and electron-electron interaction in quantum wires. Then I considered a spin valve, where the middle nonmagnetic layer is formed by an organic conducting compound. In the last chapter I investigated the effect of spin-orbit coupling on the optical conductivity in graphene. In the following the main conclusions are summarised.

In chapter 2 I derived a low-energy Hamiltonian for a homogeneous one dimensional quantum wire. I included electron-electron interactions as well as Rashba spin-orbit coupling. Using the simplest model, i.e., no magnetic field, no disorder, and only a single channel, I first analysed the possible interaction processes through the second order RG flow-equation. I found that the backscattering, which would open a spin gap, is irrelevant in a RG sense, and were able to find the renormalised coupling constants for the low energy theory. Having found the new renormalised couplings I constructed a low-energy modified Luttinger liquid theory. In this new theory the spin-orbit coupling breaks the spin charge separation. Our theory is analytically solvable and opens up the possibility to compute all physical properties of the system. In this framework I computed the RKKY range function, which describes the interaction of two magnetic impurities. In a quantum wire without spin-orbit coupling or electron-electron interaction the magnetic coupling strength spatially oscillates with frequency of $2k_F$, and decays as $|x|^{-1}$ for long distances. For a noninteracting wire with spin-orbit coupling several spatial oscillation periods are found, reflecting the fact that there are now two Fermi points $k_F^{(A/B)}$, but the asymptotic behaviour $\propto |x|^{-1}$ is not changed. Interactions change this picture. I still find several oscillating frequencies, which now do not decay at the same rate. One frequency dominates at long distances due to the slowest decay with an exponent $\eta_B < 1$. This exponent depends on the electron-electron interaction strength as well as the tunable Rashba coupling strength. This opens the possibility to tune the long range decay and the dominating frequency of the RKKY interaction function. An external perpendicular field, which causes the spin-orbit interaction, makes it possible to alter the magnetic properties of the quantum wire. Since I have set up an exactly solvable model for the interacting Rashba wire, all correlation functions are known and it should be easy to extract more physical properties of the wire from this theory. Thus, our formulation holds promise for future examination of the combined effect of electron-electron interaction and spin-orbit coupling on the spin transport properties of quantum wires. It would be interesting to model a ferromagnetic quantum-wire contact and investigate how the spin injection is influenced by the combined effect of spin-orbit coupling and electron-electron interactions. This would allow to examine the spin accumulation in the wire.

In chapter 3 I discussed a GMR-like spin valve, in which a conducting polymer is sandwiched between differently magnetised ferromagnetic layers. Conducting polymers are semiconductors, but in contrast to inorganic semiconductors, the charge and spin transport is not due to holes and electrons, but more complicated excitations with non-standard spin charge relations. There are singly charged and spinful polarons and doubly charged and spinless bipolarons. I used network theory and a diffusive model to obtain the spin dependent transport properties of the organic polymer sandwiched between two arbitrarily magnetised ferromagnets. I took both species of charge carriers, polarons and bipolarons, into account and introduced the transition rates k and b to describe the process of two polarons combining into one bipolaron and vice versa. Fortunately, the transition rates k and b are small enough to justify a perturbative approach. I found the spin-dependent current to be independent of the scattering rates between the two species, leaving the current unchanged from the situation without bipolarons. In turn I found the bipolaron density to be sensitive to the magnetisation angle between the magnetic contacts. This effect is small, but it may still offer the possibility to use optical measurements of the bipolaron density to probe the spin polarisation, thus giving an additional experimental tool to detect spin accumulation in organic compounds. Future work could include the study of disordered bundles of highly conducting ploymers in a spin-valve. The heterogeneous disorder in polymer bundles has proven to be the main cause for the semiconductor-metal crossover behaviour of conducting polymers. Taking disorder into account would allow to model the spin-transport more accurately.

In chapter 4 I explored the optical properties of single-layer graphene. I used the pseudo-relativistic low-energy description of graphene. On top of that, I included the known spin-orbit coupling terms, intrinsic and Rashba terms. The existence of these can be inferred from group-theoretical arguments, tight-binding, or functional density calculations. The actual values of their respective strength are, however, subject to recent debate. I theoretically analysed the optical conductivity of graphene in the Kubo formalism. Since the Rashba term is gate tunable, I computed the optical conductivity for various parameter regimes that are experimentally accessible via an externally applied electric field. The high energy behaviour remains unchanged, and the optical conductivity asymptotically reaches the well-known universal value of $e^2/4\hbar$. At energies comparable to the gap opened by the spin-orbit interaction, I find distinct kinks and peaks that are attributed to the presence of spin-orbit coupling. I propose measuring the microwave optical conductivity in single-layer graphene as a way to determine the values of the intrinsic as well as the Rashba spin-orbit couplings. Further studies could contain the inclusion of higher order terms in the spin-orbit coupling such as the split Dirac-cone or trigonal warping, and the extension of our calculation to double-layer graphene. To match theoretical results in experiments it might be necessary to go beyond the effective relativistic model and do numerical first principle calculations, such as density functional methods or random phase approximations.

Results obtained in this thesis are published in [21, 24, 26].

Appendix A

Second order RG equations

In this appendix we demonstrate the derivation of the second order RG equations in a perturbative scheme. The partition function, depending on the couplings $\{g_i\}$ and the cutoff Λ or a, can be expressed in the functional integral formalism as

$$Z\left[g_i,\Lambda\right]=\int\mathcal{D}\psi\ \exp\left(-S\left[\psi\right]\right), \tag{A.1}$$

where $\mathcal{D}\psi$ stands symbolically for the integration over all four fermionic fields and the action S is defined as

$$S[\psi]=\int d\tau H_0+H_I, \tag{A.2}$$

thus it can be split into $S=S_0+S_I$, the kinetic and the interaction part. The interaction part reads

$$S_I=\sum_j g_j\int dx\int d\tau\ \ O_j(x). \tag{A.3}$$

With this we can cast equation (A.1) as

$$Z\left[g_i,\Lambda\right]=\int\mathcal{D}\psi\ e^{-S_0[\psi]}e^{-S_I[\psi]}=\left\langle e^{-S_I[\psi]}\right\rangle_{S_0}Z_0. \tag{A.4}$$

The last equality in equation (A.4) indicates that we can express the partition function of the interacting system in terms of a noninteracting expectation value, i.e., with respect to S_0. We assume that the initial coupling constants found in equation (2.37) are small enough for perturbative treatment. We then expand the expectation value in equation (A.4) up to second order to find the *one loop* RG equations

$$\begin{aligned}\frac{Z\left[g_i,\Lambda\right]}{Z_0} &= \langle 1\rangle-\sum_j g_j\left\langle\int dx\int d\tau\ \ O_j(x,\tau)\right\rangle\\ &\quad+\frac{1}{2}\sum_{ij}g_ig_j\left\langle\int dx_1d\tau_1dx_2d\tau_2\ \ O_j(x_1,\tau_1)O_i(x_2,\tau_2)\right\rangle+\mathcal{O}(g_i^3),\end{aligned} \tag{A.5}$$

where the second order integral is only evaluated for $|x_1 - x_2| > a$. We iteratively rescale the momentum cutoff $\Lambda \to \Lambda' = \Lambda e^{-l}$, in real space this translates to $a' = ae^l$, with $l = \log(a'/a) = \log(\Lambda/\Lambda')$. We integrate out the degrees of freedom between the two cutoffs. Since the cutoff is arbitrary, the physical properties of the system must not depend on it. Therefore, we need to define a new set of coupling constants g_i', for the new cutoff Λ', such that the partition function is unchanged

$$Z\left[g_i, \Lambda\right] = Z\left[g_i', \Lambda'\right]. \tag{A.6}$$

We start with the first order term. Here we need to find the scaling dimension h_i of the operators O_i which is formally defined via

$$O_i(sx, s\tau) = s^{-h_i} O_i(x, \tau). \tag{A.7}$$

It is now possible to derive the first order RG equation from this. Since we set $\hbar = 1$ the action is a dimensionless quantity. The O_i's have dimension L^{-h_i} (L=length) and the integral $\int dx \int v d\tau$ has dimension L^2. Thus, g_i/v will have dimension L^{2-h_i}. The new coupling constants will then be defined as $\tilde{g}_i = g_i a^{2-h_i}$. To keep the partition function invariant under RG we need to ensure that $S_I[g_i, a] = S_I[g_i', a']$. It is now easy to see that from an infinitesimal RG step we find a differential equation for the RG flow as

$$\frac{dg_i(l)}{dl} = (2 - h_i) g_i(l). \tag{A.8}$$

Let us introduce the concept of relevant ($h_i < 2$), irrelevant ($h_i > 2$) and marginal ($h_i = 2$) operators, which grow, vanish, or stay the same under RG flow ($l \to \infty$). Relevant operators we need to keep, irrelevant operators we can forget, and for the marginal operators we have to go to the next order in the expansion (A.5) to find out how they behave. To find the scaling dimension h_i we use Wick's theorem and the two point correlation functions for the fermionic operators

$$\left\langle \psi(x_1) \psi^\dagger(x_2) \right\rangle \propto \frac{1}{|x_1 - x_2|}. \tag{A.9}$$

Consequently, the expectation value for our interaction operators scales as

$$\langle O_i(sx) \rangle = s^{-2} \langle O_i(x) \rangle, \tag{A.10}$$

and thus have scaling dimension $h_i = 2$. Therefore, all considered operators are marginal and we need to go to the next order for all couplings.

To find the second order contribution for the RG equation we use a technique called *operator product expansion* (OPE). It essentially states that marginal operators can be decomposed as

$$O_i(x_1)O_j(x_2) \simeq \sum_k C^k_{ij}(x_{12})O_k(X). \tag{A.11}$$

It is implicitly assumed here that the operators, that are produced in this process are all contained in a closed set $\{O_k\}$. It is also said that the interaction operators form a closed algebra under OPE. We define the important quantity

$$c^k_{ij} = \frac{2\pi}{l}\int\limits_a^{a'} dx_{12}\int\limits_{-\infty}^{\infty} d\tau C^k_{ij}(x_{12}). \tag{A.12}$$

With this we consider the partition function again, and find the second order correction to the first order expansion in the following way

$$\begin{aligned}\frac{Z\left[g_i', \Lambda\right]}{Z_0} \quad = \quad & \langle 1\rangle - \sum_j g_j' \left\langle \int dx \int d\tau \;\; O_j(x,\tau)\right\rangle \\ & + \frac{1}{2}\sum_{ij} g_i' g_j' \left\langle \int dx_1 d\tau_1 dx_2 d\tau_2 \;\; O_j(x_1,\tau_1)O_i(x_2,\tau_2)\Theta(|x_{12}| > a)\right\rangle \\ & - \frac{1}{2}\sum_{ij} g_i' g_j' \left\langle \int dx_1 d\tau_1 dx_2 d\tau_2 \;\; O_j(x_1,\tau_1)O_i(x_2,\tau_2)\Theta(a' > |x_{12}| > a)\right\rangle \\ & + \mathcal{O}(g_i^3),\end{aligned} \tag{A.13}$$

where in the third line we expand the operator product, and find

$$g_i' g_j' \int dx_1 d\tau_1 dx_2 d\tau_2 \;\; O_j(x_1,\tau_1)O_i(x_2,\tau_2)\Theta(a' > |x_{12}| > a) \simeq \sum_k g_i' g_j' \int dX O_k(X)\frac{c^k_{ij} l}{2\pi}. \tag{A.14}$$

Thus we can express the partition function as

$$\frac{Z\left[g_i, \Lambda\right]}{Z_0} = \langle 1\rangle - \sum_i \left\langle \int dx \int d\tau \left(g_i' + \frac{1}{2}\sum_{jk}\frac{g_j' g_k'}{2\pi} c^i_{jk} l\right) \;\; O_i(x,\tau)\right\rangle + \mathcal{O}(g^2). \tag{A.15}$$

The second order RG equations for the marginal operators read

$$\frac{dg_i}{dl} = \frac{1}{4\pi}\sum_{jk} c^i_{jk} g_j g_k. \tag{A.16}$$

The task we are left with is to find the c^i_{jk}. To do so we will again use Wick's theorem.

Let $A(x_1)$ and $B(x_2)$ be one of the four fermion operators defined in equation (2.38) to (2.42). Wick's theorem (see e.g. [149]) then states that

$$A(x_1)B(x_2) = \sum_{n=0}^{4} \left[A(x_1)B(x_2)\right]_n , \tag{A.17}$$

where $\left[A(x_1)B(x_2)\right]_n$ is the sum of all terms with n contractions, with a contraction defined as

$$\begin{aligned} \underbracket{\psi^\dagger_{\nu r}(x_1)\psi_{\nu' r'}}(x_2) &= \left\langle T_\tau \psi^\dagger_{\nu r}(x_1)\psi_{\nu' r'}(x_2)\right\rangle \\ &= \delta_{\nu\nu'}\delta_{rr'}\frac{ir}{2\pi}\frac{1}{x_{12} + ir\mathrm{sgn}(\tau_{12})(v_\nu|\tau_{12}| + a)}. \end{aligned} \tag{A.18}$$

Furthermore, we know that contractions within already normal ordered blocks are zero. In our discussion only terms containing two contractions contribute to the RG equations. The other terms are either irrelevant, disconnected diagrams, or can be absorbed by a shift in the chemical potential. So we only need to look at the following integral

$$\int_{a}^{a'} dx_{12} \int_{-\infty}^{\infty} d\tau \left[A(x_1)B(x_2)\right]_2 . \tag{A.19}$$

The integral over the two contractions can then be computed using Cauchy's theorem

$$\int_{\alpha}^{\alpha'} dx_{12} \int_{-\infty}^{\infty} d\tau \frac{ir}{2\pi}\frac{ir'}{2\pi}\frac{1}{(x + irv_\nu\tau)(x + ir'v_{\nu'}\tau)} = \delta_{rr'}\frac{1}{2\pi}\frac{2l}{v_\nu + v_{\nu'}}. \tag{A.20}$$

With this it is straight forward to find the OPE coefficient c^i_{jk}. Equation (A.16) then allows us to cast the one loop RG equations as

$$\frac{dg_{4\|\nu}}{dl} = \frac{dg_{4\perp}}{dl} = 0, \tag{A.21}$$

$$\frac{1}{\pi v_\nu}\frac{dg_{2\|\nu}}{dl} = -\frac{\gamma}{2\pi^2 v_F^2} g_f^2, \tag{A.22}$$

$$\frac{1}{\pi v_F}\frac{dg_{2\perp}}{dl} = \frac{1}{2\pi^2 v_F^2} g_f^2, \tag{A.23}$$

$$\frac{1}{\pi v_F}\frac{dg_f}{dl} = -\frac{1}{2\pi^2 v_F^2} g_f \left(\frac{g_{2\|A}}{2\pi v_A} + \frac{g_{2\|B}}{2\pi v_B} - \frac{g_{2\perp}}{\pi v_F}\right), \tag{A.24}$$

with the dimensionless constant

$$\gamma = \frac{v_F^2}{v_A v_B} = \frac{1}{1-\delta^2} \geq 1. \tag{A.25}$$

It can be seen that the g_4 terms do not contribute to the one loop RG equations and we can use the initial values defined in (2.37). Following [64, 65], we find the following integrals of motion, i.e., quantities that are invariant under RG

$$I_1 = \frac{g_{2\|A}}{\pi v_A} - \frac{g_{2\|B}}{\pi v_B}, \tag{A.26}$$

$$I_2 = \frac{1}{\gamma}\left(\frac{g_{2\|A}}{\pi v_A} + \frac{g_{2\|B}}{\pi v_B}\right) - \frac{2g_{2\perp}}{\pi v_F}, \tag{A.27}$$

$$I_3 = \left(\frac{g_{2\|A}}{2\pi v_A} + \frac{g_{2\|B}}{2\pi v_B} - \frac{g_{2\perp}}{\pi v_F}\right)^2 - \frac{1+\gamma}{2}\frac{g_f^2}{\pi^2 v_F^2}. \tag{A.28}$$

It is easy to see that $dI_k/dl = 0$. With the following rescaled constants

$$\bar{g}_2 = \frac{g_{2\|A}}{2\pi v_A} + \frac{g_{2\|B}}{2\pi v_B} - \frac{g_{2\perp}}{\pi v_F}, \tag{A.29}$$

$$\bar{g}_f = \sqrt{\frac{1+\gamma}{2}\frac{g_f^2}{\pi^2 v_F^2}}, \tag{A.30}$$

we can reduce the RG equations to only two equations with only two coupling constants, the two-dimensional Kosterlitz-Thouless RG flow equations,

$$\frac{d\bar{g}_2}{dl} = -\bar{g}_f^2, \quad \frac{d\bar{g}_f}{dl} = -\bar{g}_f \bar{g}_2. \tag{A.31}$$

Following [46, 47], we can easily solve these equations. For all initial conditions with $|\bar{g}_f(0)| \leq \bar{g}_2(0)$ we find the solution to be

$$\bar{g}_2(l) = \frac{A}{\tanh\left[Al + \operatorname{atanh}\left(\frac{A}{\bar{g}_2(0)}\right)\right]}, \tag{A.32}$$

$$\bar{g}_f(l) = \frac{A}{\sinh\left[Al + \operatorname{atanh}\left(\frac{A}{\bar{g}_2(0)}\right)\right]}, \tag{A.33}$$

where $A^2 = I_3$ and the initial values can be read from (2.37)

$$\begin{aligned} \bar{g}_2(l=0) &= \frac{(\gamma-1)W_0 + W_1}{\pi v_F}, \\ \bar{g}_f(l=0) &= \sqrt{\frac{1+\gamma}{2}\frac{W_1}{\pi v_F}}. \end{aligned} \tag{A.34}$$

Equations (2.35) and (2.47) imply with $\gamma \simeq 1 + \delta^2$ the condition

$$\tilde{V}(0) \geq \frac{1}{4}\cos^2(\theta_A - \theta_B)\ \tilde{V}\left(k_F^{(A)} + k_F^{(B)}\right), \tag{A.35}$$

which is satisfied for all physically relevant repulsive e-e interaction potentials, thus the initial conditions hold $|\bar{g}_f(0)| \leq \bar{g}_2(0)$.

Appendix B

Bosonisation and Luttinger liquids

In this appendix we want to explain the concept of bosonisation and derive the Tomonaga Luttinger model in detail and explain how the expectation values are computed.

Let us start with illustrating equation (2.52) for the spinless case

$$\psi_\nu(x) = \frac{\eta_\nu}{\sqrt{2\pi a}} e^{i\nu\phi_\nu(x)}. \tag{B.1}$$

To prove this mapping between fermions and bosons the following bosonic operator identity [150] is needed:

$$e^A e^B =: e^{A+B} : e^{\langle AB+(A^2+B^2)/2\rangle}, \tag{B.2}$$

where $\langle\dots\rangle$ is the expectation value in the bosonic vacuum, and $:\cdots:$ is the normal ordering. In a normal ordered product the destruction operators are put on the right and creation operators on the left. Here A, B are just linear combinations of bosonic creation and destruction operators

$$\begin{aligned} A &= \alpha_1 a^\dagger + \alpha_2 a, &\text{(B.3)}\\ B &= \beta_1 a^\dagger + \beta_2 a. &\text{(B.4)}\end{aligned}$$

Hence, $[A, B]$ commutes with A or B. We use the Baker-Hausdorff identity

$$e^{A+B} = e^A e^B e^{-\frac{1}{2}[A,B]}, \tag{B.5}$$

to decompose the exponential. After that, we use the commutation rules to normal order the product and get

$$\begin{aligned} e^A e^B &= e^{\alpha_1 a^\dagger} e^{\beta_1 a^\dagger} e^{\alpha_2 a} e^{\beta_2 a} e^{\beta_1\alpha_2+\frac{1}{2}(\alpha_1\alpha_2+\beta_1\beta_2)} &\text{(B.6)}\\ &= : e^{A+B} : e^{\langle AB+(A^2+B^2)/2\rangle}. &\text{(B.7)}\end{aligned}$$

To prove that the bosonic representation really is equivalent to the fermionic one we need to verify that we can reproduce the commutation relations and the correlation functions.

Let us start with the commutation relations. To prove that equation (B.1) reproduces

$$\left\{\psi_\nu(x), \psi^\dagger_{\nu'}(x')\right\} = \delta_{\nu\nu'}\delta(x-x'), \tag{B.8}$$

using equation (B.2) and the bosonic correlators we first prove the above identity for right movers. The Green's function in the bosonic picture reads (see e.g., [47])

$$G_R(x-x') = \left\langle \phi_R(x)\phi_R(x')\right\rangle - \left\langle \phi_R(x)^2\right\rangle = \log\left(\frac{ia}{(x-x')+ia}\right), \tag{B.9}$$

we obtain

$$\begin{aligned}
\left\{\psi_R(x), \psi^\dagger_R(x')\right\} &= \lim_{a\to 0}\frac{1}{2\pi a}\left[\eta_R e^{i\phi_R(x)}\eta_R e^{-i\phi_R(x')} + \eta_R e^{-i\phi_R(x')}\eta_R e^{i\phi_R(x)}\right] \\
&= \lim_{a\to 0}\frac{1}{2\pi a} : e^{i(\phi_R(x)-\phi_R(x')} : \left[e^{G_R(x,x')} + e^{G_R(x',x)}\right] \\
&= \lim_{a\to 0}\frac{1}{2\pi a} : e^{i(\phi_R(x)-\phi_R(x')} : \left[\frac{ia}{(x-x')+ia} - \frac{ia}{(x-x')-ia}\right] \\
&= \lim_{a\to 0}\frac{ia}{2\pi a} : e^{i(\phi_R(x)-\phi_R(x')} : \left[-2i\pi\delta(x-x')\right] \\
&= \delta(x-x').
\end{aligned} \tag{B.10}$$

The computation for the left movers is analogous. What is left to show is $\{\psi_R, \psi^\dagger_L\} = 0$. Since left and right-moving bosons commute, this anti-commutation relation is provided by the Klein factors:

$$\begin{aligned}
\{\psi_R, \psi^\dagger_L\} &= \frac{1}{2\pi a}\left[\eta_R e^{i\phi_R(x)}\eta_L e^{i\phi_L(x')} + \eta_L e^{i\phi_L(x')}\eta_R e^{i\phi_R(x)}\right] \\
&= \frac{1}{2\pi a}\left[\eta_R\eta_L + \eta_L\eta_R\right] e^{i\phi_R(x)} e^{i\phi_L(x')} \\
&= 0.
\end{aligned} \tag{B.11}$$

Therefore, the anti-commutation relations (B.8) are fulfilled in the bosonic picture.

Now we show that equation (B.1) also leads to the correct correlation functions. In the fermionic picture the right mover correlation function is

$$\begin{aligned}\left\langle\psi_R^\dagger(x)\psi_R(x')\right\rangle &= \frac{1}{2\pi}\int\limits_{-\infty}^{\infty} e^{-ik(x-x')}\left\langle c_R^\dagger(k)c_R(k)\right\rangle \\ &= \frac{1}{2\pi}\int\limits_{-\infty}^{0} e^{[a-i(x-x')]k} \\ &= \frac{1}{2\pi}\frac{1}{a-i(x-x')}. \end{aligned} \tag{B.12}$$

In the bosonic version using (B.2) we find

$$\begin{aligned}\left\langle\psi_R^\dagger(x)\psi_R(x')\right\rangle &= \frac{1}{2\pi a}\left\langle e^{-i\phi_R(x)}e^{i\phi_R(x')}\right\rangle \\ &= \frac{1}{2\pi a}\left\langle : e^{-i(\phi_R(x)-\phi_R(x'))} :\right\rangle e^{G_R(x,x')} \\ &= \frac{1}{2\pi}\frac{1}{a-i(x-x')}. \end{aligned} \tag{B.13}$$

Note that by definition in the expectation value of the normal ordered exponential, only the unity fails to annihilate the vacuum; thus $\left\langle : e^{i\phi} :\right\rangle = 1$. The computation for the left movers is analogous.

Finally, using (B.1) we can also reproduce the bosonic Hamiltonian (2.51) starting from the fermionic Hamiltonian, equation (2.50). In order to prove that we need to know the density and the kinetic energy operators in the bosonic representation. We restrict this analysis to the spinless case for simplicity. The density of right movers is given by

$$\begin{aligned}\lim_{x'\to x}\psi_R^\dagger(x')\psi_R(x) &= \lim_{x'\to x}\frac{1}{2\pi a}e^{-i\phi_R(x')}e^{i\phi_R(x)} \\ &= \lim_{x'\to x}\frac{1}{2\pi a} : e^{-i\phi_R(x')+i\phi_R(x)} : e^{G_R(x'-x)} \\ &= \lim_{x'\to x}\frac{1}{2\pi a} : 1 - i(x'-x)\partial_x\phi_R(x'-x) + O((x'-x)^2) : \frac{ia}{x'-x+ia} \\ &= \lim_{x'\to x}\frac{i}{2\pi(x'-x+ia)} + : \frac{1}{2\pi}\partial_x\phi_R + O(x'-x) : \quad . \end{aligned} \tag{B.14}$$

Notice that the exponential is expanded within the normal ordering because the normal ordered quantity is free of divergences, and one can treat the fields as if they were commuting. The last step is allowed since any distance x, even in the limit $x \to 0$, has to be seen as larger than a. The first term is then divergent. This merely reflects the infinite number of right mover states in the ground state. Defining the normal ordered charge density by removing the vacuum expectation value we find

$$: \psi_R^\dagger(x)\psi_R(x) := \frac{1}{2\pi}\partial_x\phi_R(x). \tag{B.15}$$

This regularisation procedure is called point-splitting regularisation. For the left movers one obtains the same result.

Now consider the kinetic part in the Hamiltonian. For the right movers we find

$$\begin{aligned}\lim_{x'\to x}\psi_R^\dagger(x')(-i\partial_x\psi_R(x)) &= \lim_{x'\to x}(-i\partial_x)(\psi_R^\dagger(x')\psi_R(x))\\ &= \frac{1}{2\pi a}(-i\partial_x)\left[: e^{-i(\phi_R(x')-\phi_R(x)}:e^{G_R(x',x)}\right]. \qquad \text{(B.16)}\end{aligned}$$

In the computation of the density it was enough to expand the exponential only up to the first order in $x'-x$, in this case though, it is necessary to go up to second order due to the derivative and we find

$$\begin{aligned}&: e^{-i(\phi_R(x')-\phi_R(x))} :=\\ &: 1+(x'-x)\left(-i\partial_x\phi_R(x-x')\right)+\frac{1}{2}(x'-x)^2\left(-i\partial_x^2\phi_R(x)-(\partial_x\phi_R(x))^2\right)+O((x'-x)^3):.\end{aligned}$$

Inserting this into equation (B.16) we get

$$\lim_{x'\to x}\psi_R^\dagger(x')(-i\partial_x\psi_R)(x)=\frac{1}{2\pi}\left[\frac{1}{(x'-x+i\alpha)^2}-i\frac{1}{2}\partial_x^2\phi_R(x)+\frac{1}{2}(\partial_x\phi_R(x))^2\right]. \qquad \text{(B.17)}$$

The first term is again the vacuum average, that has to be removed. The second term $\partial_x^2\phi_R$ is a total derivative that does not contribute to the Hamiltonian, and therefore can be neglected. In the computation for left movers an additional overall sign is found since

$$G_L(x-x')=\log\left(\frac{-ia}{(x-x')-ia}\right). \qquad \text{(B.18)}$$

Thus, the final result for the kinetic part of the Hamiltonian is

$$:\psi_\nu^\dagger(-i\partial_x)\psi_\nu:=\frac{\nu}{4\pi}(\partial_x\phi_\nu)^2. \qquad \text{(B.19)}$$

With this we have all the tools to bosonise the clean Tomonaga-Luttinger model Hamiltonian or the Hamiltonian of the quantum wire with spin-orbit coupling. The generalisation to these cases is straightforward.

We finish this appendix with deriving the correlation functions for the interacting spinful case, see equation (2.56). The computation for the general case with spin orbit coupling is equivalent, but lengthy. Computing the correlations permits us to see a main difference with respect to the Fermi liquid theory, the power law behaviour. We compute the Euclidean time-ordered single particle Green's function

$$G_{\sigma\nu}^T(x,\tau)\equiv\left\langle T\psi_{\nu\sigma}(x,\tau)\psi_{\nu\sigma}^\dagger(0,0)\right\rangle, \qquad \text{(B.20)}$$

where the time is Wick rotated, $it \to \tau$. With (B.2) the bosonic expression for this reads

$$G^T_{\sigma\nu}(x,\tau) = \frac{1}{2\pi a}\exp(\langle\phi_{\nu\sigma}(x,\tau)\phi_{\nu\sigma}(0,0)\rangle - \langle\phi_{\nu\sigma}(0,0)\phi_{\nu\sigma}(0,0)\rangle). \tag{B.21}$$

In all correlators of interest it is essential to know the bosonic correlators. The bosonic correlators are easily derived using Gaussian integration in a bosonic pathintegral formalism, see e.g. [46], obtaining

$$\begin{aligned}
\langle\phi_i(x,\tau)\phi_j(0,0)\rangle &= -\frac{K_j\delta_{ij}}{4\pi}\log\left(\frac{x^2+(v_j|\tau|+a)^2}{a^2}\right), && \text{(B.22)}\\
\langle\theta_i(x,\tau)\theta_j(0,0)\rangle &= -\frac{\delta_{ij}}{4\pi K_j}\log\left(\frac{x^2+(v_j|\tau|+a)^2}{a^2}\right), && \text{(B.23)}\\
\langle\phi_i(x,\tau)\theta_j(0,0)\rangle &= -\frac{\delta_{ij}}{4\pi}\log\left(\frac{v_j\tau - ix + \mathrm{sgn}\tau a}{v_j\tau + ix + \mathrm{sgn}\tau a}\right), && \text{(B.24)}
\end{aligned}$$

where $j = s, c$ and $K_c = K$ and $K_s = 1$. Thus, the single-particle Green's function is given as

$$G^T_{\sigma\nu}(x,\tau) = \frac{1}{2\pi a}\prod_{j=c,s}\left[\left(\frac{x^2+(v_j|\tau|+a)^2}{a^2}\right)^{-\gamma_j}\left(\frac{v_j\tau - ix + \mathrm{sgn}\tau a}{v_j\tau + ix + \mathrm{sgn}\tau a}\right)^{-\frac{\nu}{4}}\right], \tag{B.25}$$

where $\gamma_j = \frac{1}{8}\left(K_j + \frac{1}{K_j}\right)$. The non-zero temperature ($\beta = 1/k_bT$) expression for (B.25) is given following [46] as

$$\begin{aligned}
&G^T_{\sigma\nu}(x,\tau,\beta)\\
&= \frac{1}{2\pi a}\prod_{j=c,s}\left[\left|\frac{\beta^2 v_j^2}{\pi^2 a^2}\sin\left(\frac{\pi(v_j\tau+ix)}{\beta v_j}\right)\sin\left(\frac{\pi(v_j\tau-ix)}{\beta v_j}\right)\right|^{-\gamma_j}\left|\frac{\sin\left(\frac{\pi(v_j\tau-ix)}{\beta v_j}\right)}{\sin\left(\frac{\pi(v_j\tau+ix)}{\beta v_j}\right)}\right|^{-\frac{\nu}{4}}\right].
\end{aligned} \tag{B.26}$$

For the Hamiltonian (2.66) the correlation functions are computed analogously. The differences are that in equations (B.22) to (B.24) we do not find a Kronecker delta between the spin and the charge field correlators, reflecting the broken $SU(2)$ symmetry, leading to the exponents given from (2.98) to (2.102).

Bibliography

[1] H. Hahn, A. Sidorenko, and I. Tiginyanu. *Nanoscale Phenomena: Fundamentals and Applications*. Springer, Berlin, 2009.

[2] A. Korkin and F. Rosei. *Nanoelectronics and Photonics: From Atoms to Materials, Devices, and Architectures*. Springer, Berlin, 2008.

[3] B. Bhushan. *Springer Handbook of Nanotechnology*. Springer, Berlin, 2004.

[4] S. Datta. *Electronic Transport in Mesoscopic Systems*. University Press, Cambridge, 1995.

[5] G. Inzelt. *Conducting Polymers: A New Era in Electrochemistry*. Springer, Berlin, 2008.

[6] K.S. Novoselov, A.K. Geim, S.V. Morozov, D. Jiang, Y. Zhang, S.V. Dubonos, I.V. Grigorieva, and A.A. Firsov. Electric field effect in atomically thin carbon films. *Science*, 306:666, 2004.

[7] K.S. Novoselov, D. Jiang, F. Schedin, T.J. Booth, V.V. Khotkevich, S.V. Morosov, and A.K. Geim. Two-dimensional atomic crystals. *PNAS*, 102:10451, 2005.

[8] C. Thomson, S.Reich, and J. Maulzsch. *Carbon Nanotubes: Basic Concepts and Physical Properties*. WILEY-VCH, Weinheim, 2004.

[9] K.M. Kadish and R.S. Ruoff. *Fullerenes: Chemistry, Physics, and Technology*. Wiley, New York, 2000.

[10] I. Zutic, J. Fabian, and S. Das Sarma. Spintronics: Fundamentals and applications. *Rev. Mod. Phys*, 76:323, 2004.

[11] P. Grünberg, R. Schreiber, Y. Pang, M. B. Brodsky, and H. Sowers. Layered magnetic structures: Evidence for antiferromagnetic coupling of Fe layers across Cr interlayers. *Phys. Rev. Lett.*, 57(19):2442, 1986.

[12] S. Datta and B. Das. Electronic analog of the electro-optic modulator. *Appl. Phys. Lett.*, 56:665, 1990.

[13] Åkerman J. Toward a universal memory. *Science*, 308:508, 2005.

[14] A. Fert. Nobel lecture: Origin, development, and future of spintronics. *Rev. Mod. Phys.*, 80:1517, 2008.

[15] P. A. Grünberg. Nobel lecture: From spin waves to giant magnetoresistance and beyond. *Rev. Mod. Phys.*, 80:1531, 2008.

[16] J. S. Moodera, Lisa R. Kinder, Terrilyn M. Wong, and R. Meservey. Large magnetoresistance at room temperature in ferromagnetic thin film tunnel junctions. *Phys. Rev. Lett.*, 74(16):3273, 1995.

[17] H.C. Koo, J.H. Kwon, J. Eom, J. Chang, S.H. Han, and M. Johnson. Control of spin precession in a spin-injected field effect transistor. *Science*, 325:1515, 2010.

[18] A.N.M. Zainuddin, S. Hong, L. Siddiqui, and S. Datta. Voltage controlled spin precession. *arXiv:1001.1523v1*, 2010.

[19] P. Agnihotri and S.Bandyopadhyay. Analysis of the two dimensional Datta-Das spin field effect transistor. *arXiv:1001.2705v2*, 2010.

[20] M. Governale and U. Zülicke. Spin accumulation in quantum wires with strong Rashba spin-orbit coupling. *Phys. Rev. B*, 66:073311, 2002.

[21] A. Schulz, A. De Martino, P. Ingenhoven, and R. Egger. Low energy theory and RKKY interaction for interacting quantum wires with Rashba spin-orbit coupling. *Phys. Rev. B*, 79:205432, 2009.

[22] A.B. Kaiser. Electronic transport properties of conducting polymers and carbon nanotubes. *Reports on Progress in Physics*, 64:1, 2001.

[23] A.J. Heeger, S. Kivelson, J.R. Schrieffer, and W.-P. Su. Solitons in conducting polymers. *Rev. Mod. Phys.*, 60:781, 1988.

[24] P. Ingenhoven, R. Egger, and U. Zülicke. Spin transport and bipolaron density in organic polymers. *J. Phys.: Condens Matter*, 21:415302, 2009.

[25] R.E. Peierls. Quelques proprietes typiques des corps solides. *Ann. I.H. Pointcare*, 5:250, 1935.

[26] P. Ingenhoven, J. Z. Bernad, U. Zülicke, and R. Egger. Features due to spin-orbit coupling in the optical conductivity of single-layer graphene. *Phys. Rev. B*, 81:035421, 2010.

[27] Y.A. Bychkov and E.I. Rashba. Oscillatory effects and the magnetic susceptibility of carriers in inversion layers. *J. Phys. C*, 17:6039, 1984.

[28] R. Winkler. Rashba spin splitting in two-dimensional electron and hole systems. *Phys. Rev. B*, 62:4245.

[29] R. Winkler. *Spin-orbit coupling effects in two-dimensional electron and hole systems.* Springer, Berlin, 2003.

[30] J. Schliemann, J.C. Egues, and D. Loss. Nonballistic spin-field-effect transistor. *Phys. Rev. Lett.*, 90:146801, 2003.

[31] J. Nitta, T. Akazaki, H. Takayanagi, and T. Enoki. Gate control of spin-orbit interaction in an inverted $\mathrm{In_{0.53}Ga_{0.47}As/In_{0.52}Al_{0.48}As}$ heterostructure. *Phys. Rev. Lett.*, 78:1335, 1997.

[32] G. Engels, J. Lange, Th. Schäpers, and H. Lüth. Experimental and theoretical approach to spin splitting in modulation-doped $\mathrm{In}_x\mathrm{Ga}_{1-x}\mathrm{As/InP}$ quantum wells for $B\rightarrow 0$. *Phys. Rev. B*, 55:R1958.

[33] D. Grundler. Large Rashba splitting in InAs quantum wells due to electron wave function penetration into the barrier layers. *Phys. Rev. Lett.*, 84:6074, 2000.

[34] Y. Kato, R.C. Myers, A.C. Gossard, and D.D. Awschalom. Coherent spin manipulation without magnetic fields in strained semiconductors. *Nature*, 427:50, 2004.

[35] J. Schäfer, C. Blumenstein, S. Meyer, M. Wisniewski, and R. Claessen. New model system for a one-dimensional electron liquid: Self-organized atomic gold chains on Ge(001). *Phys. Rev. Lett.*, 101:236802, 2008.

[36] A.V. Moroz and C.H.W. Barnes. Effect of the spin-orbit interaction on the band structure and conductance of quasi-one-dimensional systems. *Phys. Rev. B*, 60:14272, 1999.

[37] A.V. Moroz and C.H.W. Barnes. Spin-orbit interaction as a source of spectral and transport properties in quasi-one-dimensional systems. *Phys. Rev. B*, 61:R2464, 2000.

[38] E. A. de Andrada e Silva and G. C. La Rocca. Rashba spin splitting in semiconductor quantum wires. *Phys. Rev. B*, 67:165318, 2003.

[39] S.L. Erlingsson, J.C. Egues, and D. Loss. Spin densities in parabolic quantum wires with Rashba spin-orbit interaction. *Phys. Stat. Sol. (c)*, 3:4317, 2006.

[40] C.A. Perroni, D. Bercioux, V. Marigliano Ramaglia, and V. Cataudella. Rashba quantum wire: exact solution and ballistic transport. *J. Phys.: Cond. Matt.*, 19:186227, 2007.

[41] A. De Martino, R. Egger, and A.M. Tsvelik. Nonlinear magnetotransport in interacting chiral nanotubes. *Phys. Rev. Lett.*, 97:076402, 2006.

[42] W. Häusler. Rashba precession in quantum wires with interaction. *Phys. Rev. B*, 63:121310(R), 2001.

[43] K. Kuroki T. Kimura and H. Aoki. Generation of spin-polarized currents in Zeeman-split Tomonaga-Luttinger models. *Phys. Rev. B*, 53:9572, 1996.

[44] M. Governale and U. Zülicke. Rashba spin splitting in quantum wires. *Solid State Comm*, 131:581, 2004.

[45] T. Kaneko, M. Koshino, and T. Ando. Numerical study of spin relaxation in a quantum wire with spin-orbit interaction. *Phys. Rev. B*, 78:245303, 2008.

[46] T. Giamarchi. *Quantum Physics in One Dimension.* University Press, Oxford, 2004.

[47] A.O. Gogolin, A.A. Nersesyan, and A.M. Tsvelik. *Bosonization and Strongly Correlated Systems.* University Press, Cambridge, 1998.

[48] A.V. Moroz, K.V. Samokhin, and C.H.W. Barnes. Spin-orbit coupling in interacting quasi-one-dimensional electron systems. *Phys. Rev. Lett.*, 84:4164, 2000.

[49] A.V. Moroz, K.V. Samokhin, and C.H.W. Barnes. Theory of quasi-one-dimensional electron liquids with spin-orbit coupling. *Phys. Rev. B*, 62:16900, 2000.

[50] A. De Martino and R. Egger. ESR theory for interacting 1D quantum wires. *Europhys. Lett.*, 56:570, 2001.

[51] A. Iucci. Correlation functions for one-dimensional interacting fermions with spin-orbit coupling. *Phys. Rev. B*, 68:075107, 2003.

[52] W. Häusler. Dephasing in Rashba spin precession along multichannel quantum wires and nanotubes. *Phys. Rev. B*, 70:115313, 2004.

[53] V. Gritsev, G.I. Japaridze, M. Pletyukhov, and D. Baeriswyl. Competing effects of interactions and spin-orbit coupling in a quantum wire. *Phys. Rev. Lett.*, 94:137207, 2005.

[54] M.A. Ruderman and C. Kittel. Indirect exchange coupling of nuclear magnetic moments by conduction electrons. *Phys. Rev.*, 96:99, 1954.

[55] T. Kasuya. A theory of metallic ferro- and antiferromagnetism on Zener's model. *Prog. Theor. Phys.*, 16:45, 1956.

[56] K. Yosida. Magnetic properties of Cu-Mn alloys. *Phys. Rev.*, 106:893, 1957.

[57] C. Kittel. Indirect exchange interactions in metals. *Sol. State Phys.*, 22:1, 1968.

[58] Y. Yafet. Ruderman-Kittel-Kasuya-Yosida range function of a one-dimensional free-electron gas. *Phys. Rev. B*, 36:3948, 1987.

[59] H. Imamura, P. Bruno, and Y. Utsumi. Twisted exchange interaction between localized spins embedded in a one- or two-dimensional electron gas with Rashba spin-orbit coupling. *Phys. Rev. B*, 69:121303(R), 2004.

[60] P. Lyu, N.-N. Liu, and C. Zhang. Gate-tunable Ruderman-Kittel-Kasuya-Yosida interaction mediated by low-dimensional electrons with Rashba spin-orbit coupling. *J. Appl. Phys.*, 102:103910, 2007.

[61] J. Simonin. Kondo quantum dots and the novel Kondo-doublet interaction. *Phys. Rev. Lett.*, 97:266804, 2006.

[62] R. Egger and H. Schoeller. RKKY interaction and Kondo screening cloud for strongly correlated electrons. *Phys. Rev. B*, 54:16337, 1996.

[63] K. Hallberg and R. Egger. Two-impurity Kondo problem for correlated electrons. *Phys. Rev. B*, 55:R8646, 1997.

[64] O.A. Starykh, D.L. Maslov, W. Häusler, and L.I. Glazman. *Interactions and quantum transport properties of lower dimensional systems*. Lecture Notes in Physics, (Proceedings of the International WEH Workshop). Springer, Hamburg, 1999.

[65] K.A. Muttalib and V.J. Emery. Solvable two-band model of fermions. *Phys. Rev. Lett.*, 57:1370, 1986.

[66] Johannes Voit. Charge-spin separation and the spectral properties of Luttinger liquids. *Phys. Rev. B*, 47(11):6740, 1993.

[67] I.H. Campbell and D.L. Smith. Physics of organic electronic devices. *Solid State Physics*, 55:1, 2001.

[68] A.B. Kaiser. Systematic conductivity behavior in conducting polymers: Effects of heterogeneous disorder. *Advanced Materials*, 13:927, 2001.

[69] W.J.M. Naber, S. Faez, and W.G. van der Wiel. Organic spintronics. *J. Phys. D: Appl. Phys.*, 40:R205, 2007.

[70] V. Dediu, M. Murgia, F.C. Matacotta, C. Taliani, and S. Barbanera. Room temperature spin polarized injection in organic semiconductor. *Sol. Stat. Comm.*, 122:181, 2002.

[71] Z.H. Xiong, D. Wu, Z.V. Vardeny, and J. Shi. Giant magnetoresistance in organic spin-valves. *Nature*, 427:821, 2004.

[72] S. Majumdar, H.S. Majumdar, R. Laiho, and R. Österbacka. Comparing small molecules and polymer for future organic spin-valves. *J. Alloys Comp.*, 423:169, 2006.

[73] S. Majumdar, H.S. Majumdar, R. Laiho, and R. Österbacka. Organic spin valves: effect of magnetic impurities on the spin transport properties of polymer spacers. *New J. Phys.*, 11:013022, 2009.

[74] A.H. Davis and K. Bussmann. Organic luminescent devices and magnetoelectronics. *J. Appl. Phys.*, 93:7358, 2003.

[75] I.H. Campbell and B.K. Crone. Energy barriers from ferromagnetic contacts to semiconducting polymers. *Appl. Phys. Lett.*, 90:242107, 2007.

[76] N. Kirova and S. Brazovskii. Contact kinetics in conducting polymers. *Synth. Metals*, 76:229, 1996.

[77] M.N. Bussac, D. Michaud, and L. Zuppiroli. Electrode injection into conjugated polymers. *Phys. Rev. Lett.*, 81:1678, 1998.

[78] D.M. Basko and E.M. Conwell. Theory of carrier injection into a polymer chain: Polaronic effects. *Phys. Rev. B*, 66:094304, 2002.

[79] S.J. Xie, K.H. Ahn, D.L. Smith, A.R. Bishop, and A. Saxena. Ground-state properties of ferromagnetic metal/conjugated polymer interfaces. *Phys. Rev. B*, 67:125202, 2003.

[80] A. Brataas, Yu.V. Nazarov, and G.E.W. Bauer. Finite-element theory of transport in ferromagnet normal metal systems. *Phys. Rev. Lett.*, 84:2481, 2000.

[81] D. Huertas Hernando, Yu.V. Nazarov, A. Brataas, and G.E.W. Bauer. Conductance modulation by spin precession in noncollinear ferromagnet normal-metal ferromagnet systems. *Phys. Rev. B*, 62:5700, 2000.

[82] L. Balents and R. Egger. Spin transport in interacting quantum wires and carbon nanotubes. *Phys. Rev. Lett.*, 85:3464, 2000.

[83] L. Balents and R. Egger. Spin-dependent transport in a Luttinger liquid. *Phys. Rev. B*, 64:035310, 2001.

[84] G. Magela e Silva. Electric-field effects on the competition between polarons and bipolarons in conjugated polymers. *Phys. Rev. B*, 61:10777, 2000.

[85] A. Johansson and S. Stafström. Polaron dynamics in a system of coupled conjugated polymer chains. *Phys. Rev. Lett.*, 86:3602, 2001.

[86] A. Johansson and S. Stafström. Soliton and polaron transport in trans-polyacetylene. *Phys. Rev. B*, 65:045207, 2002.

[87] H. Ma and U. Schollwöck. Dynamical simulations of charged soliton transport in conjugated polymers with the inclusion of electron-electron interactions. *J. Chem. Phys.*, 129:244705, 2008.

[88] J.A. Freire and G. Voss. Master equation approach to charge injection and transport in organic insulators. *J. Chem. Phys.*, 122:124705, 2005.

[89] P.P. Ruden and D.L. Smith. Theory of spin injection into conjugated organic semiconductors. *J. Appl. Phys.*, 95, 2004.

[90] J.F. Ren, J.Y. Fu, D.S. Liu, L.M. Mei, and S.J. Xie. Diffusion theory of spin injection into organic polymers. *J. Phys.: Cond. Matt.*, 17:2341, 2005.

[91] Z.G. Yu, M.A. Berding, and S.Krishnamurty. Spin drift, spin precession, and magnetoresistance of noncollinear magnet-polymer-magnetstructures. *Phys. Rev. B*, 71:060408(R), 2005.

[92] Y. Zhang, J. Ren, G. Hu, and S. Xie. Effects of polarons and bipolarons on spin polarized transport in an organic device. *Organic Electronics*, 9:687, 2008.

[93] H Takayama, Y.R. Lin-Liu, and K. Maki. Continuum model for solitons in polyacetylene. *Phys. Rev. B*, 21:2388, 1980.

[94] W.P. Su, J.R. Schrieffer, and A.J. Heeger. Solitons in polyacetylene. *Phys. Rev. Lett.*, 42:1698, 1979.

[95] W.P. Su, J.R. Schrieffer, and A.J. Heeger. Solitons excitations in polyacetylene. *Phys. Rev. B*, 22:2099, 1980.

[96] H. Bruus and K. Flensberg. *Many-body quantum theory in condensed matter physics, an introduction.* Oxford University Press, Oxford, 2004.

[97] S.A. Brazovskii and N.N Kirova. Electron selflocalization and periodic superstructures in quasi-one-dimensional dielectrics. *Sov. Sci. Rev. A Phys.*, 5:99, 1984.

[98] L.D. Landau and E.M. Lifshitz. *Quantum Mechanics.* Pergamon Press, New York, 1958.

[99] D. K. Campbell, A. R. Bishop, and K. Fesser. Polarons in quasi-one-dimensional systems. *Phys. Rev. B*, 26:6862, 1982.

[100] K.E. Ziemelis, A.T. Hussain, D.D.C. Bradley, R.H. Friend, J. Rühe, and G. Wegner. Optical spectroscopy of field-induced charge in poly(3-hexyl thienylene) metal-insulator-semiconductor structures: Evidence for polarons. *Phys. Rev. Lett.*, 66:2231, 1991.

[101] C. Botta, C. Mercogliano, A. Bolognesi, H.S. Majumbar, and A.J. Pal. Photoluminescence measurements to study conductance switching and data storage in polythiophene based devices. *Appl. Phys. Lett*, 85:2393, 2004.

[102] Y.Y. Deng and H. Sirringhaus. Optical absorptions of polyfluorene transistors. *Phys. Rev. B*, 72:045207, 2005.

[103] M.G. Harrison, D. Fichou, F. Garnier, and A. Yassar. In situ charge-modulation spectroscopy of oligothiophene field-effect diodes: from sexithiophene towards polythiophene. *Opt. Mater.*, 9:53, 1998.

[104] P.A. Bobbert, T.D. Nguyen, F.W.A. van Oost, B. Koopmans, and M. Wohlgenannt. Bipolaron mechanism for organic magnetoresistance. *Phys. Rev. Lett.*, 99:216801, 2007.

[105] J. Ren, Y. Zhang, and S. Xie. Charge current polarization and magnetoresistance in ferromagnetic/organic semiconductor/ferromagnetic devices. *Organic Electronics*, 9:1017, 2008.

[106] P.R. Wallace. The band theory of graphite. *Phys. Rev.*, 71:622, 1947.

[107] J. C. Slonczewski and P. R. Weiss. Band structure of graphite. *Phys. Rev.*, 109:272, 1958.

[108] A. H. Castro Neto, F. Guinea, N.M.R. Peres, K.S. Novoselov, and A.K. Geim. The electronic properties of graphene. *Rev. Mod. Phys.*, 81:109, 2009.

[109] Y. Zhang, Y. Tan, H.L. Stormer, and P. Kim. Experimental observation of the quantum hall effect and Berry's phase in graphene. *Nature (London)*, 438:201, 2005.

[110] K.S. Novoselov, A.K. Geim, S.V. Morozov, D. Jiang, Y. Zhang, S.V. Dubonos, I.V. Grigorieva, and A.A. Firsov. Two-dimensional gas of massless Dirac fermions in graphene. *Nature (London)*, 438:197, 2005.

[111] G. Dresselhaus and M.S. Dresselhaus. Spin-orbit interaction in graphite. *Phys. Rev.*, 140:A401, 1965.

[112] T. Ando. Spin-orbit interaction in carbon nanotubes. *J. Phys. Soc. Jpn.*, 69:1757, 2000.

[113] A. De Martino, R. Egger, K. Hallberg, and C.A. Balseiro. Spin-orbit coupling and electron spin resonance theory for carbon nanotubes. *Phys. Rev. Lett*, 88:206402, 2002.

[114] C.L. Kane and E.J. Mele. Quantum spin Hall effect in graphene. *Phys. Rev. Lett*, 95:226801, 2005.

[115] D. Huertas-Hernando, F. Guinea, and A. Brataas. Spin-orbit coupling in curved graphene, fullerenes, nanotubes, and nanotube caps. *Phys. Rev. B*, 74:155426, 2006.

[116] H. Min, J.E. Hill, N.A. Sinitsyn, B.R. Sahu, L. Kleinman, and A.H. MacDonald. Intrinsic and Rashba spin-orbit interactions in graphene sheets. *Phys. Rev. B.*, 74:165310, 2006.

[117] M. Zarea and N. Sandler. Rashba spin-orbit interaction in graphene and zigzag nanoribbons. *Phys. Rev. B*, 79:165442, 2009.

[118] D. Huertas-Hernando, F. Guinea, and A. Brataas. Spin-orbit-mediated spin relaxation in graphene. *Phys. Rev. Lett.*, 103:146801, 2009.

[119] A.H. Castro Neto and F. Guinea. Impurity-induced spin-orbit coupling in graphene. *Phys. Rev. Lett.*, 103:026804, 2009.

[120] E.I. Rashba. Graphene with structure-induced spin-orbit coupling: Spin-polarized states, spin zero modes, and quantum Hall effect. *Phys. Rev. B*, 79:161409(R), 2009.

[121] F. Kuemmeth and E.I. Rashba. Spin-polarized photoemission from graphene: Joint effect of sublattice interference and spin-orbit coupling to substrate. *arXiv:0906.1812*, 2009.

[122] F. Kuemmeth, S. Ilani, D.C. Ralph, and P.L McEuen. Coupling of spin and orbital motion of electrons in carbon nanotubes. *Nature (London)*, 452:448, 2008.

[123] A. Varykhalov, J. Sanchez-Barriga, A.M. Shikin, C. Biswas, E. Vescovo, A. Rybkin, D. Marchenko, and O. Rader. Electronic and magnetic properties of quasifreestanding graphene on Ni. *Phys. Rev. Lett.*, 101:157601, 2008.

[124] O. Rader, A. Varykhalov, J. Snachez-Barriga, D. Machenko, A. Rybkin, and A.M.Shikin. Is there a Rashba effect in graphene on 3D ferromagnets? *Phys. Rev. Lett.*, 102:057602, 2009.

[125] K. Ziegler. Robust transport properties in graphene. *Phys. Rev. Lett.*, 97:266802, 2006.

[126] K. Ziegler. Minimal conductivity of graphene: Nonuniversal values from the Kubo formula. *Phys. Rev. B*, 75:233407, 2007.

[127] L.A. Falkovsky and A.A. Varlamov. Space-time dispersion of graphene conductivity. *Eur. Phys J. B*, 56:281, 2007.

[128] N.M.R. Peres, T. Stauber, and A.H. Castro Neto. The infrared conductivity of graphene on top of silicon oxide. *Europhys. Lett.*, 84:38002, 2008.

[129] E.J. Nicol and J.P. Carbotte. Optical conductivity of bilayer graphene with and without an asymmetry gap. *Phys. Rev. B*, 77:155409, 2008.

[130] C. Zhang, L. Chen, and Z. Ma. Orientation dependence of the optical spectra in graphene at high frequencies. *Phys. Rev. B*, 77:241402(R), 2008.

[131] V.P. Gusynin, S.G. Sharapov, and J.P. Carbotte. Unusual microwave response of Dirac quasiparticles in graphene. *Phys. Rev. Lett.*, 96:256802, 2006.

[132] A. Yamakage, K.-I. Imura, J. Cayssol, and Y. Kuramoto. Spin-orbit effects in a graphene bipolar pn junction. *Europhys. Lett.*, 87:47005, 2009.

[133] A.R. Wright, G.X. Wang, W. Xu, Z. Zeng, and C. Zhang. The spin-orbit interaction enhanced terahertz absorption in graphene around the K point. *Microelec. J.*, 40:857, 2009.

[134] Y. Yao, F. Ye, X.L. Qi, S.C. Zhang, and Z. Fang. Spin-orbit gap of graphene: First-principles calculations. *Phys. Rev. B*, 75:041401(R), 2007.

[135] J.C. Boettger and S.B. Trickey. First-principles calculation of the spin-orbit splitting in graphene. *Phys. Rev. B*, 75:121402, 2007.

[136] M. Gmitra, S. Konschuh, C. Ertler, C. Ambrosch-Draxl, and J. Fabian. Band-structure topologies of graphene: spin-orbit coupling effects from first principles. *arXiv:0904.3315*, 2009.

[137] J. C. Slater and G. F. Koster. Simplified LCAO method for the periodic potential problem. *Phys. Rev.*, 94:1498, 1954.

[138] O. Madelung. *Introduction to Solid-State Theory.* Springer, Berlin, 1978.

[139] C.L. Kane and E.J. Mele. Z_2 topological order and the quantum spin Hall effect. *Phys. Rev. Lett.*, 95:146802, 2005.

[140] L. Brey and H.A. Fertig. Edge states and the quantized Hall effect in graphene. *Phys. Rev. B*, 73:195408, 2006.

[141] C. Wu, B.A. Bernevig, and S.-C. Zhang. Helical liquid and the edge of quantum spin Hall systems. *Phys. Rev. Lett.*, 96:106401, 2006.

[142] T. Giamarchi and H. Schulz. Anderson localization and interactions in one-dimensional metals. *Phys. Rev. B*, 37:325, 1988.

[143] T. Giamarchi and A.J. Millis. Conductivity of a Luttinger liquid. *Phys. Rev. B*, 46:9325, 1992.

[144] J.W. McClure. Band structure of graphite and de Haas-van Alphen effect. *Phys. Rev.*, 108:612, 1957.

[145] A.G. Grushin, B. Valenzuela, and M.A.H. Vozmediano. Effect of coulomb interactions on the optical properties of doped graphene. *Phys. Rev. B*, 80:155417, 2009.

[146] R van Gelderen and C Morais Smith. Rashba and intrinsic spin-orbit interaction in biased bilayer graphene. *arXiv:0911.0857v2*, 2009.

[147] Z. Fei, Y. Shi, L. Pu, F. Gao, Y. Liu, L. Sheng, B. Wang, R. Zhang, and Y. Zheng. High-energy optical conductivity of graphene determined by reflection contrast spectroscopy. *Phys. Rev. B*, 78:201402(R), 2008.

[148] K.F. Mak, M.Y. Sfeir, Y. Wu, C.H. Lui, J.A. Misewich, and T. F. Heinz. Measurement of the optical conductivity of graphene. *Phys. Rev. Lett.*, 101:196405, 2008.

[149] F. Schwabl. *Quantenmechanik für Fortgeschritene, QM 2.* Springer, Hamburg, 2004.

[150] R. Shankar. Bosonization: How to make it work for you on condensed matter. *Acta. Phys. Pol. B*, 26:1835, 1995.